MICHIGAN STATE UNIVERSITY
CYCLOTRON LABORATORY
EAST LANSING, MICHIGAN

ABSTRACT

AN INVESTIGATION OF (p,d) REACTIONS IN 1p SHELL NUCLEI

By Lorenz A. Kull

The energy levels of ^{5}Li, ^{6}Li, ^{8}Be, ^{9}B and ^{10}B excited in the (p,d) reaction have been studied with a 33.6 MeV incident proton beam from the Michigan State University sector focused, isochronous cyclotron. The differential cross sections were measured for the strongly excited levels using a solid state dE/dx counter telescope to detect the deuterons. The angular distributions were also measured for the elastic scattering of 33.6 MeV protons from ^{6}Li, ^{7}Li, ^{9}Be and ^{10}B. Optical model fits were made with a computer code to this elastic proton data and to deuteron elastic scattering data obtained from the literature in order to extract optical parameters. These optical model parameters were used in a computer code which performed distorted wave Born approximation (DWBA) calculations for the (p,d) reactions. The DWBA results were subsequently used to extract spectroscopic factors for all the strongly excited levels of the nuclei being studied.

Deuteron groups were detected corresponding to strongly excited levels of ^{5}Li at 0.0 and 16.6 meV excitation and to strongly excited levels of ^{6}Li at 0.0, 2.15,

3.57 and 5.38 MeV excitation. The energy spectra show deuteron groups corresponding to strongly excited levels of ^{8}Be at 0.0, 3.1, 11.4, 16.95, 17.62, 18.18 and 19.21 MeV excitation; a small deuteron yield was also observed corresponding to ^{8}Be excited levels at 16.6 and 19.15 MeV. Deuteron groups were observed corresponding to strongly excited levels of ^{9}B at 0.0, 2.35, 7.1 and 11.75 MeV excitation and to weakly excited ^{9}B levels at 2.8 and 14.6 MeV excitation. Deuteron groups were observed corresponding to strongly excited levels of ^{10}B at 0.0, 0.72, 1.76, 2.15, 3.57, 4.75, 5.18 and 6.04 MeV excitation; weakly excited levels were noted at 6.57 and 7.5 MeV excitation.

The experimental spectroscopic factors were compared with several different theoretical calculations for the reactions being studied. In particular, good agreement was found between the data and an intermediate coupling model of the 1p shell nuclei. On the basis of this general accord between experiment and theory, spin assignments were made for the observed ^{9}B levels from the intermediate coupling model predictions. Comparison of the experimental spectroscopic factors for the ^{10}B excited states with results from other experiments show that spectroscopic factors extracted by the present method do not depend significantly on the incident particle or its energy.

Angular distributions for all the strongly excited levels observed, with the exception of the ^{8}Be level at

11.4 MeV ($J^{\pi} = 4^{+}$), indicate the direct pickup of a 1p shell neutron. Isotopic spin mixing in the higher excited levels of ^{8}Be and the possibility of 2s-1d shell admixtures in the ground state wave functions of the target nuclei are discussed.

AN INVESTIGATION OF (p,d) REACTIONS IN 1p SHELL NUCLEI

By

Lorenz A. Kull

A THESIS

Submitted to
Michigan State University
in partial fulfillment of the requirements
for the degree of

DOCTOR OF PHILOSOPHY

Department of Physics

1967

ACKNOWLEDGMENTS

I would like to express my gratitude to Dr. Edwin Kashy for suggesting this work, for his continuing guidance during the experiments, and for helpful discussions of the results. I thank Dr. Morton M. Gordon for his intriguing introduction to the field of nuclear physics.

Thanks go to Mr. Raymond Kozub, Mr. Phillip Plauger, and Mr. Craig Barrows for their help in taking and analyzing the data.

I acknowledge the financial assistance of the National Science Foundation which provided partial support for the experimental program. I also acknowledge financial support from the National Aeronautics and Space Administration Traineeship which I held for three years.

I want to express my deepest appreciation to my wife, Joan, for helping with the typing and for her patience and understanding during my graduate work.

I also want to thank all the Michigan State University cyclotron staff members who have made this work possible with their untiring support of the nuclear experimental program.

TABLE OF CONTENTS

LIST OF TABLES

LIST OF FIGURES

INTRODUCTION

This thesis describes the results of (p,d) reactions using 34 MeV protons with targets of ^{6}Li, ^{7}Li, ^{9}Be, ^{10}B, and ^{11}B [1,2]. The first successful attempt to measure deuteron angular distributions for a variety of (p,d) reactions was made by K. G. Standing in 1956 using 18 MeV incident protons [3]. A clever and simple method was used to detect the deuterons. NaI crystals were cut to a thickness which just stopped deuterons of a selected energy. It can be shown that a deuteron at this critical energy produces a larger pulse at the scintillation counter output than any other deuteron or any proton. Thus, by carefully selecting the crystal thickness, a deuteron group corresponding to the ground state or a lower excited state of the residual nucleus could be displayed on a multichannel analyzer.

Previous studies of the (p,d) reactions with very light nuclei have been made at Princeton University with an incident proton energy of approximately 18 MeV in which only the lower excited states of the residual nuclei could be observed [4,5,6,7]. The same reactions were also studied at the University of Minnesota using 40 MeV protons [8,9], where a magnetic spectrometer was used to measure angular distributions out to 40° for most of the lower

excited states of the residual nuclei. Many other studies of these reactions have been done at even lower proton energies, most of which examined the properties of the ground state and lower excited states of ^{5}Li, ^{6}Li, ^{8}Be, ^{9}B, and ^{10}B [9]. The (p,d) reactions on these nuclei have also been investigated with incident proton energies of 95 MeV and above [11,12,13]. The range of observable excitation energy in the residual nuclei included all the known strongly excited levels; however, the energy resolution did not permit the separation of closely spaced levels.

The purpose of this work was to use an incident proton beam with sufficient energy to allow observation of all the strongly excited levels in ^{5}Li, ^{6}Li, ^{8}Be, ^{9}B, and ^{10}B, and yet with a low enough energy to enable the use of solid state radiation detectors with their desirable energy resolution capabilities. An incident proton energy of about 34 MeV fulfilled both requirements. The intensity and inherent energy resolution of the unanalyzed proton beam available from the Michigan State University cyclotron at this energy allowed angular distributions to be measured out to an angle between 100° and 140°, depending on the particular reaction being studied.

The data were analyzed to extract spectroscopic factors using a method successfully applied to (p,d) reactions with medium weight nuclei [14,15]. The experimental results were then compared to the theoretical intermediate coupling calculations in the 1p shell of Kurath [16], of Barker [17]

and of Balashov [18]. Special emphasis was placed on the comparison of the data to Kurath's work which is a complete model of the 1p shell for A = 5-16. The theoretical wave functions have been tested with regard to predictions of electromagnetic transition widths [19] and energy levels [20]; this work provides a separate and different test of this model's ability to predict experimentally verifiable quantities over a wide range of nuclei.

CHAPTER 1

NUCLEAR THEORY

1.A. The Distorted Wave Born Approximation

The direct interaction is defined as one in which the incident particle excites only one degree of freedom in the target nucleus. The specific types of direct interactions include knockout, inelastic scattering, stripping and pick-up. The (p,d) direct interaction is a pickup reaction in which the incident proton "plucks" a neutron from the target nucleus without exciting any other degrees of freedom of the target nucleus. The process can also be thought of as the incident proton dropping off a neutron "hole" which then interacts with the original target nucleus.

The direct interaction competes with the compound nucleus interaction in producing the measured yield of reaction products. The primary difference between these two different reaction processes is the time involved for the reaction to take place (Δt). The direct reaction has a Δt roughly associated with the time it takes for the incident particle to transit the nuclear volume ($\sim 10^{-22}$ sec); the compound nucleus reaction has a much longer Δt on the order of 10^{-14} sec [21]. For the case of incident protons, the compound process is dominant for very low incident energies (<5 MeV), the compound and direct processes are approximately

equivalent at higher incident energies (5-15 MeV), and the direct process is dominant for even higher incident energies (>15 MeV). The exact dependence of the relative compound and direct yields on incident projectile, incident energy, and target is not known, although work has been directed toward solving this problem for particular cases [22]. However, from this rough energy scale, this work at an incident proton energy of 34 MeV falls well inside the region in which the direct process is predominant.

The best clue for a direct interaction process, which the experimenter can look for, is an angular distribution strongly peaked in the forward direction and oscillating with increasing angle. The successful theoretical attempts to describe the direct process all predict this diffraction effect; the expression for the differential cross section for the reaction A(a,b)B proceeding by a direct interaction can be found in standard texts[23,24] and is given by equations (1) and (2):

$$(1) \qquad \frac{d\sigma}{d\Omega} = \frac{m_f m_i}{(2\pi\hbar^2)^2} \frac{K_f}{K_i} \sum_{AV} |T_{fi}|^2$$

$$(2) \qquad T_{fi} = \langle V_f \chi_f^{(-)} | V_f | \Psi^{(+)} \rangle$$

$m_i(m_f)$ = reduced mass in the incident (exit) channel.

$k_i(k_f)$ = wave number in the incident (exit) channel.

v_f = internal wave function of the final state nucleus.

$\chi_f^{(-)}$ = wave function for relative motion in the exit channel with an optical potential between b and B.

$\psi^{(+)}$ = Coulomb wave of relative motion between a and A plus outgoing Coulomb b waves from B.

V_f = final interaction not included in the central interaction of b with B.

$\sum_{AV}$ = sum over the unobserved quantum numbers in the exit channel and an average over those in the incident channel.

The equation (2) is an exact expression, however the exact form of $\psi^{(+)}$ is not known. In order to perform the calculation of (2), the function $\psi^{(+)}$ is replaced by $(\chi_i^{(+)} v_i)$ where:

$\chi_i^{(+)}$ = wave function for relative motion in the incident channel using an optical potential as an approximation to the real interaction between a and A.

v_i = internal wave function of initial state nucleus.

This approximation is known as the distorted wave Born approximation (DWBA).

The approach taken here will be to calculate $\frac{d\sigma}{d\Omega}$ from equations (1) and (2) for the direct process A(d,p)B and then use the principle of detailed balance to arrive at the

solution for $\frac{d\sigma}{d\Omega}$ for the inverse process, B(p,d)A. This appears to be a somewhat round about way to arrive at the answer. However, it was actually the procedure followed in obtaining the DWBA results, since the Masefield computer code, which was used to perform the calculation, originally was written to solve the (d,p) problem.

The effects of the potentials involved in the reaction A(d,p)B can all be located in the matrix element, T_{fi}. Effects internal to all the nuclei are included in the nuclear wave functions v_f and v_i. Central interactions between incoming and outgoing particles with A and B are included in the distorted waves $\chi_i^{(+)}$ and $\chi_f^{(-)}$. Everything left over is included in V_i (incident channel) and V_f (exit channel) where

(3a) $V_i = V_{pA} + V_{nA}$

(3b) $V_f = V_{pn} + V_{pA}$ (p-proton; n-neutron)

We assume V_{pA} to be zero in (3b) and hence neglect any non-central interaction of the outgoing proton with the core, (A). Therefore only the neutron-proton interaction is left to couple the initial state to the final state. We now rewrite (2) for the specific case A(d,p)B using the DWBA approximation.

$$(4)\quad T_{fi} = \left\langle V_B(\vec{r}_A, \vec{r}_n)\chi_f^{(-)}(\vec{R}_p, \vec{r}_p)\middle| V_{np}(\vec{r}_{np})\middle|\phi_d(\vec{r}_{np})\, V_A(\vec{r}_A)\, \chi_i^{(+)}(\vec{R}_d, \vec{r}_d)\right\rangle$$

The neutron is assumed to be captured into a shell model orbit characterized by the orbital and total angular momentum quantum numbers ℓ and j, respectively. Since the shell model wave functions constitute a complete set of orthonormal functions, we can expand v_B in this set without making any particular assumption about the nature of B.

$$(5)\quad V^{J_B}_{M_B}(\bar{r}_A,\bar{r}_n) = \sum_{\ell} S^{1/2}_{\ell J_A}\left[V^{J_A}_{M_A}(\bar{r}_A)\times \phi^{\ell}_{m}(\bar{r}_n)\right]^{J_B}_{M_B}$$

We omit consideration of the intrinsic spin of the neutron since it only complicates the calculation and doesn't add anything to the results. $S^{1/2}_{\ell j}$ is the spectroscopic amplitude. We can also write

$$(6)\quad \left[V^{J_A}_{M_A}(\bar{r}_A)\times \phi^{\ell}_{m}(\bar{r}_n)\right]^{J_B}_{M_B} = \sum_{m,M_A} C(J\ell M_A m | J_B M_B)\, V^{J_A}_{M_A}(\bar{r}_A)\,\phi^{\ell}_{m}(\bar{r}_n)$$

Now the assumption is made that the neutron goes into a definite orbit (ℓ,j) and the equation (5) can be written,

$$(7)\quad V^{J_B}_{M_B}(\bar{r}_A,\bar{r}_n) = S^{1/2}_{\ell J_A}\left[V^{J_A}_{M_A}(\bar{r}_A)\times \phi^{\ell}_{m}(\bar{r}_n)\right]^{J_B}_{M_B}$$

We insert (6) and (7) into (4) and using the orthogonality properties of the v^J_M arrive at,

$$(8)\quad T_{fi} = S^{1/2}_{\ell J_A} C(J_A \ell M_A m | J_B M_B) \int \phi^{\ell *}_{m}(\bar{r}_n)\,\chi^{(-)*}_{f}(\bar{K}_p,\bar{r}_p)\left\{V_{np}(\bar{r}_{np})\phi_d(\bar{r}_{np})\right\}\chi^{(+)}_{i}(\bar{K}_d,\bar{r}_d)\,d\bar{r}_n\,d\bar{r}_p$$

Consider the bracketed expression inside the integral in equation (8). We will use the zero range approximation for the deuteron wave function,

$$\phi_d(\bar{r}_{np}) = \sqrt{\frac{\gamma}{2\pi}}\,\frac{e^{-\gamma r_{np}}}{r_{np}} \qquad (9)$$

where $\frac{\hbar^2\gamma^2}{2m_{np}} = 2.23$ MeV (binding energy of deuteron). The meaning of this expression becomes clear if it is inserted in the Schroedinger equation for the bound neutron.

$$\left(-\frac{\hbar^2}{2m_{np}}\nabla^2 - V_{np}\right)\phi_d = E\phi_d$$

$$\frac{-\hbar^2}{2m_{np}}\left[\nabla^2 - \gamma^2\right]\phi_d = V_{np}\phi_d \qquad (10)$$

But, $\frac{e^{-\gamma r}}{r}$ is the Green's function for the operator $(\nabla^2 - \gamma^2)$, i.e.

$$\left(\nabla^2 - \gamma^2\right)\frac{e^{-\gamma r_{np}}}{r_{np}} = -4\pi\,\delta(r_n - r_p) \qquad (11)$$

Substituting equations (9) and (11) into (10),

$$\frac{-\hbar^2}{2m_{np}}\sqrt{8\pi\gamma}\;\delta(r_n - r_p) = V_{np}\,\phi_d(\bar{r}_{np}) \qquad (12)$$

With this choice of the deuteron wave function, we see that the neutron-proton interaction is represented in the calculation by a Dirac delta function, the mathematical counterpart of a zero range physical interaction. This is only a simple approximation of the actual physical situation where the interaction is of short, but finite range. The most desirable feature of the approximation is that it makes the calculation tractable. Some computer codes allow the insertion of a potential function (V_{np}) in place of the zero range approximation (ZRA) and the problem of ascertaining the effect of using the ZRA has been worked on [25,26,27]. Calculations made for medium and heavy weight nuclei show little change in shape in the angular distribution, with an overall increase in magnitude when the ZRA is used instead of the finite range interaction. The effect is not completely understood and is complicated by the fact that the actual interaction (V_{np}) is not known. The position adopted in this work will be to use the ZRA, keeping in mind its inherent limitations.

Inserting (12) into (8),

$$(13)\quad T_{fi} = \sum_{\ell J_A} \frac{\hbar^2}{2m_p} \sqrt{8\pi\gamma}\, C(J_A \ell M_A m | J_B M_B) \int \phi^{\ell *}_{m}(\bar{r})\, \chi_f^{(-)*}(\bar{K}_p, \bar{r})\, \chi_i^{(+)}(\bar{K}_d, \bar{r})\, d\bar{r}$$

The expression (13) is then inserted into (1) and a sum over the final magnetic substates yields a factor, $\frac{2J_B + 1}{2\ell + 1}$ (from the Clebsch-Gordon coefficients); averaging over the initial state produces a factor, $\frac{1}{2J_A + 1}$. Then

$$(14a)\quad \frac{d\sigma}{d\Omega}(A(d,p)B) = \frac{m_p m_d}{(2\pi\hbar^2)^2}\frac{K_p}{K_d}\frac{2J_B+1}{2J_A+1}\sum_m \frac{1}{2\ell+1} S_{\ell J_A} |\beta_{\ell m}|^2$$

where

$$(14b)\quad \beta_{\ell m} = \frac{\hbar^2}{2m_{np}}\sqrt{8\pi\gamma}\int \phi^{*\ell}_m(\bar{r})\,\chi^{(-)}_f(\bar{K}_p,\bar{r})\,\chi^{(+)}_i(\bar{K}_d,\bar{r})\,d\bar{r}$$

Let k_d lie along the polar axis (the deuteron beam points in the +z direction). Then the optical wave functions (χ) can be written (see equation 20).

$$\chi^{(+)}_i(\bar{K}_d,\bar{r}) = \frac{\sqrt{4\pi}}{K_d r}\sum_{\lambda'}\sqrt{2\lambda'+1}\; i^{\lambda'} f_{\lambda'}(K_d,r)\, Y^0_{\lambda'}(\bar{r})$$

$$(15)\quad \chi^{(-)*}_f(\bar{K}_p,\bar{r}) = \frac{\sqrt{4\pi}}{K_p r}\sum_{\lambda,u}\sqrt{2\lambda+1}\; i^{-\lambda} f_\lambda(K_p,r)\, Y^{u*}_\lambda(\bar{r})\sqrt{\frac{(\lambda-u)!}{(\lambda+u)!}}\, P^u_\lambda(\hat{K}_p\cdot\hat{K}_d)$$

Now set

$$\phi_m^{\ell}(\bar{r}) = u_\ell(r)\, Y_\ell^m(\bar{r}) \tag{16}$$

where $u_\ell(r)$ is determined by using a potential well whose depth and radius give the correct binding energy for the neutron (Q-2.223 MeV). After inserting (15) and (16) into the expression (14b) for $\beta_{\ell m}$, the integration can be performed over the angular coordinates with the aid of a Clebsch-Gordon series [28]. The result is

$$\beta_{\ell m} = \frac{\hbar^2}{2m_p}\frac{4\pi\sqrt{2\delta}}{K_p K_d}\sum_{\lambda,\lambda'}^{1}(2\lambda+1)\sqrt{\frac{(2\ell+1)(\lambda+m)!}{(\lambda-m)!}}\, i^{\lambda'-\lambda} C(\lambda\ell 00|\lambda' 0)\times C(\lambda\ell u m|\lambda' u')\, R_{\lambda\lambda'}\, P_\lambda^{-m}(\hat{K}_p\cdot\hat{K}_d) \tag{17}$$

where

$$R_{\lambda\lambda'} = \int_0^\infty f_\lambda(K_p r)\, f_{\lambda'}(K_d r)\, u_\ell(r)\, dr \tag{18}$$

The $f_\lambda(Kr)$ in the integral expression (18) are obtained by fitting the elastic scattering data* from p(B,B)p and d(A,A)d where the incident particle's energy is chosen so that p and d have center of mass energies as close as possible to those encountered in the pickup reaction

*This fitting was done using the computer code Abacus [29].

B(p,d)A. The Schroedinger equation for the elastic scattering is given by

$$(19)\quad \left(-\nabla^2+\frac{2m}{\hbar^2}U-K^2\right)\chi^{(\pm)}=0 \qquad ;\ \frac{\hbar K^2}{2m}=E$$

(Note: for ~~simplicity~~, we are ignoring the Coulomb term.) The solutions are of the form

$$(20a)\quad \chi^{(+)}=\frac{4\pi}{Kr}\sum_{\ell,m} i^{\ell} f_{\ell}(Kr)\, Y_{\ell}^{m}(\bar{r})\, Y_{\ell}^{m*}(\bar{K})$$

$$(20b)\quad \chi^{(-)}=\frac{4\pi}{Kr}\sum_{\ell,m} i^{\ell} f_{\ell}^{*}(Kr)\, Y_{\ell}^{m}(\bar{r})\, Y_{\ell}^{m*}(\bar{K})$$

The $^{(+)}$ and $^{(-)}$ signs refer to the outgoing and incoming boundary conditions, respectively.* The $f_{\lambda}(Kr)$ satisfy the differential equation

$$(21)\quad \left(-\frac{d^2}{dr^2}+\frac{\ell(\ell+1)}{r^2}+\frac{2m}{\hbar^2}U-K^2\right)f_{\ell}(Kr)=0$$

where

$$(22)\quad U=-Vf(r,R,a_R)-i4a_x W\frac{d}{dr}f(r,R,a_x)-\frac{1}{(m_\pi c)^2}\bar{\sigma}\cdot\bar{l}\,\frac{V_{so}}{r}\frac{d}{dr}f(r,R,a_R)$$

---

* $\chi^{(+)}\sim e^{i\bar{K}\cdot\bar{r}}$ + "outgoing wave"

$\chi^{(-)}\sim e^{i\bar{K}\cdot\bar{r}}$ + "incoming wave"

Here $f(r,R,a) = \frac{1}{e^{x}+1}$; $x = \frac{r - RA^{1/3}}{a}$

The actual potential used includes a term (U_c), the Coulomb potential of a uniformly charged sphere of radius $RA^{1/3}$ fermis. The potential also contains a "surface" absorption term and a simple spin orbit dependence. The parameters of this optical potential (U) are varied to obtain a calculated elastic angular distribution which matches the data. These parameters are then used in equation (3) to numerically evaluate the $f_i(Kr)$ for the integral expression (18).

Inserting equations (17) and (18) into (14a), we obtain a calculable expression for the differential cross section for the reaction A(d,p)B. This can now be related in a very simple manner to the differential cross section for the reaction B(p,d)A. The principle of detailed balance [30], which is a consequence of the principle of time reversal, gives the following relation:

$$(23)\quad \frac{d\sigma}{d\Omega}(B(p,d)A) = \frac{d\sigma}{d\Omega}(A(d,p)B)\,\frac{K_d^2}{K_p^2}\,\frac{(2J_d+1)(2J_A+1)}{(2J_p+1)(2J_B+1)}$$

Thus with (14a) this can be written

$$(24)\quad \frac{d\sigma}{d\Omega}(B(p,d)A) = \frac{m_p m_d}{(2\pi\hbar^2)^2}\,\frac{K_d}{K_p}\,\frac{3}{2}\sum_m \frac{1}{2l+1}\,S_{lJ}\,|\beta_{lm}|^2$$

It should be noted that the distorted deuteron waves, as calculated above, depend only on the position of the center of mass of the deuteron, whereas the weak coupling within the deuteron itself is likely to be sensitive to deformations caused by interactions with the target nucleus. This effect has not been taken into consideration in the calculation for the particle transfer reaction.

It should also be noted that the distorted waves calculated from an optical potential which reproduces the elastic scattering become a worse approximation to the actual outgoing deuteron waves as the residual nucleus is left in states of increasing excitation energy. In effect we are assuming that the outgoing waves from the residual nucleus' ground state are the same as those from one of its excited states; or equivalently, the different states of the same nucleus are assumed to resemble one another closely when considered as a scattering center. As the increase in excitation energy allows more distortion of the residual nucleus, the approximation gets worse. There is also a practical problem with unobtainable optical parameters for the scattering from unstable nuclei (e.g. ^{5}Li, ^{9}B, ^{8}Be). In these cases, the assumption must be made that the unstable nucleus differs very little from its nearest stable neighbor and then the optical parameters for the stable nucleus are used (e.g. ^{6}Li parameters for ^{5}Li).

Other limitations which could affect the validity of the final expression include the omission of the consideration

of isospin in the optical potential, non-local effects, and inelastic effects. These have all been treated elsewhere [31,32,33], but their effects on the calculations are not completely understood. The philosophy adopted in this study will be to attempt to obtain a reasonable fit to the data with the simplest possible form of the theory, as has been done in other similar (p,d) studies with different incident energies and other target nuclei [14,15].

I.B. The Intermediate Coupling Model

The (jj) coupling model has met with great success in explaining the features of heavy nuclei [34]. In this model, commonly referred to as the nuclear shell model, the spin orbit interaction attempts to orient each individual nucleon's spin ($\bar{s}_i$) relative to its orbital angular momentum ($\bar{\ell}_i$) to form a total angular momentum ($\bar{j}_i$). The individual $\bar{j}_i$ then interact to produce the jj coupling scheme, a characteristic set of energy levels for which various nuclear properties may be calculated.

However, the nucleon-nucleon force may also attempt to orient all of the individual nucleons' spins ($\bar{s}_i$) to form a total spin ($\bar{S}$) and their orbital angular momenta ($\bar{\ell}_i$) to form a total orbital angular momentum ($\bar{L}$). The $\bar{L}$ and $\bar{S}$ interact to produce the LS coupling scheme which is different in general from the jj scheme. LS coupling is commonly referred to as Russell-Saunders coupling in atomic spectroscopy; a field where this model has been very successfully applied.

As mentioned previously, the jj coupling model appears to agree with experiment very well in the case of heavy nuclei, but attempts to apply this model to the light 1p shell nuclei have not met with similar success. Moreover, the LS coupling scheme does not appear to fill all the gaps where the jj scheme fails. This is not a surprising result since the jj and LS coupling schemes only mark the two extremes of a more general theoretical model called intermediate coupling [35]. In this model, the spin-orbit forces compete with the nucleon-nucleon interactions, and produce a result which falls somewhere between the two extreme coupling schemes. If one were to plot the relative amount of jj to LS coupling as a function of the mass number A, the 1p nuclei would be found occupying the transition region between predominantly LS coupling (very light nuclei) and predominantly jj coupling (heavy nuclei)[36]. For this reason, the intermediate coupling calculations of Kurath have been chosen to be compared with the experimental results of this work [20]. The discussion of the intermediate coupling model which follows is not intended to be a comprehensive study, but only a brief survey of the problem to note some of its more important features.

Given a specific case of n nucleons all in the 1p shell, and using the basic physical laws of conservation of angular momentum, indistinguishability of identical particles, and the exclusion principle, it is possible to arrive at a set of allowed jj or LS wave functions which can be used to describe the ground state and excited states of the nucleus.

The energy level sequence and spacing in which these states fall depends on the interactions between the n lp shell nucleons. The phenomenological approach is taken in which an attempt is made to represent these interactions in a simple form which has empirical validity. We shall assume a 2-body central interaction $V(r_{ij})$ between nucleons multiplied by a dimensionless exchange operator, O_{ij}. In Rosenfeld's book [37], it is suggested that the most satisfactory version of O_{ij} is

(1a) $O_{ij} = \vec{\tau}_i \cdot \vec{\tau}_j \quad (0.1 + 0.23\, \vec{\sigma}_i \cdot \vec{\sigma}_j)$

Here, τ_i is the isotopic spin of the i^{th} particle and σ_i is its intrinsic spin. It can be shown [37] that the exchange operator (O_{ij}) can be approximated by an expression involving only the spin and space exchange operators (equation 1b).

(1b) $O_{ij} \simeq (0.93P - 0.13 - 0.26PQ + 0.46Q)$

P and Q are the space exchange (Majorana) and spin exchange (Bartlett) operators, respectively and PQ is the Heisenberg operator. A simplified version often used to make calculations more tractable and which approximates (1) closely in effect is

(2) $O_{ij} \simeq 0.8P + 0.2Q$

P can be looked upon as roughly representing the saturation effect in nuclear interactions and Q as an approximation to

the effect of a tensor interaction [35]. The spin-orbit interaction considered in this model is given by

(3) $$\sum_i a\, \bar{l}_i \cdot \bar{s}_i$$

where the parameter a is different for each nucleon shell.

The approach taken here will be to determine the energy level sequence and spacing for the allowed states of a nucleus as a function of the parameters a and V_{ij}, the result is then fitted to the experimentally observed level spacing and the magnitude of these parameters are fixed. After they are known, the Hamiltonian can be constructed and diagonalized and the wave functions for the levels determined. The wave functions can then be used to calculate all the nuclear properties of the levels.

We consider now the relatively simple case of ^{6}He with a 1s shell filled with 2 neutrons and 2 protons which will be considered as an inert core. The states of ^{6}He may then be characterized by a set of two nucleon LS wave functions which are made up from single particle wave functions with the following considerations. Given the space portions of the two single nucleon 1p shell wave functions, ψ and ϕ, the principle of indistinguishability (both 1p nucleons are neutrons) requires the space portion of the two nucleon wave function to be of the form

(4) $$\frac{1}{\sqrt{2}}(\psi_1 \phi_2 \pm \phi_1 \psi_2)$$

where $\psi_1 = \psi(\bar{r}_1)$ $\phi_1 = \phi(\bar{r}_1)$

$\psi_2 = \psi(\bar{r}_2)$ $\phi_2 = \phi(\bar{r}_2)$

The spin portion of the two nucleon wave function can similarly be written in terms of the single nucleon wave functions α and β*

$$
\begin{array}{l}
\alpha_1\alpha_2 \\
\beta_1\beta_2 \\
\frac{1}{2}(\alpha_1\beta_2 + \beta_1\alpha_2) \\
\frac{1}{2}(\alpha_1\beta_2 - \beta_1\alpha_2)
\end{array} \qquad (5)
$$

The neutrons are fermions, therefore the Pauli principle allows only four completely antisymmetric wave functions:

$$
\begin{aligned}
\Psi_1 &= \tfrac{1}{2}(\psi_1\phi_2 + \phi_1\psi_2)(\alpha_1\beta_2 - \beta_1\alpha_2) \\
\Psi_2 &= \tfrac{1}{\sqrt{2}}(\psi_1\phi_2 - \phi_1\psi_2)\alpha_1\alpha_2 \\
\Psi_3 &= \tfrac{1}{\sqrt{2}}(\psi_1\phi_2 - \phi_1\psi_2)\beta_1\beta_2 \\
\Psi_4 &= \tfrac{1}{2}(\psi_1\phi_2 - \phi_1\psi_2)(\alpha_1\beta_2 + \beta\alpha_2)
\end{aligned} \qquad (6)
$$

---

* α has quantum numbers S = 1/2, m_s = 1/2 (spin up) and β has quantum numbers S = 1/2, m_s = -1/2 (spin down).

Since only neutrons in the 1p shell are being considered, and if the initial Hamiltonian (H_o) contains the kinetic energy and a central potential representing the interaction of the 1p neutrons with the core, the Ψ_i are degenerate, i.e.

(7) $$H_o \Psi_i = E_o \Psi_i \quad ; i = 1\text{-}4$$

It can easily be seen that H_o and O_{ij} (equation 2) commute and therefore have the same set of eigenfunctions, however adding the nucleon-nucleon interaction between the 1p neutrons to the Hamiltonian will split the degeneracy as will be seen from the following arguments. Only the energy differences between the LS wave functions are of interest here so that in adding the interaction term O_{ij} to the Hamiltonian, integrals of the form

(8) $$E_i = \int \Psi_i^* V_{12} O_{12} \Psi_i$$

must be evaluated. Consider the case for E_2:

$$E_2 = \frac{1}{4} \int (\psi_1\phi_2 - \phi_1\psi_2)^*(\alpha_1\alpha_2)^* V_{12}(0.8P + 0.2Q)(\psi_1\phi_2 - \phi_1\psi_2)(\alpha_1\alpha_2)$$

(9) $$= .15 \left[\int \psi_1\phi_2 V_{12} \phi_1\psi_2 - \int \psi_1\phi_2 V_{12} \psi_1\phi_2 \right]$$

$$= .15 [K - L]$$

In atomic spectroscopy the integral K is commonly referred to as the exchange integral and the integral L as the ordinary integral. All the E_i can be expressed as a

linear combination of K and L so that the splitting of the degeneracy can be expressed in terms of the two parameters, K and L. The fact that the E_i (i=1-4) will, in general, be different is a reflection of the Pauli principle and the antisymmetric construction of the allowable wave functions.

The two parameters, K and L, are not completely independent, but depend on the range of the nucleon-nucleon interaction. This can be seen by considering two simple cases. If the range of the interaction is very long with respect to the spacial extent of the nucleus so that the potential is essentially constant out to the nuclear radius ($V_{12} = V$), then L = V and K = 0. On the other hand, if V_{12} is essentially of zero range, ($V_{12} = V\delta(r_1 - r_2)$), then L = K = V. The actual case of a finite range interaction must lie somewhere between these two extremes. Thus the energy level spacing can be expressed in terms of a single parameter K, where

(10) $$L = \gamma K$$

and γ is determined by estimating the range of the interaction in terms of the nuclear size. Since the splitting now depends only on the parameter K, it can be thought of as a measure of the strength of the LS coupling.*

---

*K is less than zero; the opposite sign is used in atomic spectroscopy where the interaction between electrons is repulsive instead of attractive as in the case here.

Returning to the case of ^{6}He, the LS wave functions which satisfy the conservation of angular momentum, the principle of indistinguishability, and Pauli's exclusion principle are ^1S_o, $^3P_{2,1,0}$, $^1D_2$.* Using the range relationship (equation 10) L=4K, the splitting of the degeneracy for the LS case has been worked out [38] and is given in Table 1.

TABLE 1. ^{6}He energy level spacing with the nucleon-nucleon potential in terms of the exchange integral parameter, K (LS coupling).

State	E	E(L=4K)	J
$^1D_2$	L-K	3K	2
$^3P_{2,1,0}$	-L+3K	-K	2,1,0
^1S_o	L+2K	6K	0

The spin-orbit coupling term can now be introduced as a perturbation which will split the degeneracy still present in the ^{3}P multiplet. It can be shown [35] that the spin-orbit interaction term (3) can be expressed as

$$\sum_i a \bar{l}_i \cdot \bar{s}_i = A \bar{L} \cdot \bar{S}$$

where $A = \frac{a}{2}$ for the 1p shell. The effect of this term on the energy level spacing is shown in Figure 1 by dashed lines.

*The notation here is $^{2s+1}L_J$.

The two neutrons in the 1p shell of ^{6}He can also be described by a set of jj wave functions which satisfy the same general conditions as those imposed on the LS set. The allowed wave functions are given in Table 2 along with the energy level spacing, assuming the only interaction to be the spin orbit term (equation 3).

TABLE 2.--^{6}He energy level spacing with the spin-orbit interaction in terms of the spin-orbit parameter a (jj coupling).

State	J	E
$(p^{3/2})^{2}$*	J=2,0	a
$(p^{3/2}p^{1/2})$	J=2,1	$-a/2$
$(p^{1/2})^{2}$	J=0	$-2a$

*The notation here is (ℓJ).

Note that the parameter a plays the same part in the jj scheme that K plays in the LS scheme. Thus a can be thought of as a measure of the strength of the jj coupling.

As would be expected, the same values of J are allowed in both the LS and jj schemes since these are simply different representations of the same states. This leads to the assumption that each individual state (J) goes over smoothly from LS coupling to jj coupling. An equation describing the splitting between the states for each set of allowed J's (2,1,0) is constructed as a function of K and a such that as K approaches zero, the roots are those calculated

for jj coupling, and as a approaches zero, the roots are those calculated for LS coupling with a spin orbit perturbation. Thus we have for J = 2,

$$E^2 - (2K + \frac{a}{2})\ E + \frac{3}{2}\ Ka - 3K^2 - \frac{a^2}{2} = 0,$$

and for J = 1,

$$E = \quad - K - \frac{a}{2},$$

and finally for J = 0,

$$E^2 - (5K-a)\ E - 6Ka - 6K^2 - 2a^2 = 0$$

The solution to these equations is plotted as a function of a/K in Figure 1 which graphically portrays the change in the energy level splitting as the coupling changes from LS to jj, i.e. as a/K goes from zero to a very large value. For this particular case, the relative position of the first 3 levels of ^{6}He determined experimentally could be used to fix the parameters a/K and K and the prediction for the upper two levels used to test the theory against experiment. Once the values of a/K and K are obtained, the energy matrix can be diagonalized and the actual wave functions for the states determined so that other nuclear properties of the theoretical levels can be calculated and compared with experiment (19).

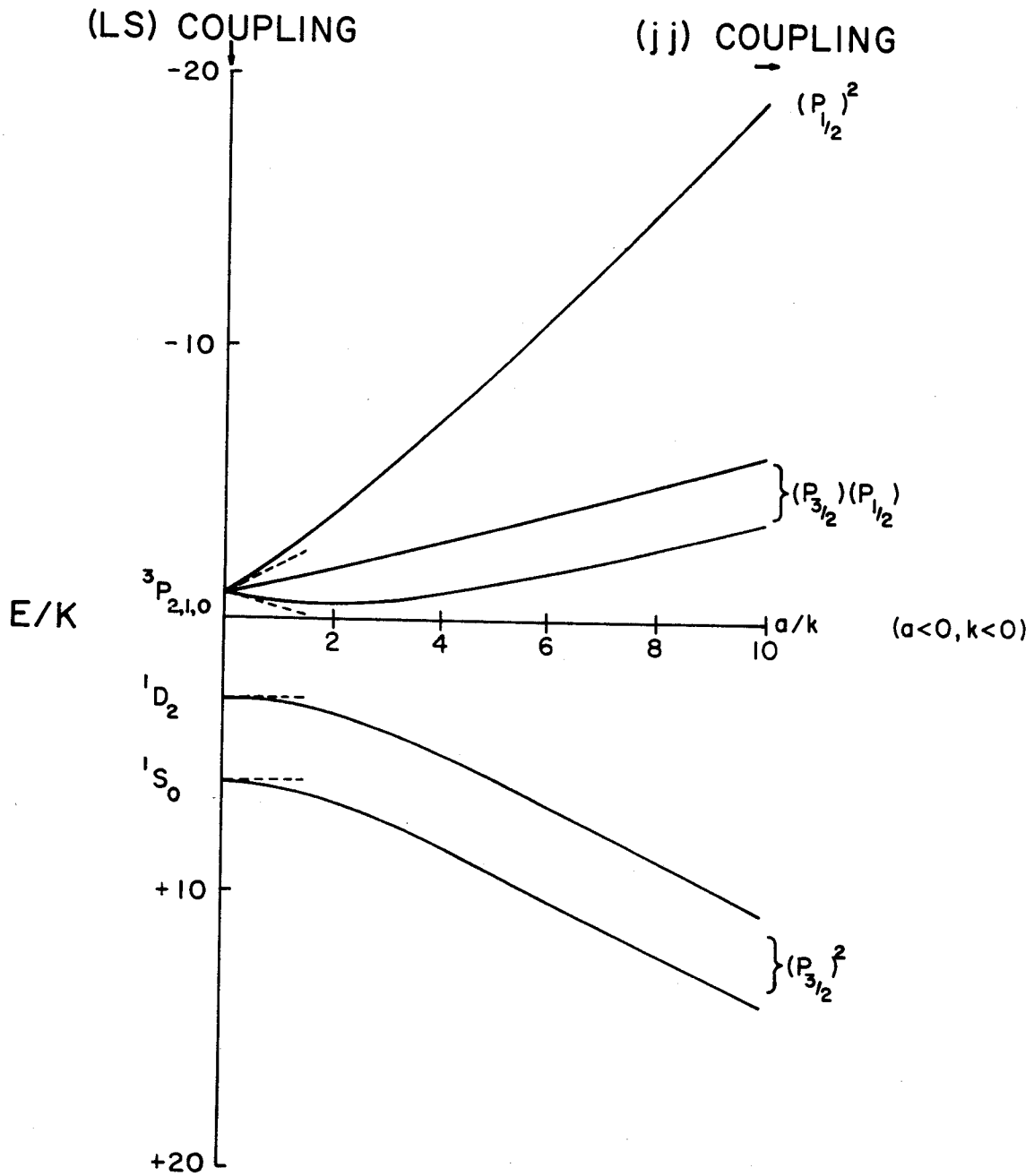

Figure 1.--^{6}He energy level spacing vs. intermediate couple parameter, a/K.

The above case of ^{6}He is extremely simple and of little practical use since only two levels of ^{6}He have been found experimentally. The same is true for the T = 1 levels of ^{6}Li for which the model also would apply. This case was chosen simply to illustrate the more important considerations in an intermediate coupling calculation. The method of calculation used at the present time is far more sophisticated, employing large computers and extensive search routines [39]. The inclusion of non-identical particles, such as in the case of ^{6}Li, introduces the concept of isotopic spin and requires the extension of the Pauli exclusion principle to preserve the total anti-symmetry of the nucleon wave functions. The additional symmetry considerations introduced by the inclusion of isotopic spin can be said to have the same kind of effect as the addition of intrinsic spin, in that the symmetries imposed on the wave function are reflected in the level spacing. The inclusion of more particles into the 1p shell also complicates matters, but the basic ideas included in this simple intermediate coupling model problem still prevail.

CHAPTER 2

EXPERIMENTAL APPARATUS

2.A. Cyclotron and Beam Handling Apparatus

Negative hydrogen ions (H^-) were accelerated by the Michigan State University sector-focused, isochronous cyclotron [40] to an energy of 33.6 MeV and a proton beam was extracted by means of a 700 $\mu g/cm^2$ aluminum stripping foil [41]. This method of obtaining an external proton beam employs a thin metal foil placed at the radius at which the beam is to be extracted from the machine. On passing through the metal foil, the negative hydrogen ions are stripped of their two electrons and emerge as positively charged ions (H^+). The Lorentz force on the H^+ ions is in the opposite direction from that on the H^- ions so that the stripped beam is deflected out of the cyclotron's magnetic field. The main difficulty encountered was that, under certain conditions, more than one turn of the internal beam may pass through the stripping foil and hence two or more proton groups (each of which is separated by $\sim$80 keV in energy) may be extracted. The presence of more than one turn in the extracted beam was detected by double peaking in the deuteron energy spectra, a condition which prohibited taking useful data. This situation was corrected primarily by adjusting the internal beam

orientation (or turn structure) although a small amount of beam from a second extracted turn could sometimes be prevented from entering the scattering chamber by adjusting the parameters of the external beam handling apparatus.

The extracted proton beam travels down an evacuated beam pipe through two quadrupole, vertical and horizontal focusing magnets and a 20° bending magnet (see Fig. 2). The strengths of the quadrupole fields are sufficient to focus the beam at the collimating slit located near the entrance to the 36 inch scattering chamber. Two small electromagnets, referred to as "Kink" magnets, are used to provide small vertical and horizontal deflection of the beam before it enters the collimator. Just in front of the collimating slit is a remotely controlled scintillating foil* which can be moved into the beam line and viewed with a closed circuit TV camera. The scintillator foil was used to initially locate and focus the beam at approximately the point where it enters the scattering chamber.

2.B. Faraday Cup and Current Integrator

Protons which pass through the target (at the geometric center of the scattering chamber) are collected in a Faraday cup, insulated from ground, at the rear of the chamber (see Fig. 2). Protons stopping in the insulated cup build up an integrated charge which can be measured to provide a

---

*Pilot "B" scintillator, .010 inches thick from Pilot Chemical, Watertown, Mass.

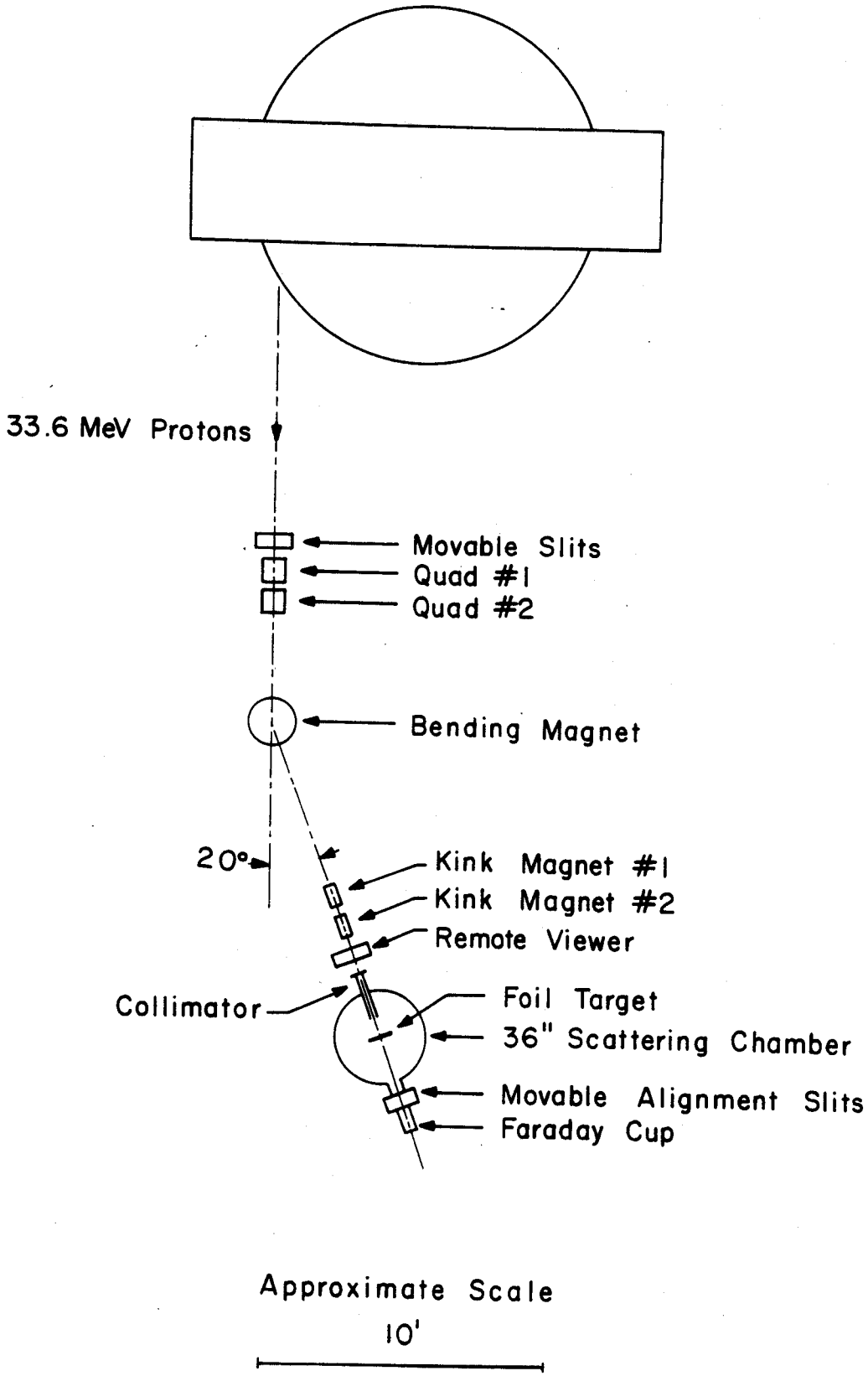

Figure 2.--External Beam Geometry.

figure for the number of protons incident on the target during a run. The entrance to the Faraday cup is ∿12 inches back from the outer wall of the chamber; the diameter of the cup is 2 7/8 inches and the depth is 11 1/2 inches. Any beam which can get through the collimating slit at the entrance to the chamber falls within a circle 1 5/8 inches in diameter at the entrance to the cup; thus, there is sufficient allowance for the collection of protons undergoing small angle Coulomb scattering in the target.

No significant difference was noted in the collected charge due to the loss of secondary electrons emitted inside this deep cup in experiments performed at the laboratory where permanent magnets were placed near the entrance of the cup to trap any escaping secondary electrons.

The beam current and integrated charge of the Faraday cup were measured using an Elcor model A310B current indicator and integrator. This instrument was checked to be accurate to within 1% using both external and internal calibration sources.

2.C. Target Holder

The target holder, positioned at the geometric center of the scattering chamber, can hold up to three 2" x 1 1/4" target frames and can be moved remotely in the vertical direction to expose any of the three targets to the beam (see Fig. 3). A standard target, such as a thin Mylar foil with a large deuteron yield and a well known energy spectrum

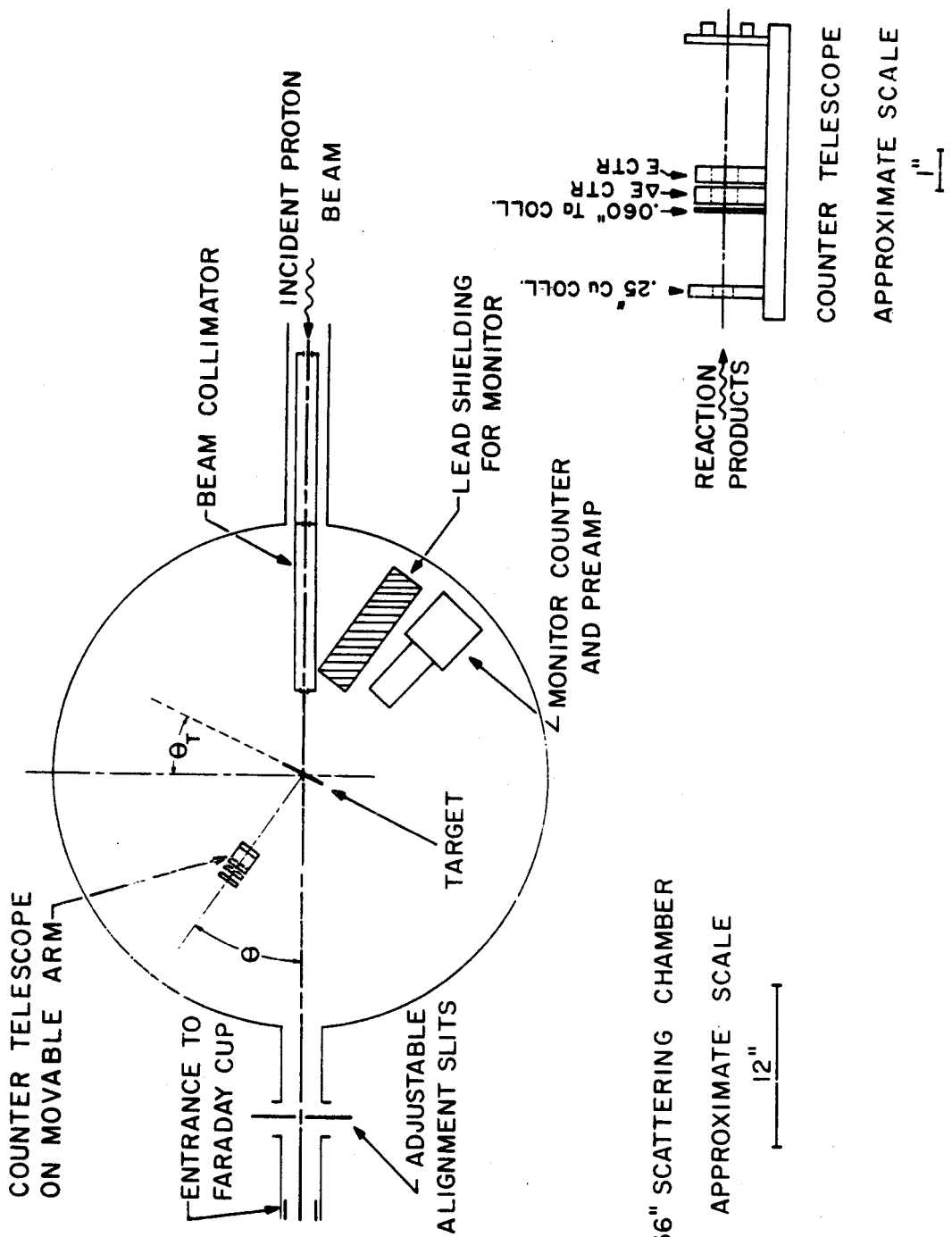

Figure 3.--Scattering chamber and counter telescope.

was used in tuning the system or for taking energy calibration spectra and afterwards the target of interest was positioned in the beam without disturbing the experimental set-up or shutting off the beam (see Fig. 6). The nominal target size used was ∿1 inch square which satisfies the requirement that all beam which passes through the collimator passes through the target area and is collected by the Faraday cup. The beam spot size on the target was about .12 inches wide and .25 inches high.

The target holder can be rotated through 360° and positioned to an accuracy of ±2°. This amounts to a small uncertainty in target thickness of ±1.2% at target angles of ∿20°, but for the largest target angle used of 45°, a significant uncertainty of 3.5% is introduced.

2.D. Beam Alignment Procedure

The front and rear slits of the beam collimator were aligned horizontally with the center of the target frame shaft (the geometric center of the scattering chamber) using an optical telescope. The collimator was leveled and the vertical height adjusted to that of the median plane of the cyclotron. In this way, a reference line was determined. The center of the 20° bending magnet also lay along this reference line. The movable counter arm was rotated until the center of the arm was aligned with the center line to determine the true $\theta = 0°$ position. Finally, the adjustable alignment slits between the rear of the scattering chamber

and the Faraday cup were aligned visually leaving an .12" gap at the center line (see Fig. 3). The proton beam was brought down the beam pipe and the cyclotron tuned until the desired energy resolution was obtained. The beam intensity was then balanced on the adjustable alignment slits with the downstream magnet array by measuring the current on the slits; afterwards the slits were moved out of the way in order to collect all the beam in the Faraday cup.

2.E. Detectors

Solid state detectors were used in a ΔE-E counter telescope configuration to identify and measure the energy of the incident deuterons. The ΔE counters were silicon surface barrier detectors with thicknesses between 150 and 770 microns; they were manufactured commercially by ORTEC*.

The basic design of these surface barrier detectors consists of a thin p-type layer on the surface of a high purity n-type wafer forming a p-n junction. Electrical contact is made to the p-surface through a gold film ∿150 Angstroms thick and to the n type surface through a non-rectifying contact. Applying a bias voltage (V_b) to the detector causes a depletion region ** to form of depth (D) where:

---

*ORTEC, Oak Ridge Technical Measurement Corporation.

**The depletion region is the region in which an electric field (E) is present and where exact compensation of the charge carriers exists.

(1) $E = E_{MAX}\ (D-X)$

(2) $E_{MAX} = 4.2 \times 10^4\ (V_{b/\rho n})$

(3) $D \approx 0.5\ \sqrt{\rho_n V_b}$

X = perpendicular distance (microns) in the n-type material measured from the p-type surface.

ρ_n = n-type resistivity in ohm-cm

(for n-type silicon)

E is in volts/cm, D in microns of silicon, and V_b in volts.

The operation of the surface barrier detector is analogous to that of an ionization chamber. Charged particles transiting the depletion region give up their energy by creating electron hole pairs ($\sim$3.5 ev/pair); the electric field present (E) separates the created charge carriers and sweeps them out of the depletion region. The motion of these carriers induces a charge Q in the external circuit which is proportional to the energy lost in the depletion region. An extensive treatment on the operation of these detectors, including performance characteristics and noise figures, can be found in reference [42].

The E counters were lithium drifted silicon detectors with a nominal thickness of $\sim$3 millimeters. All of the energy spectra presented in this work were taken with commercially produced devices, however preliminary work was done using lithium drifted counters which were fabricated by the author. The operation of these devices is similar to that of the surface barrier detectors. More details on their operation and construction can be found in Appendix I.

A 3 millimeter thick lithium drifted silicon detector will completely stop 30 meV deuterons, so that by selecting ΔE counters with depletion depths between 150 and 770 microns, 31 to 34 MeV deuterons can be completely stopped in the ΔE-E counter system. The minimum energy deuteron which can be detected is ∿6 MeV. This allows a minimum of 2 MeV of the incident deuteron's energy to be collected by the E counter for particle identification purposes.

2.F. Counter Telescope Assembly

The counters were mounted in standard holders fitted to a counter track. The track is accurately positioned on a movable arm inside the scattering chamber so that the center line of the counters goes through the geometric center of the chamber. The remotely movable arm could be rotated to ∿175° on either side of the incident beam direction and the position of the arm was read remotely to within an uncertainty of ±0.4°. On the counter track, directly in front of the ΔE counter is a tantalum collimator, .060 inches thick (see Fig. 3). This thickness will stop ∿44 MeV deuterons and ∿34 MeV protons. The diameter of the collimator opening is 0.152 inches which corresponds to an angle subtended by the counter in the scattering plane of $\leq$ 1° for the particular geometries which were used. There is a second copper collimator, 1/4 inch thick with a 1/2 inch diameter opening, placed 2 inches in front of the tantalum collimator (see Fig. 3). This arrangement insures that the sensitive area of the counters is only exposed to charged particles originating from the

target area and not to those scattered from the beam collimating slits.

The E counter is mounted in a copper holder which was cooled to dry ice temperatures (∿-78°C) by pumping cooled alcohol through a piece of copper tubing affixed to the top of the mount. The alcohol is pumped from a source located outside the scattering chamber through flexible plastic tubing.* Good charge collection was possible in the cooled counters and the deuteron energy resolution obtained was 100-130 KeV. In most cases, the cooling lowered a leakage current of the order of microamps at room temperature by a factor of ∿100.

2.G. Electronics

Signals from the E and ΔE counters are carried by coaxial cables** to TENNELEC model 100B charge sensitive, low noise, preamplifiers which are located directly outside the scattering chamber. The preamp outputs are routed to a particle identification system [43]. A brief description of the system and its use in this experiment follows:

A beam of 34 MeV protons on a target (A) will produce a large number of reactions, A(p,x)B, where x refers to

---

*Imperial-Eastman poly-flo tubing.

**Two types of cable are used:

(1) Sup. 6244 (capacitance/ft. = 9.3 pf, characteristic impedance = 125Ω).

(2) RG-62 (capacitance/ft. = 13.5 pf, characteristic impedance = 93Ω).

protons, elastic or inelastically scattered, deuterons, tritons, alpha-particles, etc. An energy pulse in the counters could originate from any of these reaction products, since there is no significant difference in the ionization produced by a proton, deuteron, triton, etc. with the same energy E. In this series of experiments, it was necessary to distinguish between deuteron energy pulses and energy pulses from other particles. This is the underlying reason for detecting a reaction product's total energy (E + ΔE) in two portions, i.e. by a ΔE counter and an E counter.

The first two components of the Goulding system consist of a set of matched amplifiers (see Fig. 4) which amplify and shape the E and ΔE pulses. A coincidence between the E and ΔE pulses is also required before either signal is allowed to proceed further. A timing pulse, which refers to the crossover of the doubly differentiated ΔE pulse, is sent to the mass generator, as well as a coincidence pulse which insures that both the E and ΔE pulses are present.

The E and ΔE pulses from the matched amplifiers are now sent to the particle identifier which:

(a) adds the E and ΔE pulses to produce a pulse (E + ΔE) proportional to the total energy of the detected particle.

(b) generates a pulse (P) whose amplitude is dependent upon the mass and charge of the detected particle.

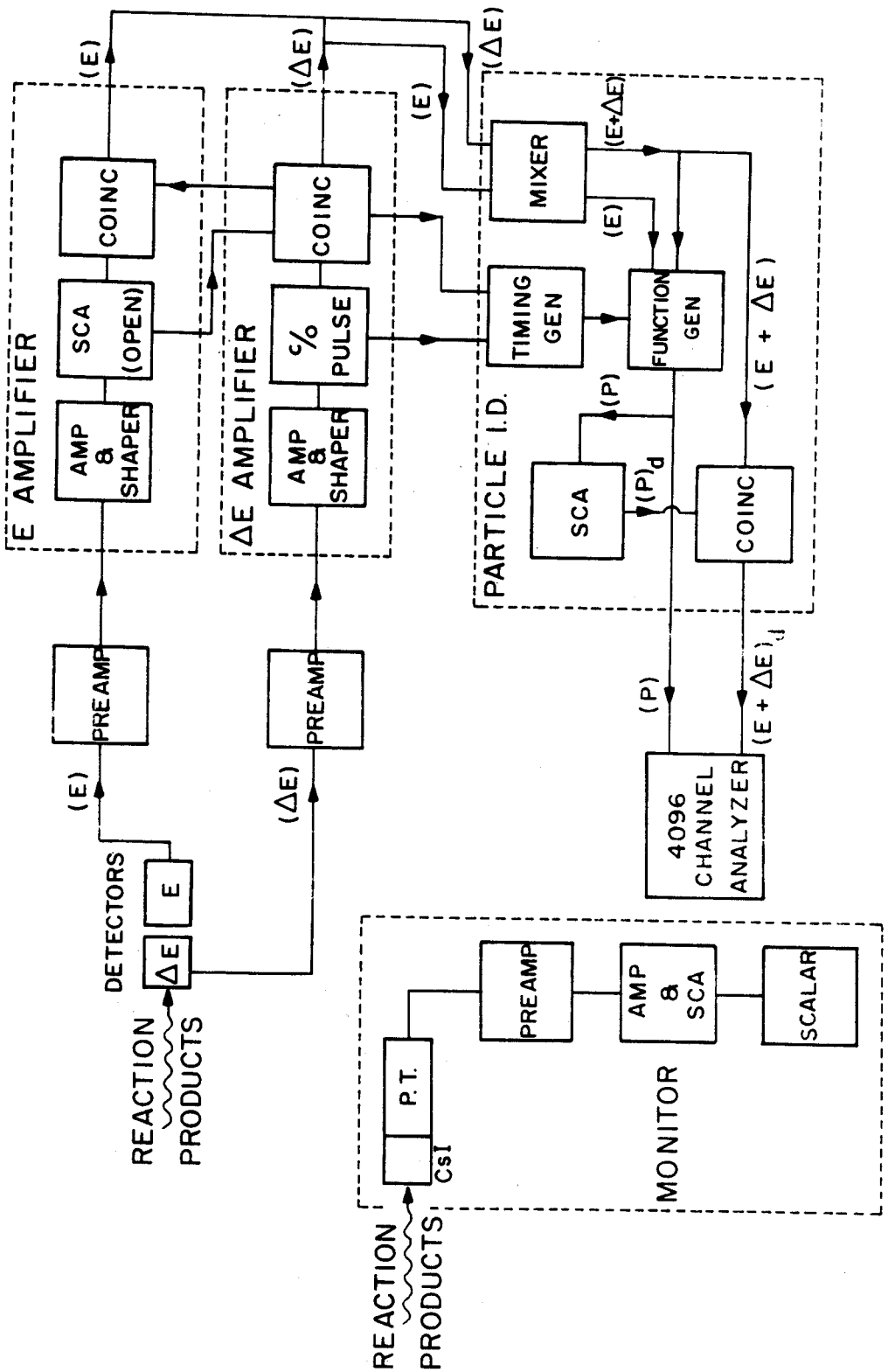

Figure 4.--Block diagram of electronics.

(c) contains the logic circuitry necessary to require a coincidence between the (E + ΔE) output and selected (P) pulses.

The operation of the second function of the mass generator (b) is based on the empirical range-energy relation (4) which is obeyed by particles in the energy range, 10 to 100 MeV.

(4) $R = a(M,Z)E^b$

R = particle range in absorber (silicon)

a = constant depending on the mass and charge of the particle

E = incident particle's energy

b = constant ($\sim$1.73)

Consider a particle (mass = M, charge = Z) about to enter the ΔE-E counter telescope with total energy (E + ΔE). The range of this particle (R_1) in the counter medium (silicon) is from (4),

(5) $R_1 = a(M,Z)\ (E + \Delta E)^b$

After penetrating the ΔE counter, the particle has energy (E) and its range in silicon is now given by (R_2), where

(6) $R_2 = a(M,Z)E^b$

However,

(7) $d = R_1 - R_2 = a(M,Z)\ [(E + \Delta E)^b - E^b]$

where d is the thickness of the ΔE counter. Equation (7) can be rewritten,

$$P = \frac{d}{a(M,Z)} = (E + \Delta E)^b - E^b$$

The quantity (P), which will be henceforth referred to as the "mass" pulse, is characteristic of the type of particle being detected and its value establishes the identity of the particle which produces the ΔE and E pulses. The heart of the particle identifier is therefore a function generator whose output is equal to the input (E + ΔE and E) raised to a power of ∿1.73.

The output pulses from the particle identifier ("mass", E + ΔE) are now displayed in a 2 dimensional mode on a 4096 channel analyzer.* The "mass" pulses are also routed through a single channel analyzer (SCA) whose output is necessary to satisfy a coincidence requirement set for the (E + ΔE) pulses before they leave the particle identifier. The window on the SCA is now closed until mass pulses corresponding only to deuterons provide the coincidence required for the (E + ΔE) signal and hence only those total energy pulses corresponding to detected deuterons are fed to the 4096 channel analyzer. The analyzer is then set in a one-dimensional mode with an input of (E + ΔE) pulses from detected deuterons; the spectra displayed in Chapter 4 were taken in this manner.

---

*Nuclear Data ND-160F 4096 channel analyzer.

Figure 5a is a one dimensional analyzer display of the "mass" pulse output from the particle identifier showing peaks corresponding to protons, deuterons, and tritons; Figure 5b is a similar spectrum with the window set to allow only deuteron pulses to get through. If Gaussian shapes are assumed for the deuteron and proton peaks in Figure 5a, less than 0.1% of the deuteron pulses are excluded by setting the gate and less than .001% of the proton pulses are included in the deuteron peak. (These spectra were taken with essentially no dead time on the analyzer.) The second (lower) spike on the proton peak results from protons which are not completely stopped in the E counter (dE/dx protons).

2.H. Data Processing

Deuteron spectra were taken in 1024 channels and the information was punched out on paper tape. The paper tape was then fed into an IBM tape-card converter and the card output processed by a computer program, PLOT*, which gives a linear or semi-log plot of the spectra and a channel listing. The peaks were then stripped from the background by hand and the actual cross sections determined by a computer program, SIGMA.** Kinematics calculations, necessary for the determination of optimum detector depths and target thicknesses, were obtained from a computer program, 8-BALL,** which does a relativistically correct kinematic calculation. Most of

---

*PLOT was written by P. Plauger.

**SIGMA and 8-BALL were written by L. Kull.

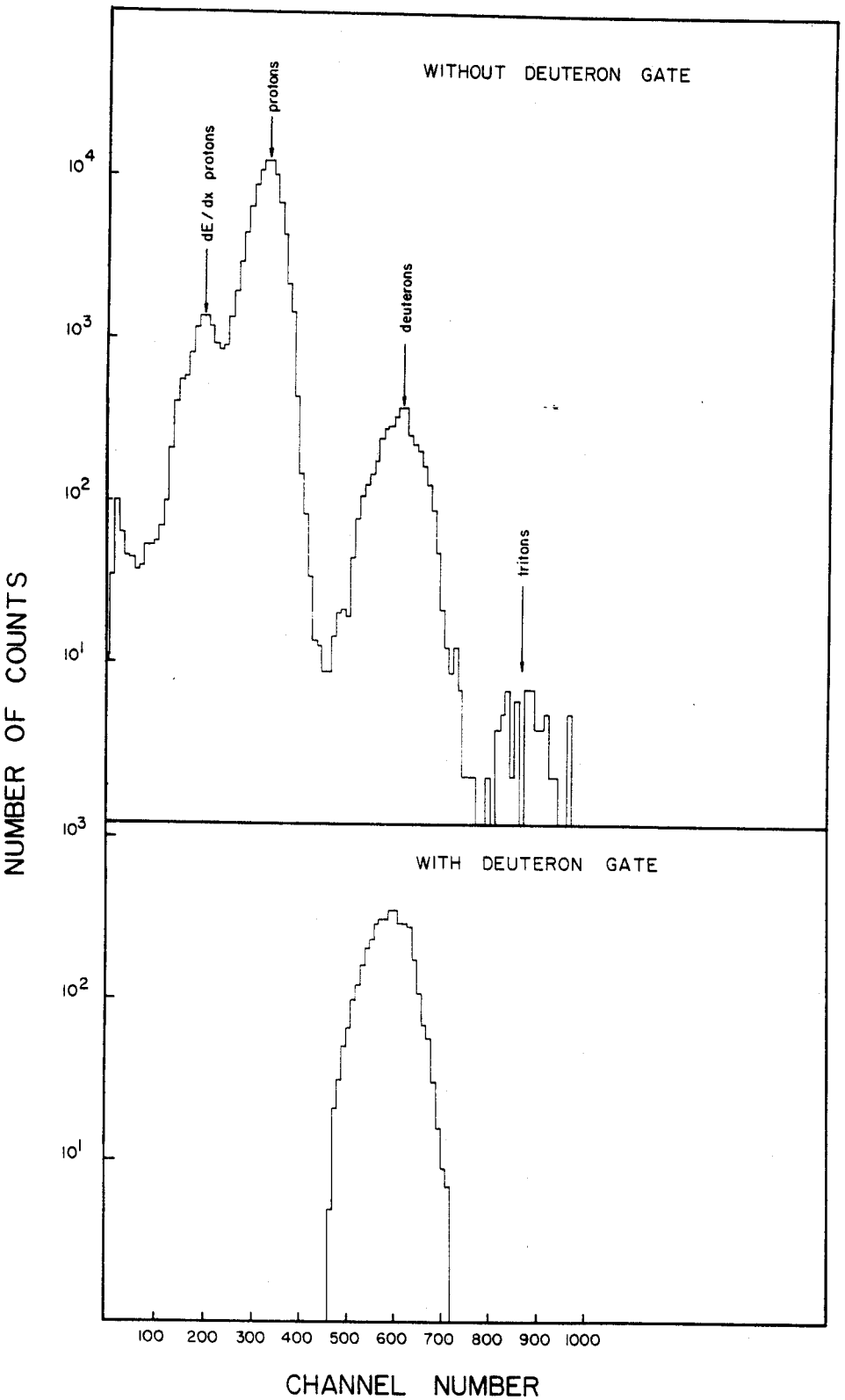

Figure 5.--Mass spectrum with and without deuteron gate.

the computer programs were run on the Michigan State University CDC 3600 computer, however plots of the last few spectra were obtained from a revised version of PLOT running on the MSU Cyclotron Laboratory's SDS SIGMA 7 computer.

2.I. Targets

The ^{6}Li targets were made by rolling isotopically enriched lithium (99.32% ^{6}Li) between two precision ground rolls to a thickness of $\sim$1.9 mg/cm^2. The lithium can be reduced in thickness without tearing if care is taken to keep the distance between the rollers set uniformly and the spacing of the rollers is reduced in steps of .001 to .003 inches. During the rolling process, the target and rolls are covered with a film of mineral oil to prevent the lithium from oxidizing during the rolling process. Before the target is inserted in the scattering chamber, it is placed in a kerosene bath in order to remove the mineral oil. The kerosene rapidly evaporates in the vacuum. The scattering chamber itself is filled with an inert argon atmosphere before inserting the target and again before the target is removed from the chamber for the purpose of weighing it. With these precautions, a typical observed oxygen contamination was $\sim$1.5%. The ^{7}Li targets were similarly fabricated from isotopically enriched lithium (99.993%^{7}Li) with thicknesses of $\sim$2.3 mg/cm^2.

The ^{9}Be target was a commercially rolled, 2.06 mg/cm^2 foil of natural beryllium (100% ^{9}Be). The ^{10}B targets were

purchased from the Nuclear Division of the Oak Ridge National Laboratory. They were made by depositing a layer of boron (92.15% ^{10}B) on a glass slide using an electron gun. The film of boron was fastened to a target frame and then floated off the glass slide in water. This resulted in a self supporting foil 158 $\mu g/cm^2$ in thickness (calculated by ORNL). The target thickness was remeasured using an alpha particle thickness gauge with 5.48 MeV particles obtained from an ^{241}Am source. Previously, the thickness gauge measurements proved to be within ±3% of the calculated value for standard mylar targets. The result for the ^{10}B target was 165 $\mu g/cm^2$; this is ∿4.2% from the ORNL value and hence in good agreement with it, since the ORNL figure is probably good to within ±5%.

The ^{11}B targets were made by using an electron gun to deposit isotopically enriched boron (98.05% ^{11}B) on a carbon backing ∿50 $\mu g/cm^2$ thick. The difference in Q value for the reactions $^{11}B(p,d)$ and $^{12}C(p,d)$ is ∿7.2 MeV so that the carbon contamination does not interfere with the strongly excited levels of ^{10}B.

Natural boron targets were also made by making a suspension of finely ground natural boron (80.22% ^{11}B and 19.78% ^{10}B) in a solution of polystyrene (C_6H_5 $CHCH_2$) dissolved in carbon tetrachloride (CCl_4). A few drops of the mixture are placed between two glass slides to spread the liquid out. When the CCl_4 evaporates, a thin foil (1-2 mg/cm^2) can be peeled off. The ratio of the ground state differential

cross sections for the $^{11}B(p,d)^{10}B$ and $^{10}B(p,d)^{9}B$ reactions was obtained with the natural boron targets at several angles; this ratio was used in conjunction with the differential cross section measured with the self-supporting ^{10}B target to obtain the absolute differential cross sections for the $^{11}B(p,d)$ reaction. From these figures, the thickness of the ^{11}B deposited on the carbon backing was determined to be 53 ± 4 $\mu g/cm^2$.

CHAPTER 3

ESTIMATES OF UNCERTAINTIES

3.A. Beam Energy

The energy of the incident proton beam was determined by the kinematic crossover method [44] and by an independent range measurement. The crossover method is a technique in which the angle is measured where protons inelastically scattered from the 9.63 MeV state of ^{12}C have the same energy as those scattered from hydrogen. This angle uniquely defines the incident energy of the proton beam. Measurements were made on both sides of the beam line so as to cancel out any asymmetries in the measurement. The protons scatterd from a polystyrene target were detected at an average crossover angle of 33.9±0.2° which corresponds to an incident proton energy of 33.4 ± .3 MeV. The detected proton's energy at this angle is ∿22.9 MeV and is easily stopped with a combination of a 3mm lithium drifted silicon detector together with a 770 micron surface barrier detector.

The energy was also measured by observing the protons elastically scattered from a ^{12}C target after they have passed through a precision ground aluminum block of thickness 1,165.4 ± .3 mg/cm^2. The protons passing through the block are detected by a silicon surface barrier counter.

Table 3 shows the average energy of the protons which were through the block as a function of the energy at which they enter it.

TABLE 3. Average energy (E_{AVG}) of protons emerging from the energy calibration block as a function of the energy at which they enter (E_{IN}).

E_{IN} (MeV)	E_{AVG} (MeV)
30.130	0.0
30.180	1.0
30.290	2.0
30.435	3.0

Notice that there is a magnification, $\Delta E_{AVG}/\Delta E_{IN} = M \simeq 8$ in the range ΔE_{AVG} = 1-3 MeV. This system yields a sensitive measure of the incident energy since any small change in the incident energy (δE_{IN}) is reflected as a measured change $\delta E_{AVG} = M \times \delta E_{IN}$. Measurements were made on both sides of the incident beam to eliminate asymmetries in the measurement. Once an angle vs. ΔE_{IN} in curve has been determined, reference to kinematic calculations for the reaction $^{12}C(p,p)$ yields the proton beam energy. The result for the method was $E_p = 33.6 \pm .2$ MeV. This method was then used as a rapid check on the incident energy for subsequent runs; the results for the incident energy always fell within 200 keV

of the above value. As can be seen, results from both methods agree to within their respective experimental errors.

3.B. Target Monitor

A cylindrically shaped cesium iodide crystal, 0.5 inches long and 0.25 inches in diameter, was mounted on a photomultiplier tube and placed at a fixed orientation relative to the incident beam, usually at 135° relative to the incident beam direction on the opposite side of the beam line from the movable ΔE-E detectors as shown in Figure 2. The pulses from protons elastically scattered from the target were selected out with a single channel analyzer and scaled. The ratio (R) was recorded for each run where,

$$R = \frac{Q}{M \cos \theta_T} \qquad (1)$$

Q = charge collected in Faraday cup (coul.).

M = number of elastically scattered protons detected by monitor.

θ_T = target angle (this term accounts for increased target thickness due to a change in the angle of the target).

Significant changes in R between runs can reflect the following experimental problems:

(1) a change in the target thickness due to the wandering of the beam spot over a non-uniform target.

(2) a malfunction of the target rotation mechanism.

(3) a malfunction in the charge integrator or the presence of an obstacle in front of the Faraday cup.

(4) destruction of a portion of the target.

In short, this additional counter monitors the performance of the target and charge collection devices. Typical figures from the experiment, $^{7}Li(p,d)^{6}Li$, are given below.

R (measured) = $(.962 \times 10^{-10})$ $\pm 3.2\%$

Considering the uncertainty in the target angle (θ_T), the accuracy of the charge integration circuitry, and the statistical uncertainty in M, the calculated uncertainties are:

uncertainty for forward angles = $\pm 2.1\%$

uncertainty for backward angles = $\pm 3.7\%$

The importance of using the monitor is realized if the ratio R is calculated and compared after every run to provide the experimenter with an up-to-date measure of the state of the target and charge integrator system.

3.C. Differential Cross Section

The differential cross section ($\frac{d\sigma}{d\Omega}(\theta)$) for A(p,d)B is defined [45] for solid targets by the expression (2).

$$(2) \quad \frac{d\sigma}{d\Omega}(\theta) = \frac{n_d}{N_o T d\Omega} \quad (cm^2/sr)$$

where n_d = no. of counts in the deuteron group corresponding to the state, B.

N_o = no. of protons incident on the target.

T = no. of target atoms/cm^2

$d\Omega$ = solid angle subtended by the detector.

This expression can be expressed in terms of directly measurable variables with the result (3),

$$\frac{d\sigma}{d\Omega}(\theta) = 3.386 \times 10^{-7} \frac{n_d R^2 a \cos\theta_T}{Q \gamma d^2} \quad (mb/sr) \tag{3}$$

where R = distance from target to detector (in).

d = diameter of detector collimator (in).

a = gm. mol. wt.of target (gm/mole)

θ_T = target angle (see Fig. 2)

Q = collected charge in Faraday cup (microcoulombs)

γ = target thickness (mg/cm^2).

A list of the estimated uncertainties for those quantities for which the uncertainty is $\geq$ 1.0% is given in Table 4.

The uncertainty in the detector angle must also be considered, but its effect on the uncertainty in the cross section depends on the value of $\frac{d}{d\theta}(\frac{d\sigma}{d\Omega})$. For angular distributions with steep slopes, such as the forward angles of the ^{9}Be ground state distribution; this correction is as large as ±4%; for relatively flat distributions, the correction is negligible.

TABLE 4.--Estimated uncertainties in parameters related to the measurement of the differential cross section. Two values representing the extremes are given when the uncertainty varies considerably between particular experiments.

Quantity	Uncertainty
n_d	3.2%
R^2	1.3%
$\cos \theta_t$	2.2% (30°); 3.5% (45°)
Q	1.0%
d^2	1.3%
γ	2% (^{9}Be); 7% (^{11}B)

The estimate for the total uncertainty in $d\sigma/d\Omega$ falls between ±6% to ±9% for the individual experiments. These figures do not include contributions from the uncertainty in separating the deuteron peak from the background. In general, however, the differential cross sections measured at forward angles with little background and small target angles have an uncertainty of ±6% to 8%, whereas in the backward angle measurements the uncertainty due to peak stripping is significant and the measurements of the differential cross section are accurate to within ± 7% to 12%.

3.D. Energy Resolution

The deuteron energy resolution varied between 100 keV (mylar calibration spectrum, see Fig. 6) to 160 keV (^{11}B) with typical figures of 120 keV. Main contributions to

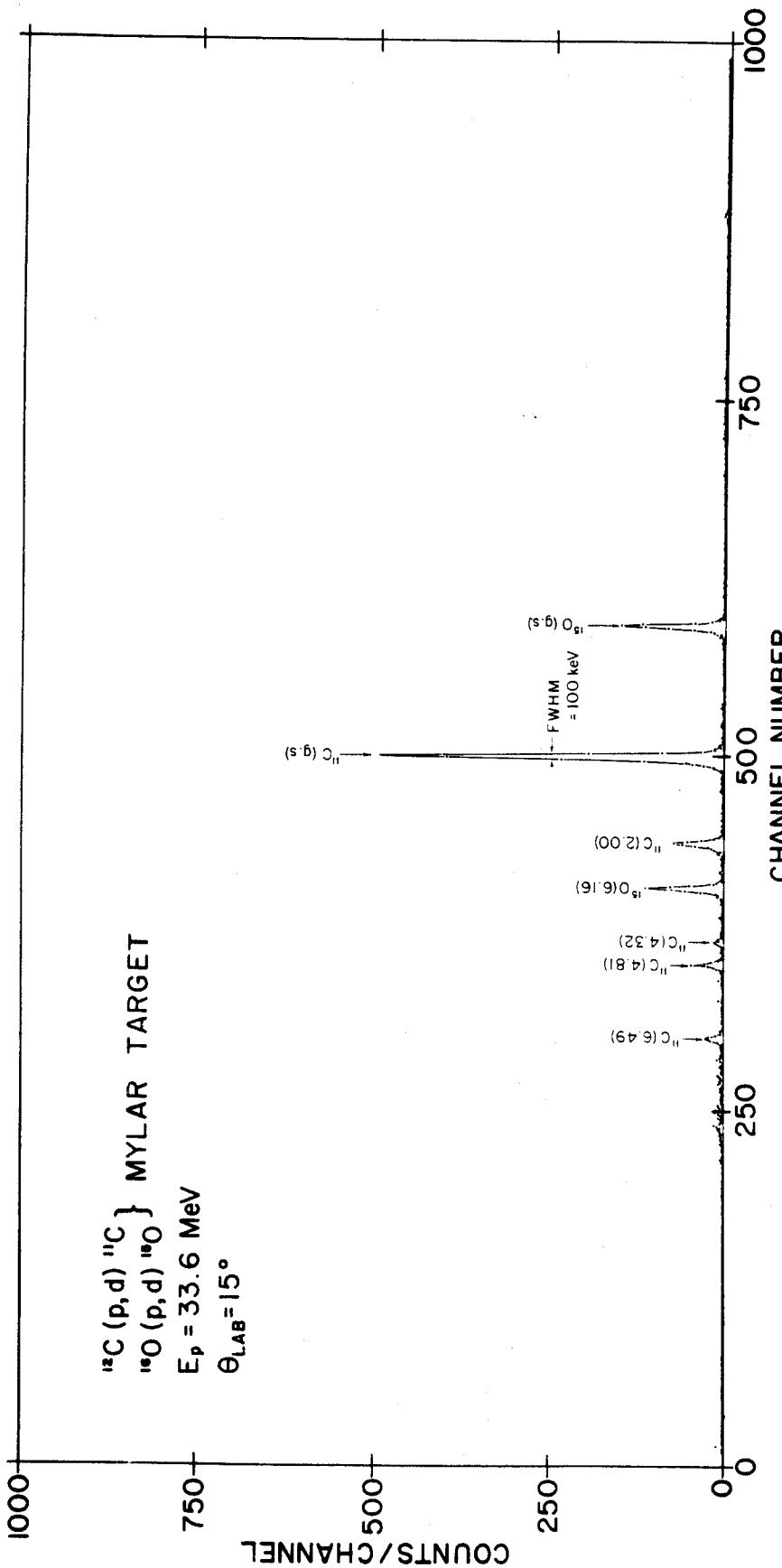

Figure 6.--$^{12}C(p,d)^{11}C$ deuteron spectrum at 15 degrees. The target was a 1.03 mg/cm^2 Mylar foil; this thickness represents ~ 45 keV energy loss to 19 MeV deuterons. Overall energy resolution in the neighborhood of 100 keV is indicative of single-turn extraction as the individual turns are separated by ~ 80 keV.

this figure come from electronic noise, incident beam resolution, target thickness, and detector resolution. Electronic noise for the entire system from the counters to the E +ΔE output was ∿70 keV. Assuming single turn extraction and less than 6° phase width, the best estimates of the cyclotron designers place the energy resolution of the 34 MeV proton beam at ∿35 keV. The target thickness introduces a spread in the energy of the outgoing deuterons of ∿55 to 75 keV depending on the particular target in use. Since the proton beam cannot be magnetically analyzed at the present time, no accurate figure can be obtained for the detector resolution, but the combined effect of detector resolution plus incident beam resolution introduced an energy spread on the order of 75 keV.

CHAPTER 4

EXPERIMENTAL RESULTS

4.A. $^{6}Li\ (p,d)^{5}Li$

Figures 7 and 8 show deuteron energy spectra taken at lab angles of 15°, 35°, and 120° which show deuteron groups corresponding to the ground state ($J^{\pi} = 3/2^{-}$) and 16.60 MeV state ($J^{\pi} = 3/2^{+}$) of ^{5}Li. The location of the broad ground state of ^{5}Li (Γ = 1.3 - 1.4 MeV) just above the α + p separation energy (Fig. 9) is an inducement to use a simple cluster model [46] description of the state, consisting of an alpha particle coupled to a proton with orbital angular momentum ℓ = 1. Possible spin and parity assignments for this configuration are $3/2^{-}$ and $1/2^{-}$. A very broad $1/2^{-}$ level (Γ = 3-5 MeV) has been reported at an excitation energy of 5 to 10 MeV [10]. A deuteron group corresponding to this level has not been identified in the energy spectra, but because of its large width, it may be impossible to isolate it from the background due to three body breakup. It is also possible that a significant fraction of the yield of this $1/2^{-}$ level lies below 5 MeV excitation energy, and that the deuterons corresponding to this state have been included in the tail of the ground state peak.

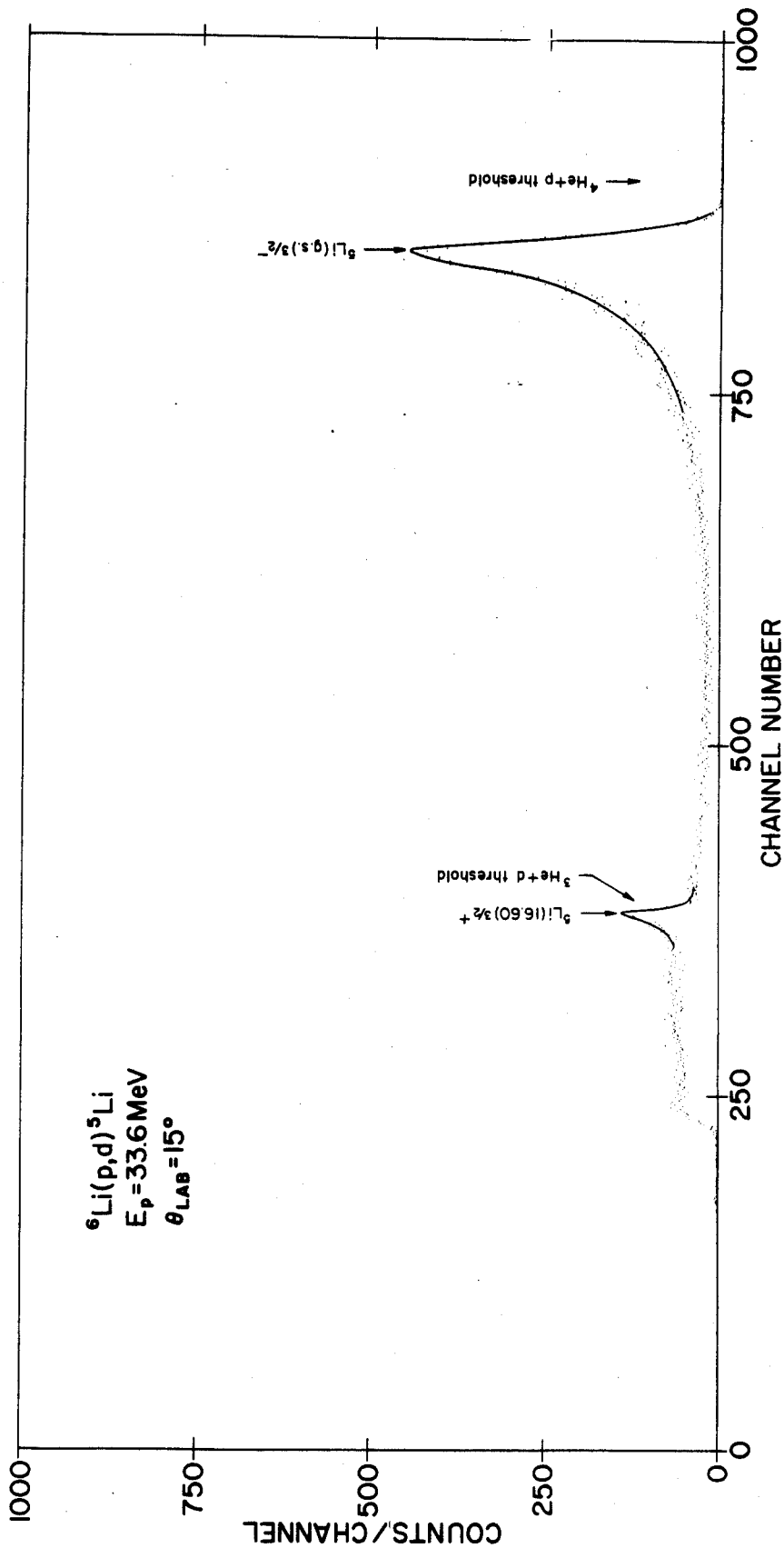

Figure 7.--^{6}Li(p,d)^{5}Li deuteron spectrum at 15 degrees. The long tail on the ground state peak may include a contribution from a previously reported $J^\pi = 1/2^-$ state.

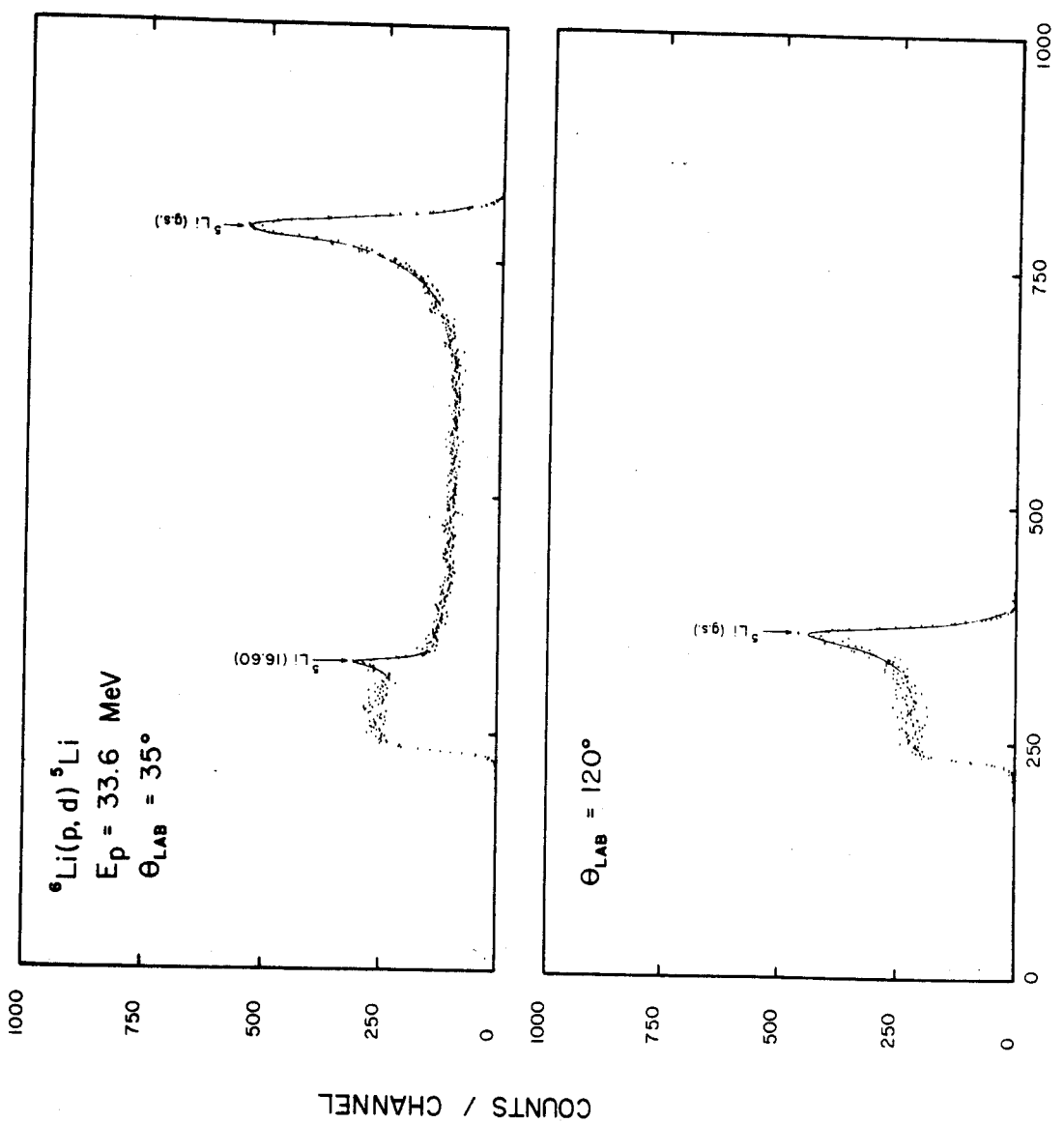

Figure 8.--^{6}Li(p,d)^{6}Li deuteron spectra at 35° and 120°.

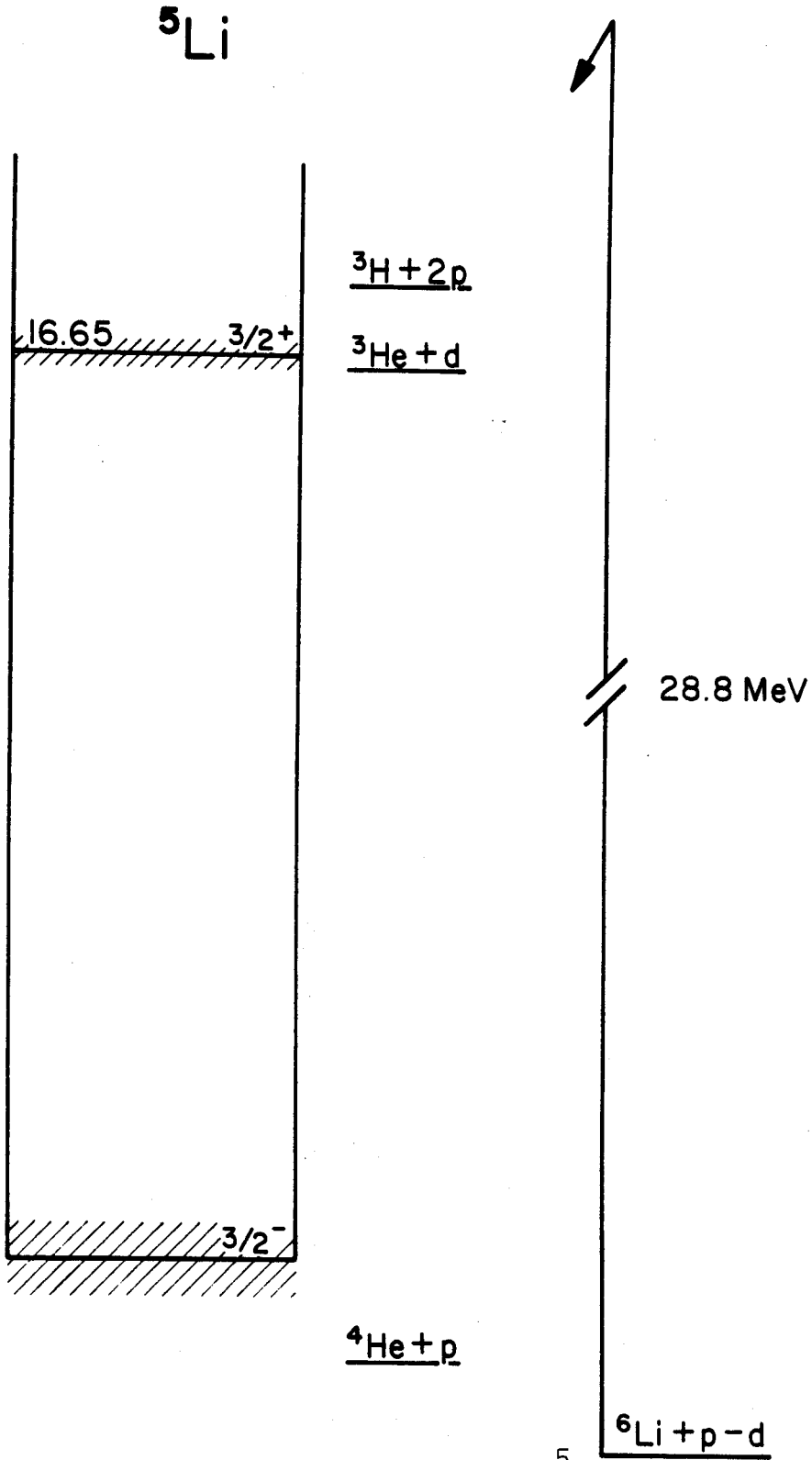

Figure 9.--Energy level diagram of ^{5}Li. Only the states observed in the ^{6}Li (p,d)^{5}Li reaction are shown and the excitation energies listed are those measured in this reaction.

No other levels have been reported [6] below the relatively narrow (Γ = 360 keV) 16.6 MeV state which lies just above the ^{3}He + d separation energy as shown in Fig. 9. There, in a situation analogous to that of the ground state, a simple cluster model description consisting of a ^{3}He nucleus coupled to a deuteron with ℓ = 0 seems appropriate for this state. The above configuration allows J^π values of $3/2^+$ and $1/2^+$.

The 16.6 MeV level of ^{5}Li($J^\pi = 3/2^+$) was strongly excited in this reaction and a search was made in the vicinity of this peak in order to detect the presence of the $1/2^+$ member of the doublet. Various incident proton energies were tried between 30 and 40 MeV, as this was the experimentally obtainable range of energies where the available phase space for competing three body breakup was calculated to be smallest [47]. No evidence was found that would locate the excitation energy of the $1/2^+$ level. There was also no indication that a ($3/2^+$, $5/2^+$) state previously reported at 20 MeV excitation is excited in this reaction [48].

Figure 10 shows a comparison of the angular distributions for the reaction ^{6}Li(p,d)^{5}Li (g.s.) calculated using the distorted wave Born approximation assuming the neutron was picked up from the 1s, 1p, and 1d shells (orbital angular momenta ℓ_n = 0,1 and 2, respectively). In the same figure it can be seen that the experimental angular distribution for the ground state of ^{5}Li shows a characteristic shape for transfer of a neutron from the 1p shell (ℓ_n = 1) by a direct

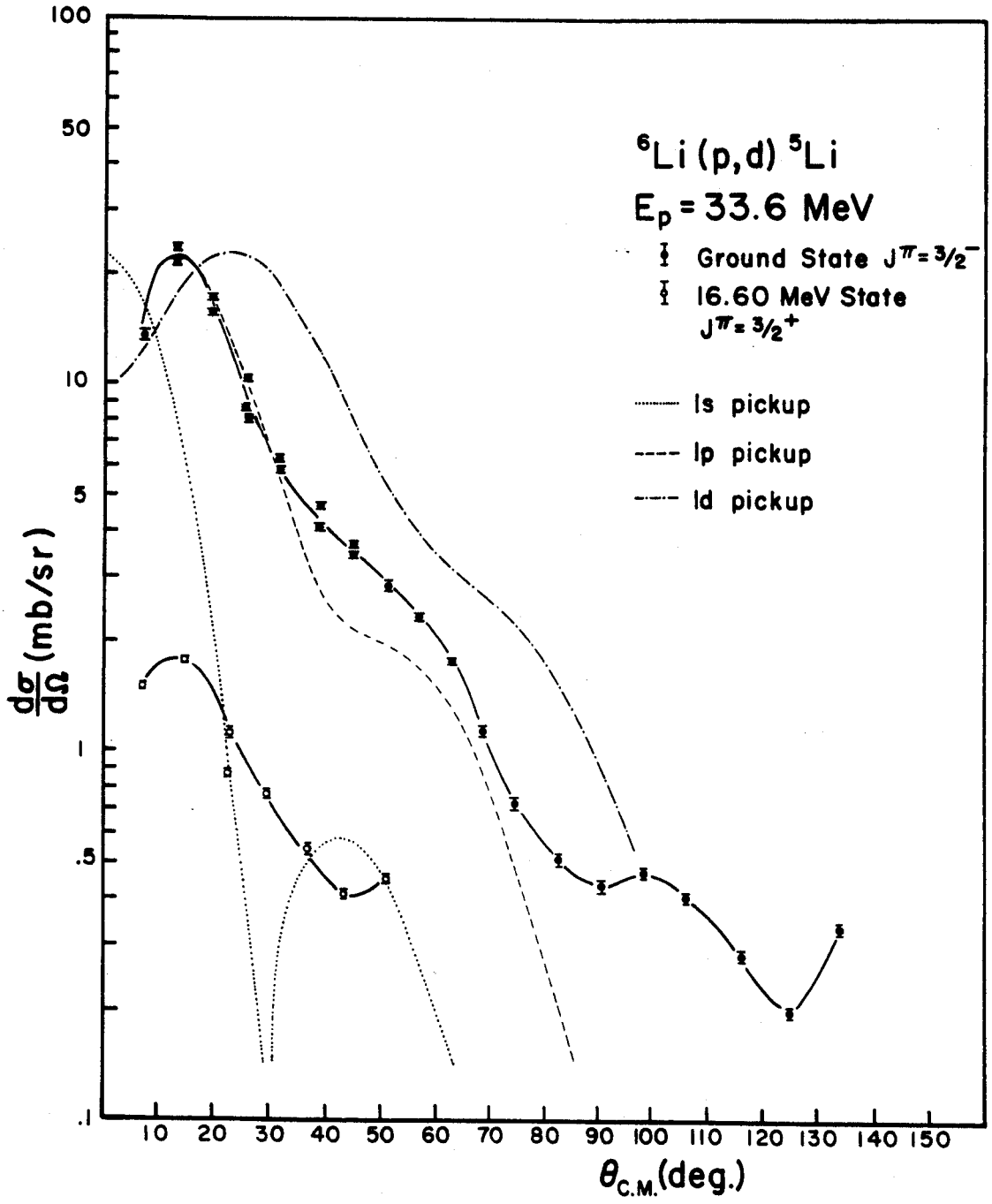

Figure 10.--$^{6}Li(p,d)^{5}Li$ angular distributions. The error bars shown only represent the uncertainty due to statistics and the solid lines are drawn to guide the eye. The dashed line shows the DWBA fit to the ground state differtial cross section.

reaction mechanism (Fig. 10.). For Q values in the range 0 to -20 MeV, the angular distribution has a first peak in the neighborhood of 10° (center of mass angle) for the pick-up of a 1p shell neutron from a target with A = 6 to 11. Angular distributions for the same cases involving the pickup of a 1s neutron or a 1d neutron have a first peak at 0° and approximately 20° respectively. The angular distribution for the 16.6 MeV state could not be obtained for lab angles greater than 35° because the deuteron peak could not be distinguished from a strong background due to three body breakup. This state is excited by the pickup of a 1s neutron from ^{6}Li but, due to the small amount of data, little can be said concerning the shape of the angular distribution.

4.B. ^{7}Li(p,d)^{6}Li

Four deuteron groups were observed in the energy spectra from the ^{7}Li (p,d)^{6}Li reaction corresponding to states of ^{6}Li at 0.0, 2.15, 3.57 and 5.38 MeV excitation energy (Figs. 11 and 12). A small peak corresponding to the ground state of ^{15}O indicates the presence of a small amount of oxygen contamination on the target (less than 1.5%). No evidence for any other strongly excited states was found up to 18 MeV of excitation energy for ^{6}Li. Deuteron groups corresponding to the positive parity states of ^{6}Li at 4.57 and 6.0 MeV were not observed; however, these states are broad and if weakly excited the peaks

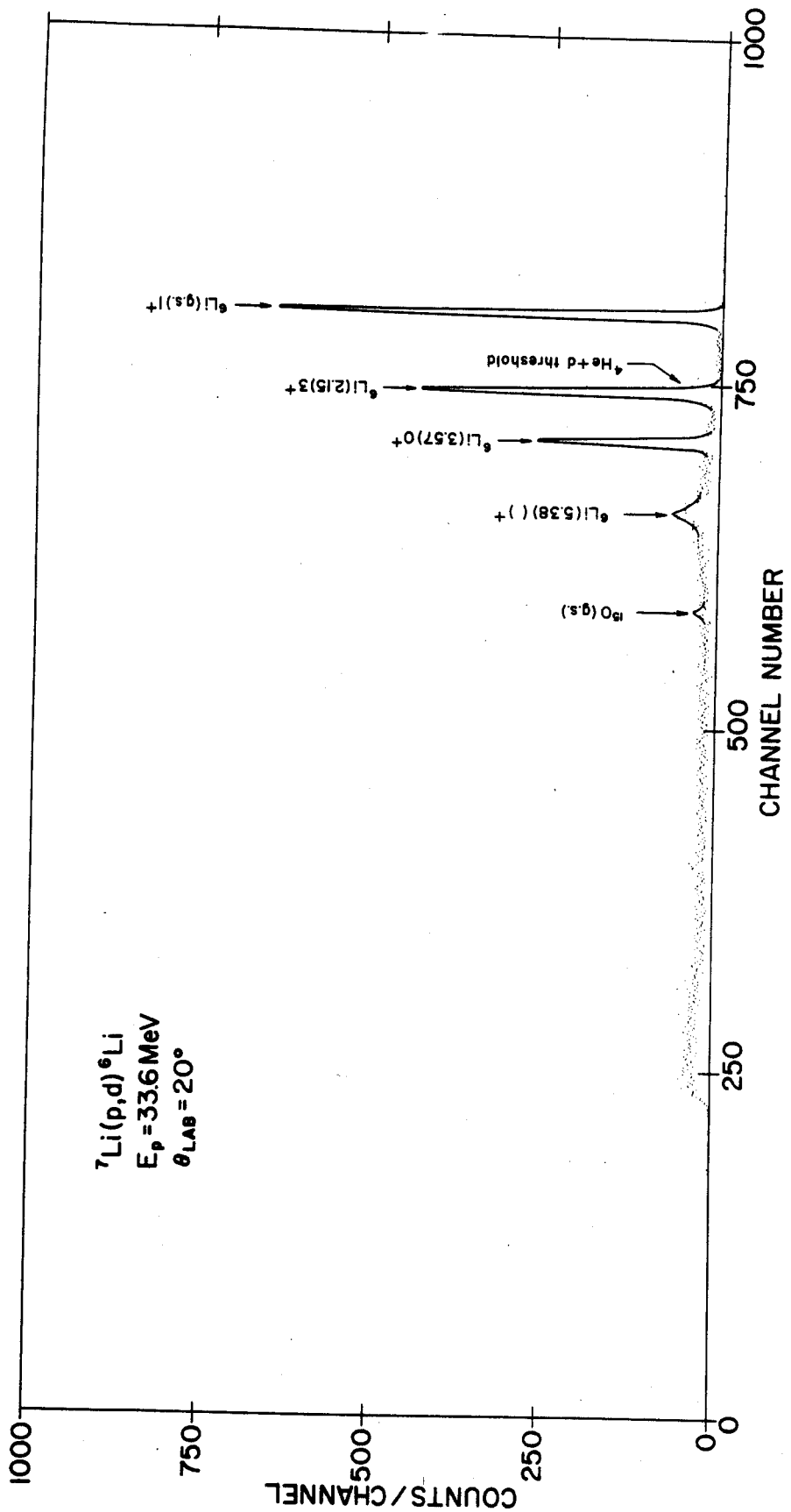

Figure 11.--^{7}Li(p,d)^{6}Li deuteron spectrum at 20 degrees. A small peak due to ~ 1.5% oxygen contamination can be seen.

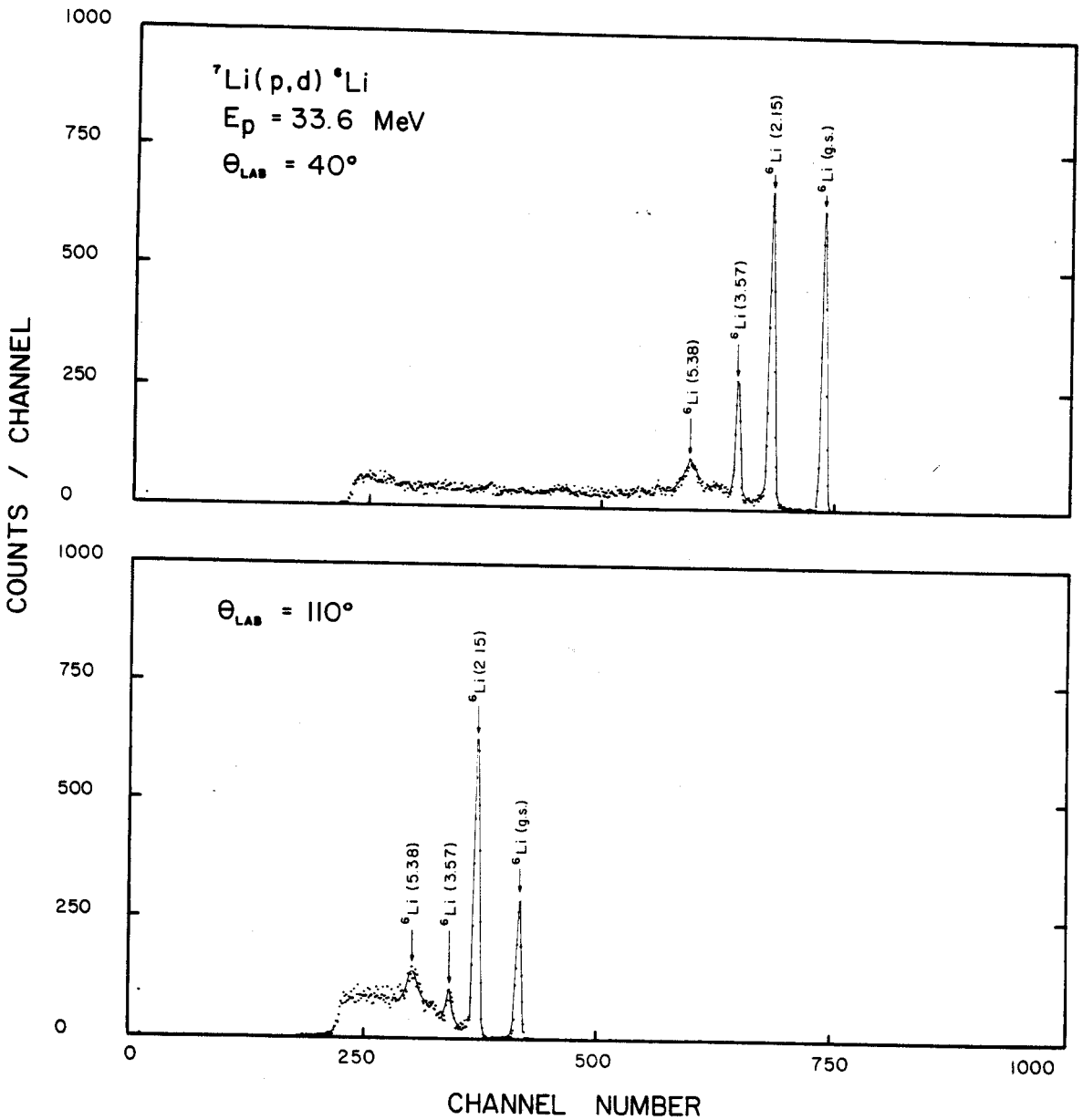

Figure 12.--^{7}Li(p,d)^{6}Li spectra at 40° and 110°.

would be difficult to extract from the background. The shapes of the angular distributions for the 0.0, 2.15, 3.57 and 5.38 MeV states are characteristic of $\ell_n = 1$ pickup (see Fig. 13). This fixes the relative parity between the initial and final state [49], in particular, this assigns a positive parity to the 5.38 MeV level. A positive parity fits in with the tentative T = 1 isospin assignment [10] for this state and places it in the isospin multiplet of which 1.80 MeV state of ^{6}He($J^\pi = (2)^+$) is a member.

It is interesting to note that the slopes of the first peak of the angular distributions for the T = 0 states at 0.0 and 2.15 MeV are much steeper than those of the lowest T = 1 states at 3.57 and 5.38 MeV. This may have some implication concerning the isotopic spin dependence of the reaction mechanism.

4.C. ^{9}Be(p,d)^{8}Be

The energy spectra from the reaction ^{9}Be(p,d)^{8}Be (see Figs. 14 and 15) show deuteron groups corresponding to strongly excited levels of ^{8}Be at 0.0, 3.1, 11.4, 16.95, 17.62, 18.18 and 19.21 MeV. A very small yield was observed for excited states of ^{8}Be at 16.6 and 19.15 MeV. The first three levels of ^{8}Be can be understood, at least qualitatively, by a cluster model of two alpha particles excited into the rotational sequence 0^+, 2^+ and 4^+ (Fig. 16) [50]. Measurements of the differential cross section for the 11.4 MeV state ($J^\pi = 4^+$) were made from 40° to 140° in

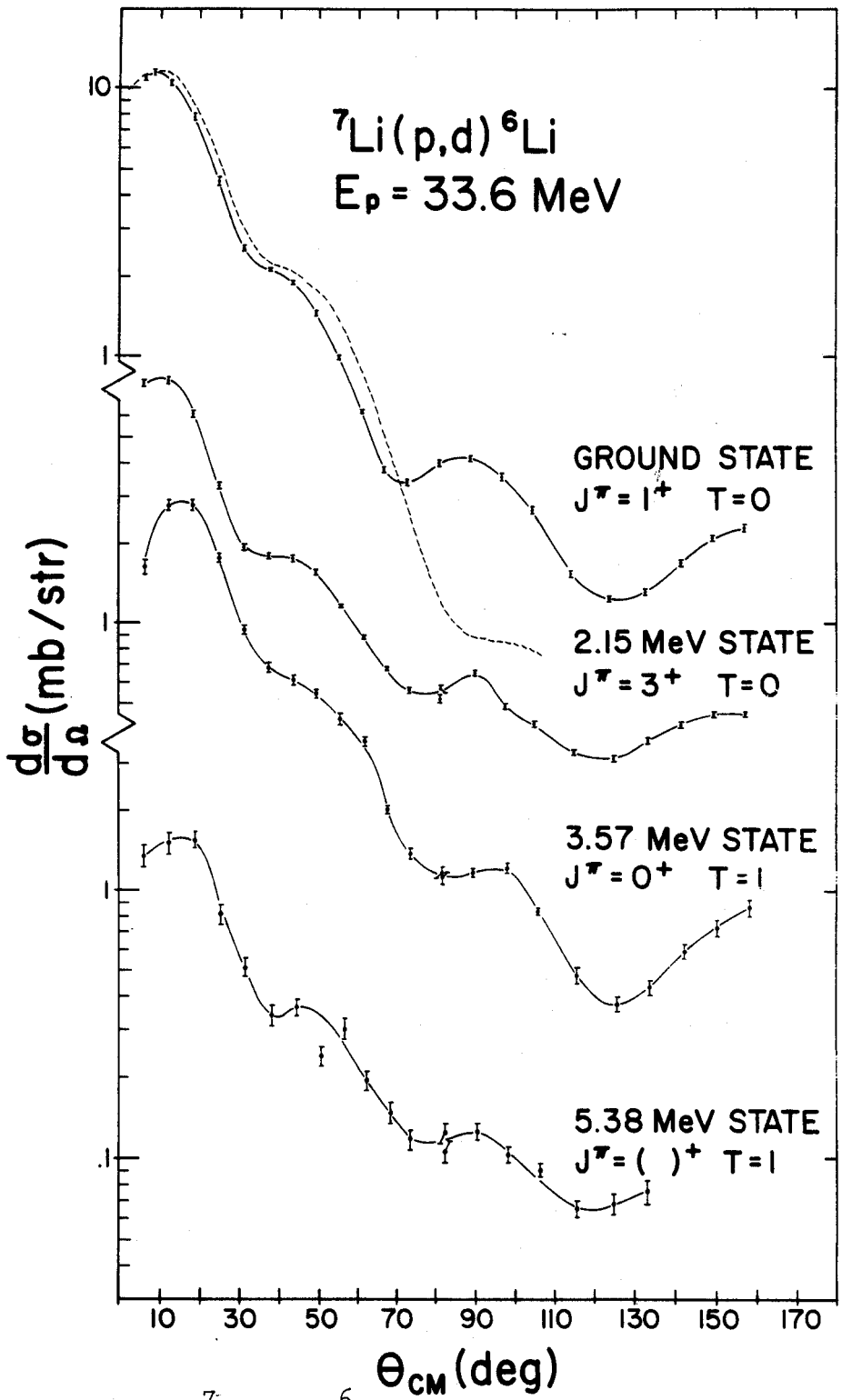

Figure 13.--^{7}Li(p,d)^{6}Li angular distributions. The DWBA fit to the ground state differential cross section is shown by a dashed line.

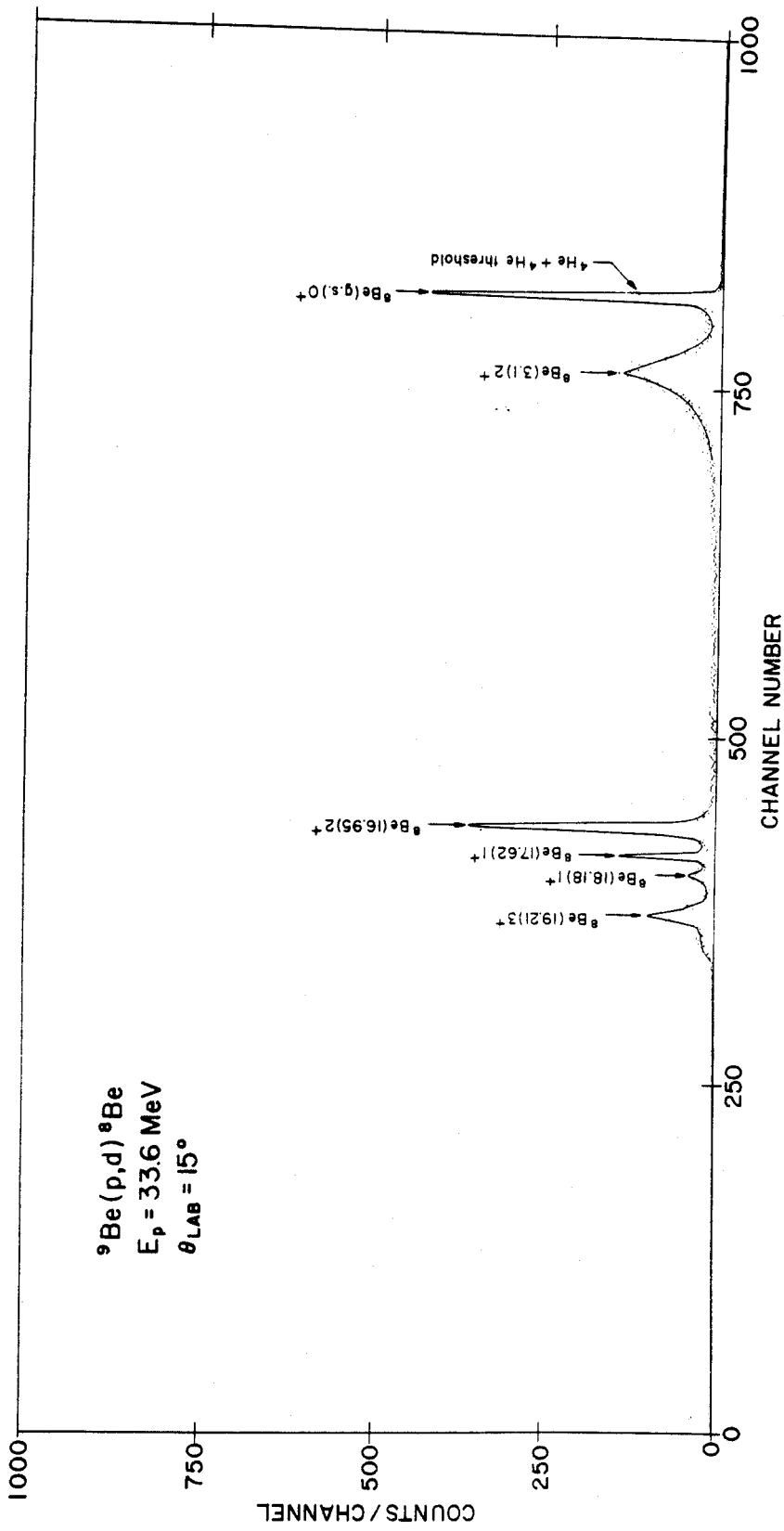

Figure 14.--^{9}Be(p,d)^{8}Be spectrum at 15°.

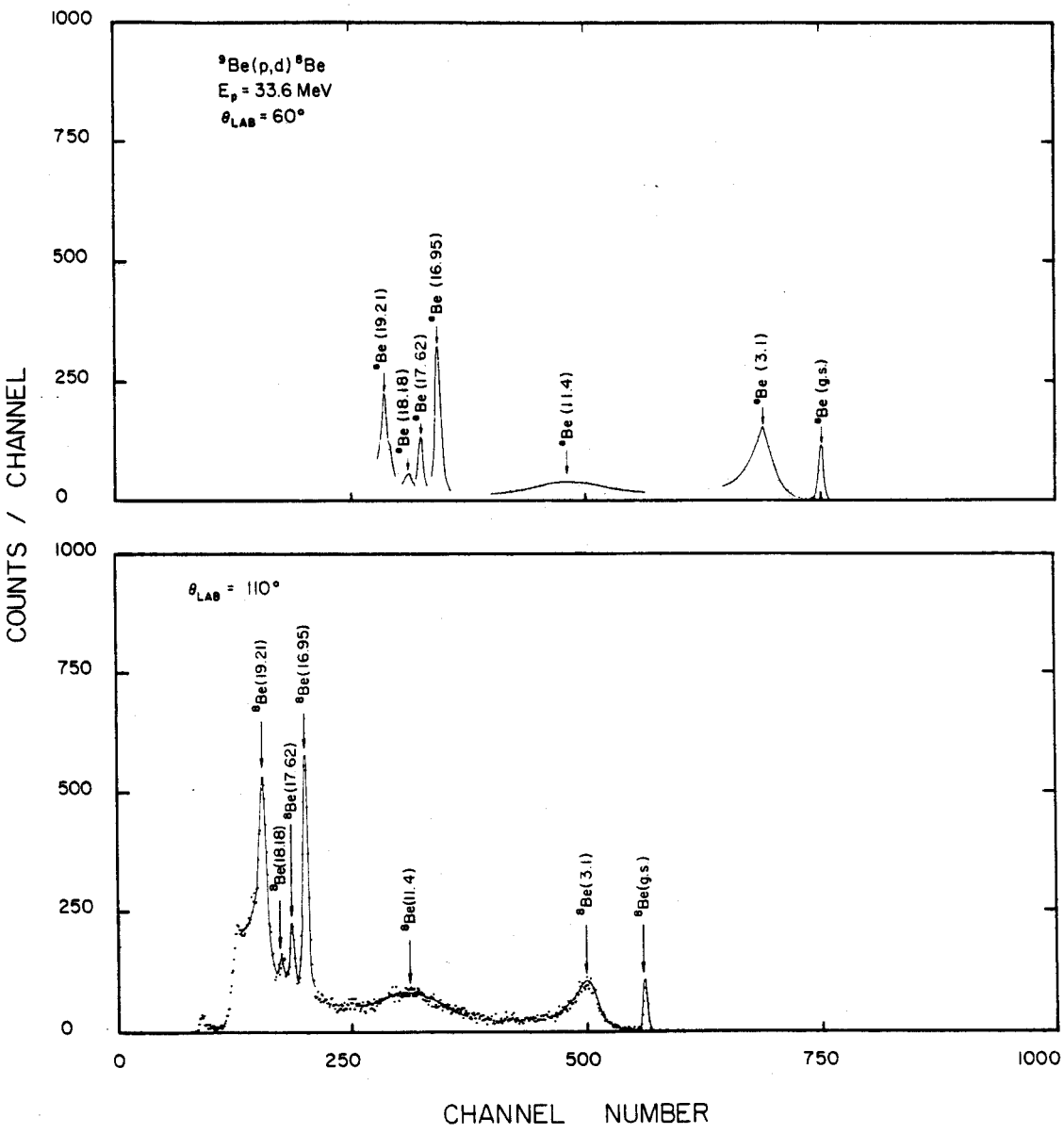

Figure 15.--^{9}Be(p,d)^{8}Be deuteron spectra at 60° degrees. The broad peak corresponding to the 11.4 MeV level of ^{8}Be can be clearly seen at back angles where its yield is comparable to that of the narrower levels.

the lab with a large uncertainty due to the width of the state ($\Gamma \sim 7$ MeV) [10] and a high background. The data show little structure in this range, the average value of the cross section falling between 0.02 and 0.05 mb/sr-MeV at the resonance. The angular distribution does not exhibit the forward peaking characteristic of a direct reaction, since the peak could not be seen at angles less than 35° (see Figs. 14 and 15). This leads to the conclusion that this state is excited principally by a compound nucleus mechanism and not by a direct process in which some 1f admixture in the ground state of ^{9}Be contributes to the cross section [13].

The next set of known levels of ^{8}Be appear in the region of the ^{7}Li + p and ^{7}Be + n separation energies (Fig. 16). Previous experimental evidence has established the fact that isospin mixing is present within each of the three doublets ($J^{\pi} = 2^{+}$, 1^{+} and 3^{+}) in this region of excitation energy [51,52,53,54,55]. Wave functions for these doublet states have been calculated by mixing intermediate coupling shell model wave functions of pure isospin with a charge dependent interaction [15]. The mixing coefficients were obtained by fitting existing experimental data and are given in Table 5. The ratio of spectroscopic factors S(16.6)/S(16.95) calculated using this model is 1/45 [17], whereas the ratio obtained experimentally is less than 1/20.

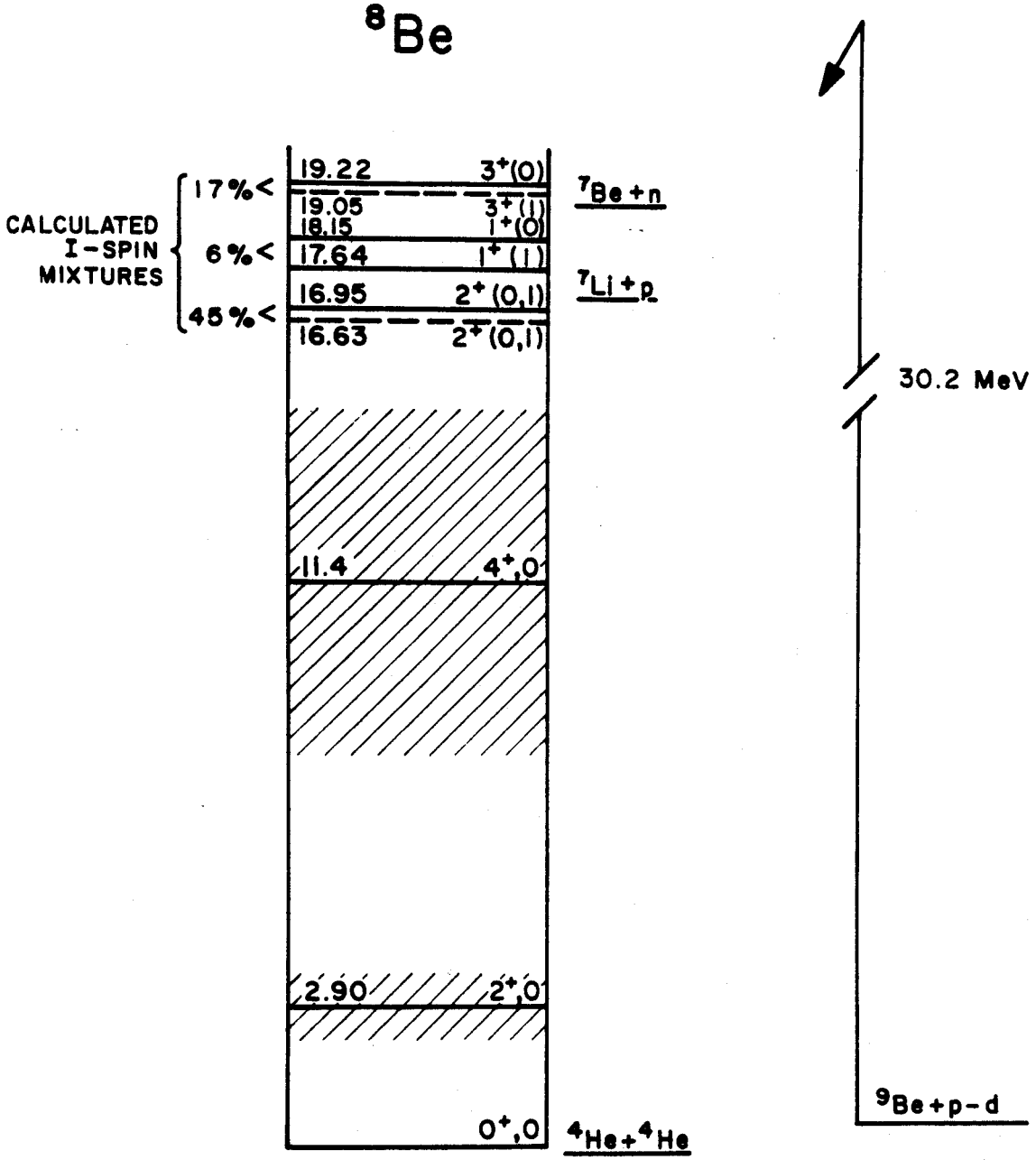

Figure 16.--Energy level diagram of ^{8}Be. The levels drawn in with dashed lines are those weakly excited in the ^{9}Be (p,d)^{8}Be reaction while those drawn in with the solid lines correspond to strongly excited levels. Also shown are the isospin admixtures which have been calculated for the J^{π} = 2^{+}, 1^{+} and 3^{+} doublets (17).

TABLE 5.--Experimental cross section ratios and isospin admixtures calculated by Barker [17] for the $J^{\pi} = 1^{+}$, 2^{+} and 3^{+} doublets.

Doublet	Ratio of cross sections (34 MeV)	Ratio of cross sections (41MeV) [51]	Isospin admixtures[a] (amplitude squared) as calculated by Barker [17]
(16.6)/(16.9)	<1/20	1/25	45%
(17.6)/(18.2)	2.6	3.5	6%
(19.1)/(19.2)	<1/20		17%

[a]50% admixture represents a doublet with maximal isospin mixing and 0% a doublet with states of pure isospin.

Some indication of the amount of isospin mixing within the doublets can be obtained if the single particle cluster model is used to describe the states [51]. In this case, the (p,d) reaction will excite only one member of the doublet if the pair is maximally mixed in isospin (50%). Conversely, if the members of the doublet are states of pure isospin (T = 0 or 1), both states should be observed by the (p,d) reaction with the same yield. Table 5 shows the data to be in general agreement with this simple model. The experimentally measured widths for the 16.95 and 19.21 MeV deuteron groups of 103 ± 15 keV and 208 ±30 keV, respectively, are in agreement with the previously obtained values [10] of 83 ± 10 keV and 190 keV insuring that only one of the states in these doublets is strongly excited. The

experimentally obtained cross section ratios for these doublets are in agreement with those obtained at E_p = 40 MeV [56].

The angular distributions for all strongly excited states of ^{8}Be (except for the above mentioned 4^+ state) exhibit the characteristic shape for ℓ_n = 1 pickup (Figs. 17 and 18). The differential cross section measurements for these states are in reasonable agreement with those obtained for E_p = 36 MeV [59]. The relative flattening of the differential cross sections as the excitation energy of the state increases is a Q value effect and was reproduced in the DWBA calculations.

4.D. ^{10}B(p,d)^{9}B

The deuteron energy spectra from the reaction ^{10}B(p,d)^{9}B are shown in Figures 19 and 20. Deuteron groups were observed corresponding to strongly excited levels of ^{9}B at 0.0, 2.33, 7.1, and 11.75 MeV and small deuteron yields were noted corresponding to weakly excited levels at 2.8 and 14.6 MeV. The very broad, weakly excited level observed with a ^{9}B excitation energy (E_x) of 14.6 MeV may correspond to the level observed at E_x = 14.9 MeV in the same reaction using 156 MeV protons [57]. With the higher incident proton energy, however, the 14.9 MeV level was observed to be strongly excited with a cross section comparable to that of ground state at forward angles, whereas the 34 MeV data show the 14.6 MeV level to have a cross section $\sim$1/10 that of the ground state at forward angles.

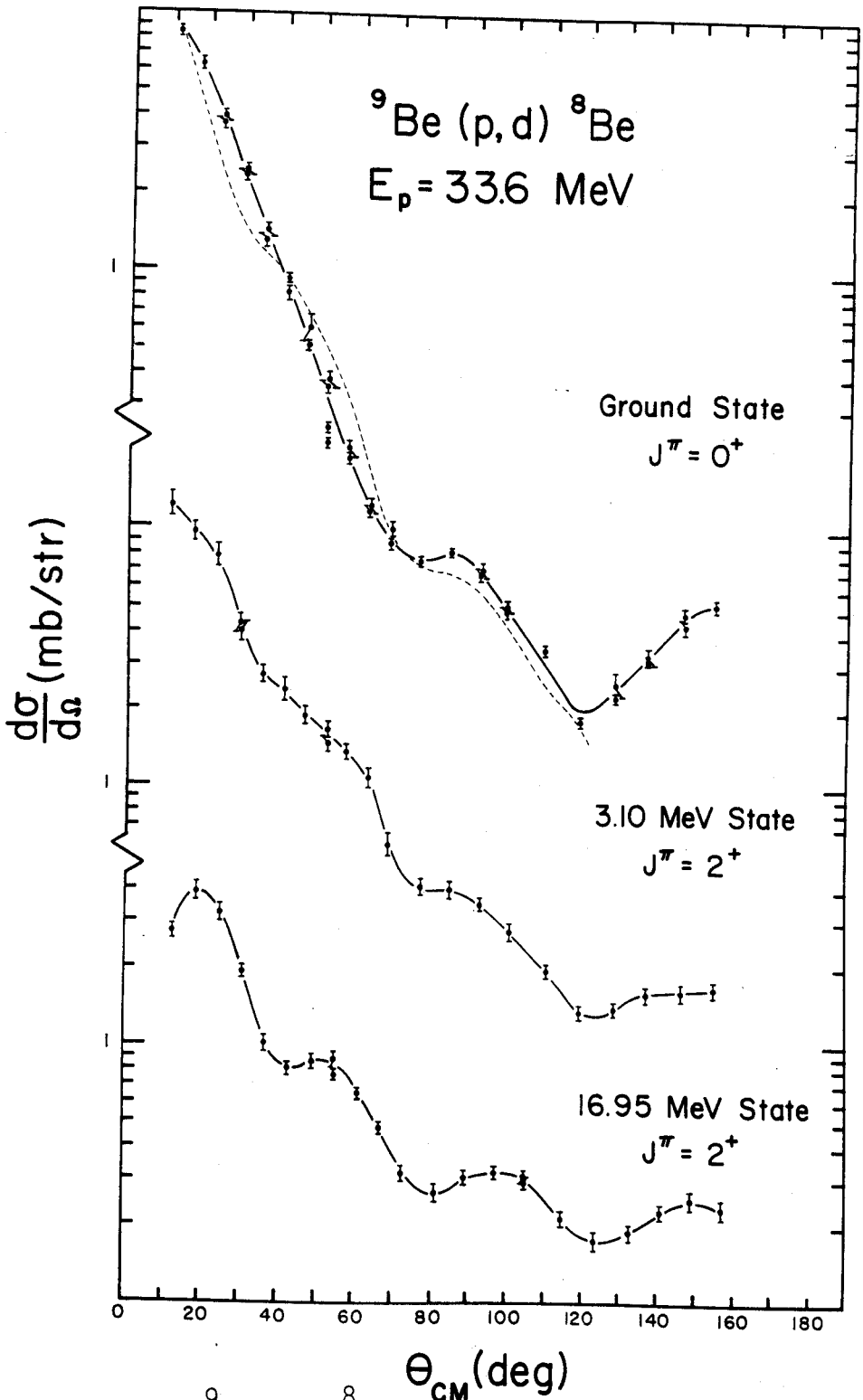

Figure 17.--^{9}Be(p,d)^{8}Be angular distributions for the 0.0, 3.1 and 16.95 MeV states of ^{8}Be. The DWBA fit to the ground state differential cross section is shown with a dashed line.

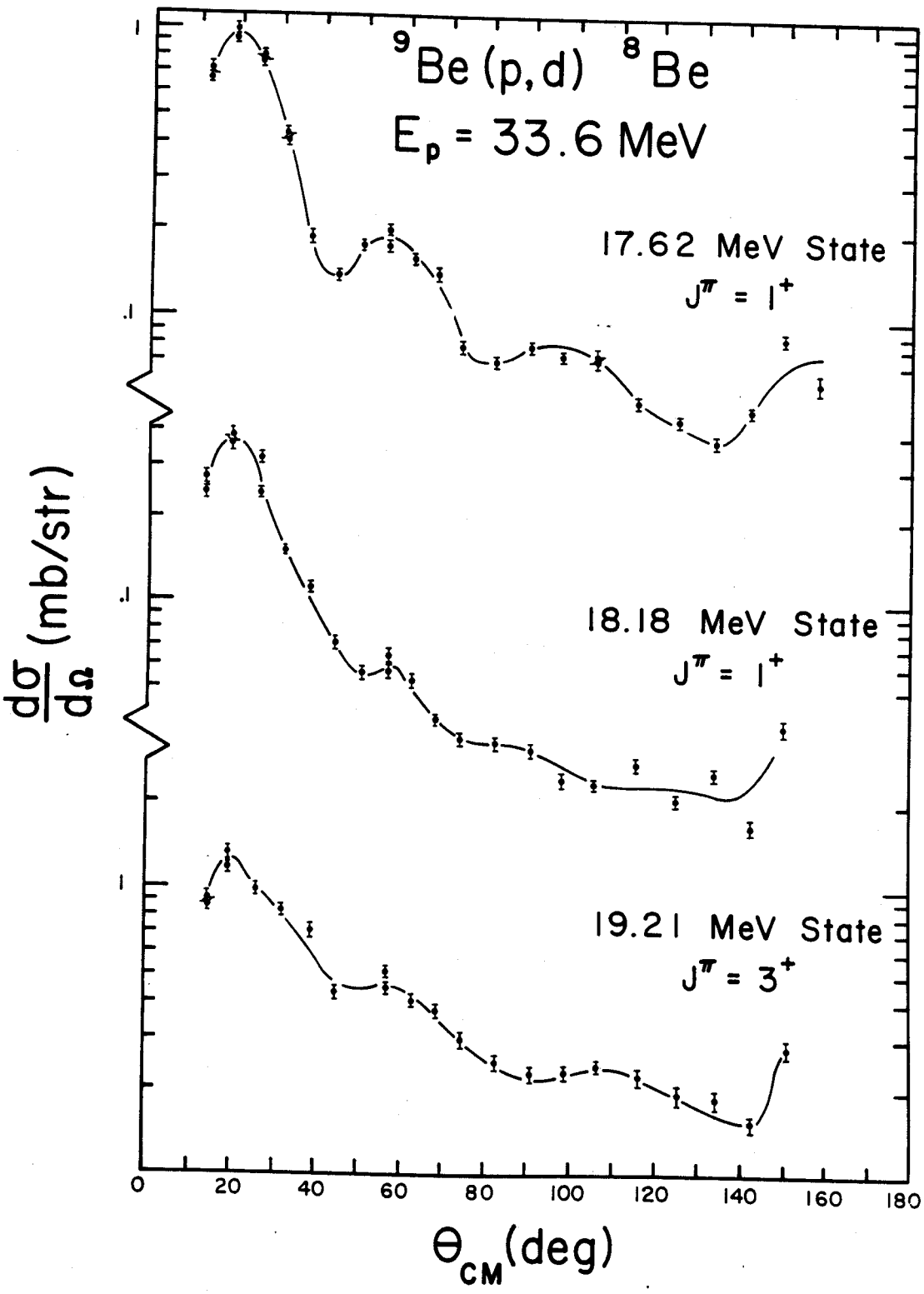

Figure 18.--^{9}Be(p,d)^{8}Be angular distributions for the 17.62, 18.18 and 19.21 MeV states of ^{8}Be.

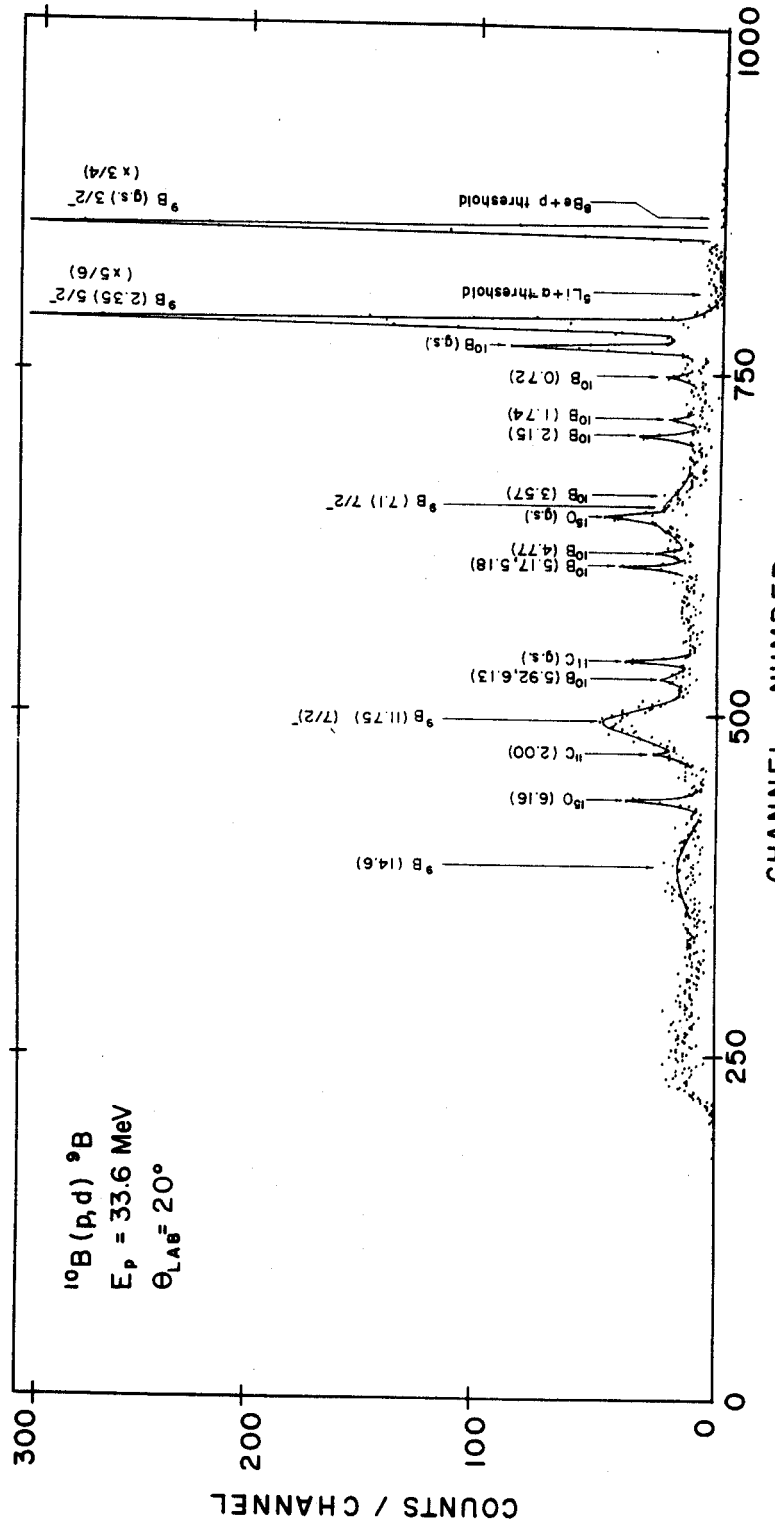

Figure 19.--^{10}B(p,d)^{9}B spectrum at 20 degrees. Deuteron groups can be seen due to ^{11}B(~8%) and ^{16}O(~1%) contaminants.

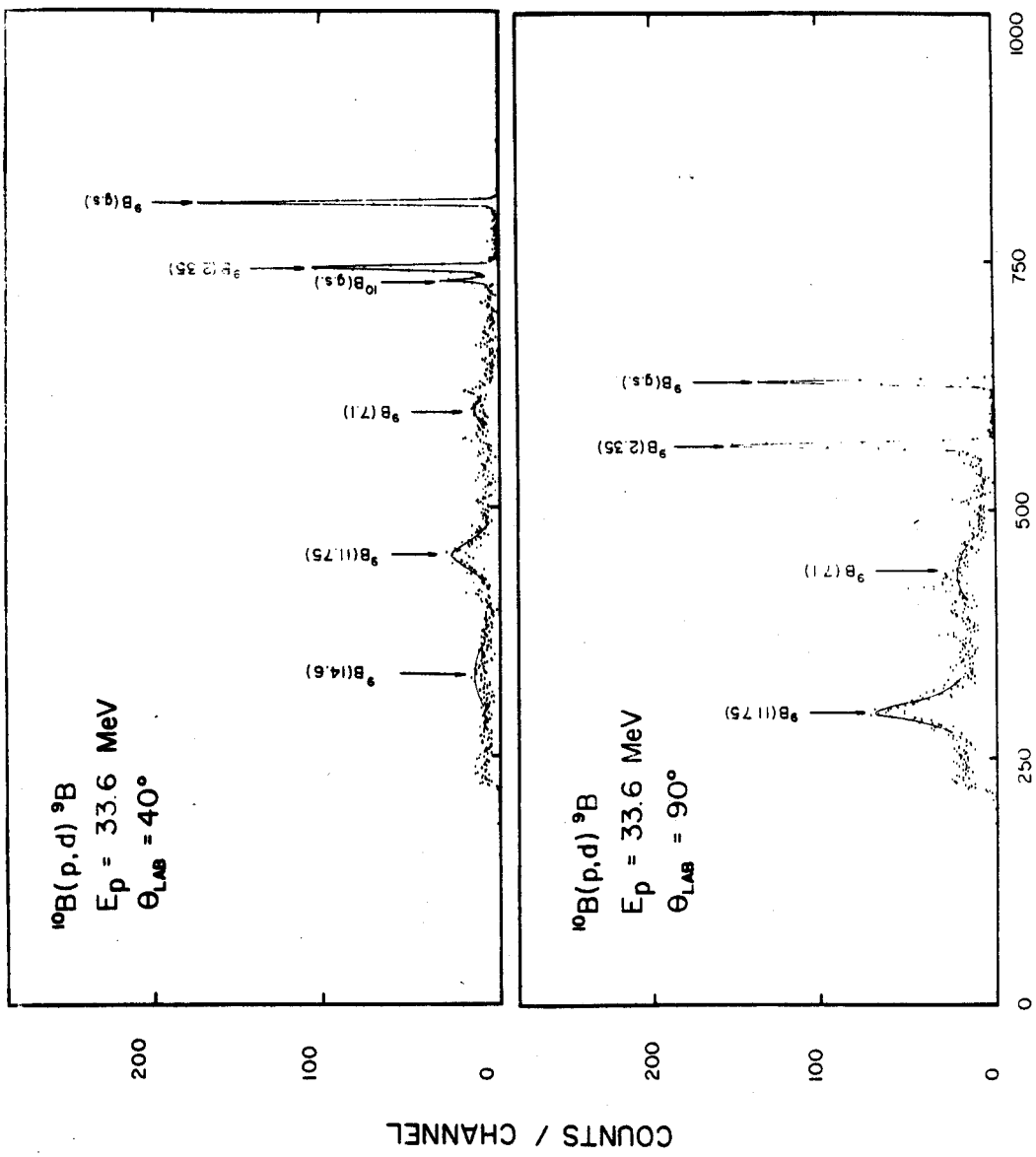

Figure 20.--$^{10}B(p,d)^{9}B$ spectra at 40° and 90°.

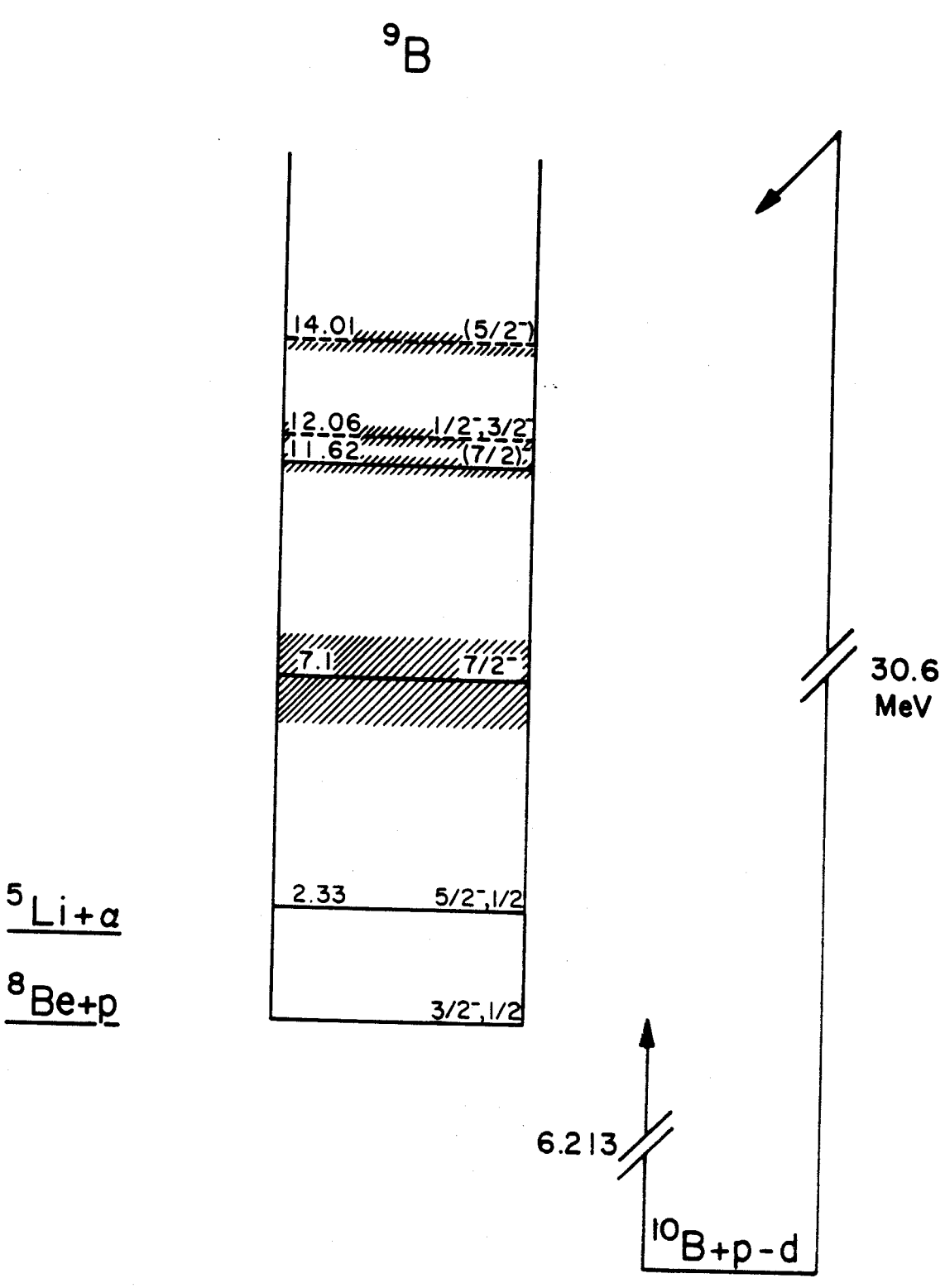

Figure 21.--Energy level diagram of ^{9}B. Weakly excited levels are drawn in with dashed lines; strongly excited levels are drawn in with solid lines. The very weakly excited positive parity ^{9}B level at ~2.8 MeV excitation is not shown.

A level at 9.7 MeV also reported to be strongly excited in the 156 MeV work was not observed to be excited in the 34 MeV data [57].

Two positive parity ^{9}B states at excitation energies of 1.5 MeV ($J^{\pi} = 1/2^{+}$) and 2.83 MeV ($J^{\pi} = 3/2^{+}, 5/2^{+}$) [10] are of special interest, since their presence in the spectra could denote the first evidence of 2s-1d shell admixtures in the ground state wave functions of stable nuclei with $A \leq 10$. No evidence was found for the excitation of the 1.5 MeV level which corresponds to the 1.67 MeV level of $^{9}Be(J^{\pi} = 1/2^{+})$, however results from the $^{10}B(p,d)^{9}B$ reaction using 11 MeV protons show a level at 1.7 MeV very weakly excited by a compound nucleus mechanism [58]. The present 34 MeV data do not rule out, on the basis of a statistical argument, the possibility of the same degree of excitation.

A small deuteron group (E_x = 2.8 MeV) with a differential cross section of approximately 120 μb/sr was observed at about 30° (center of mass angle), but it was difficult to follow over an extended range of angle because of the masking effect of levels arising from a ^{11}B impurity in the target (see Fig. 19). At 60°, the deuteron group corresponding to the 2.8 MeV level was not masked by the deuteron groups arising from the ^{11}B impurities, but was not observed. This could signify a rapidly decreasing cross section typical of a direct reaction process and therefore open the possibility for an observable 2s-1d shell admixture in the ground state wave function of ^{10}B. The evidence, however,

is scanty at best and the only definite conclusion one can draw is that any 2s-1d admixture in the ^{10}B ground state is very small.

A single strong deuteron group was observed corresponding to an excitation energy of 11.75 MeV in ^{9}B. There are two previously reported states at 11.62 MeV (J^{π} = ?) and at 12.06 MeV excitation (J^{π} = $1/2^{-}$, $3/2^{-}$) [10] allowing two possible explanations for the data: (1) the 12.06 MeV state has J^{π} = $1/2^{-}$ and cannot be excited by a direct reaction process due to angular momentum selection rules. In this case the single observed level has a measured excitation energy of 11.75 $\pm$ .1 MeV as compared with a previously determined energy of 11.62 $\pm$ .1 MeV [10]. (2) the 12.06 MeV level has J^{π} = $3/2^{-}$ and is weakly excited in the reaction causing the centroid of the doublet peak to be shifted up in excitation energy from the strongly excited level at 11.62 MeV to the observed value of 11.75 MeV. The first explanation seems to be the more likely one, since the deuteron group shows no sign of a doublet structure over a wide range of angle and the observed width of 800 $\pm$ 150 keV is close to the previously reported width for the 11.62 MeV level of 700 $\pm$ 100 keV [10].

Strongly excited levels of ^{9}B at 0.0, 2.33, 7.1, and 11.75 MeV excitation all have angular distributions with shapes characteristic of neutron orbital angular momentum transfer ℓ_n = 1 (see Figs. 22 and 23) and the parity of

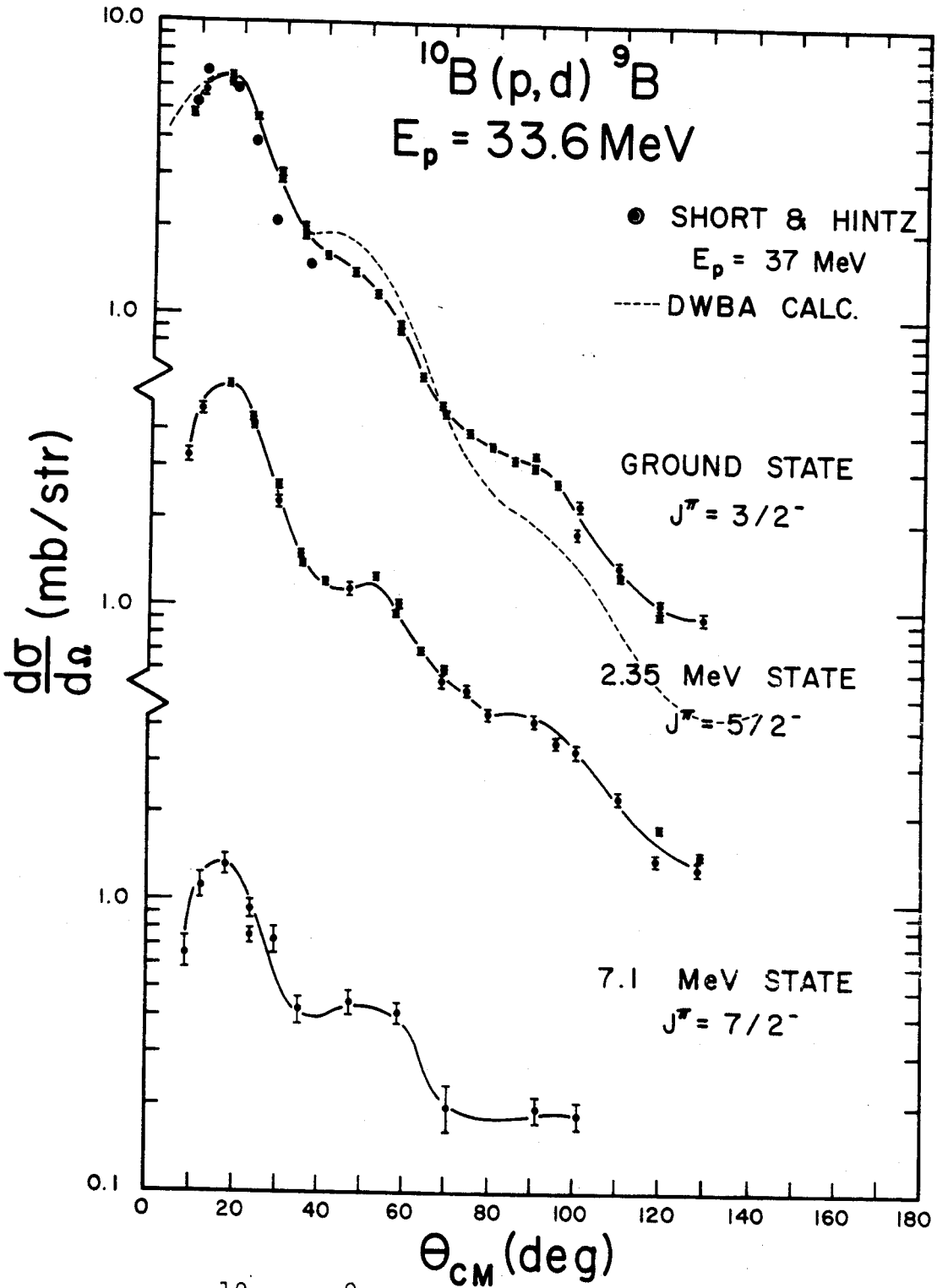

Figure 22.--$^{10}B(p,d)^{9}B$ angular distributions for the 0.0, 2.35, and 7.1 MeV states of ^{9}B. The DWBA fit to the ground state differential cross section is shown with a dashed line.

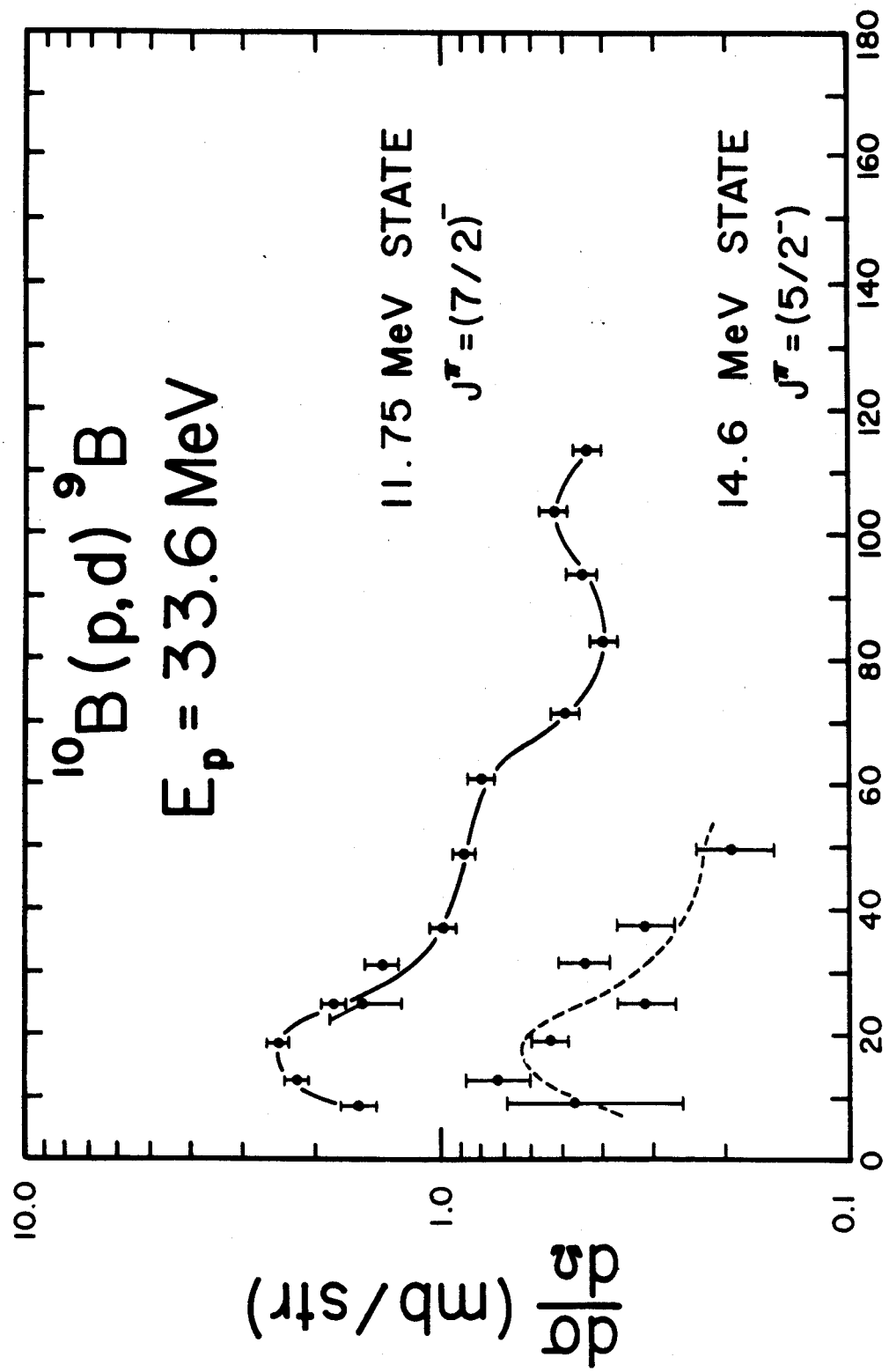

Figure 23.--$^{10}B(p,d)^{9}B$ angular distributions for the 11.75 and 14.6 MeV states. The dashed line drawn through the 14.6 MeV level data points has approximately the same shape as that drawn for the 11.75 MeV level.

these levels is negative. Poor statistics for the 14.6 MeV level data do not allow the definite assignment of the picked up neutron's orbital angular momentum, however the dashed curve in Figure 23 is approximately the same shape as that observed for the 11.75 state and shows that an $\ell_n = 1$ assignment is a reasonable possibility for this state. The angular momentum assignments for these states have been made on the basis of the measured spectroscopic factors for these levels and will be discussed in Chapter 6. Table 6 is a list of the measured excitation energies and line widths for the observed levels of ^{9}B.

TABLE 6.--Measured ^{9}B excitation energies and widths for deuteron groups observed in the reaction $^{10}B(p,d)^{9}B$.

Excitation energy (MeV)	Width (MeV)
0.0	∿0
2.35 ± .02	
7.1 ± .2	1.95 ± .2
11.75 ± .1	0.850 ± .050
14.6 ± .2	1.35 ± .2

4.E. $^{11}B(p,d)^{10}B$

The deuteron energy spectra from the $^{11}B(p,d)^{10}B$ reaction (see Figs. 24 and 25) show deuteron groups corresponding to strongly excited levels of ^{10}B with excitation energies of 0.0, 0.72, 1.76, 2.15, 3.57, 4.75, 5.18, and 6.04 MeV; levels of ^{9}B with excitation energies of 6.57 and 7.5 MeV were observed. The deuteron group corresponding to a ^{10}B excitation energy of 5.18 MeV could

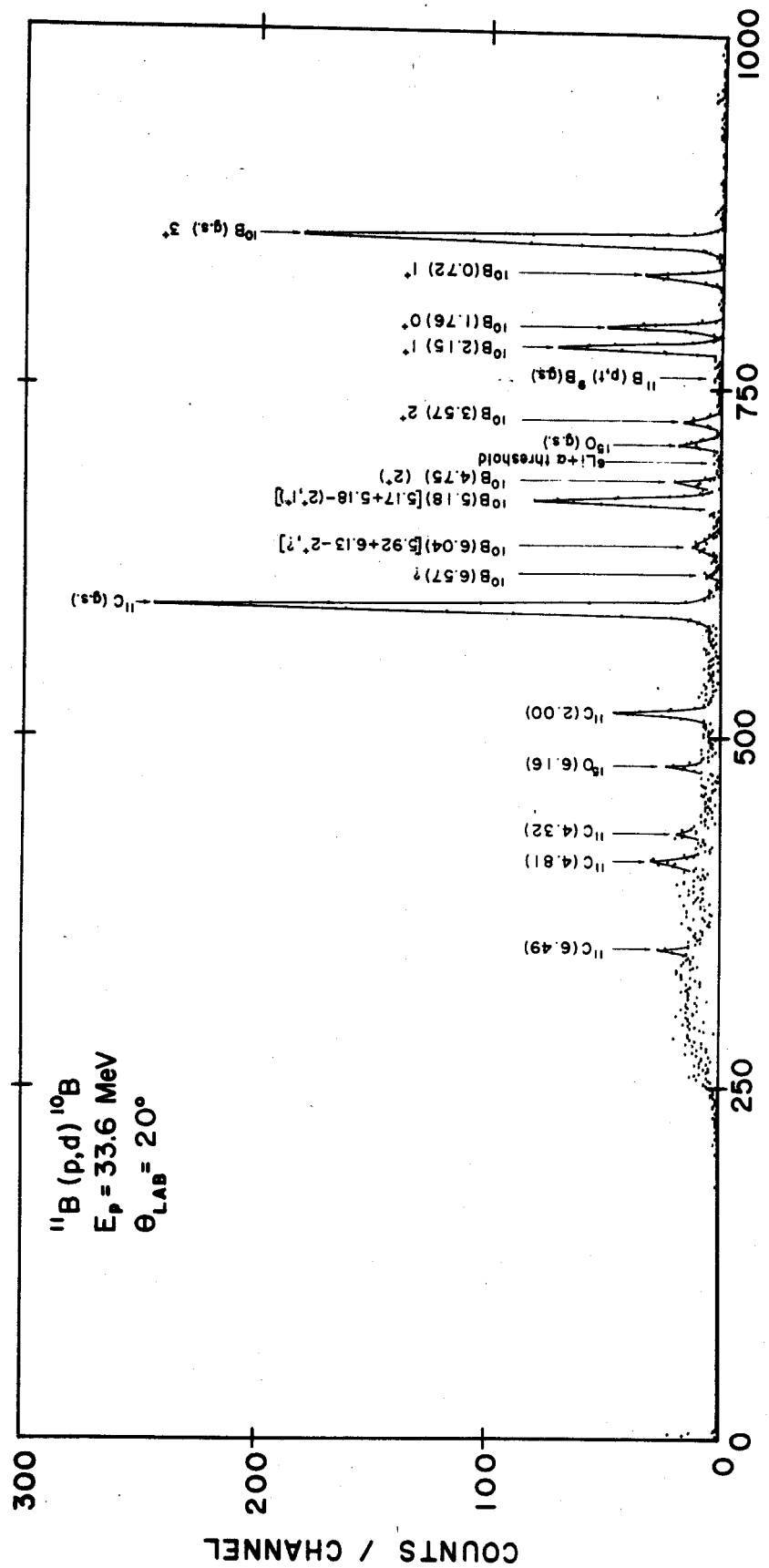

Figure 24.--^{11}B(p,d)^{10}B deuteron spectrum at 20 degrees. The target consisted of 54 µg/cm^2 of ^{11}B evaporated on an ~50 µg/cm^2 carbon backing, resulting in the strong ^{11}C spectrum seen above.

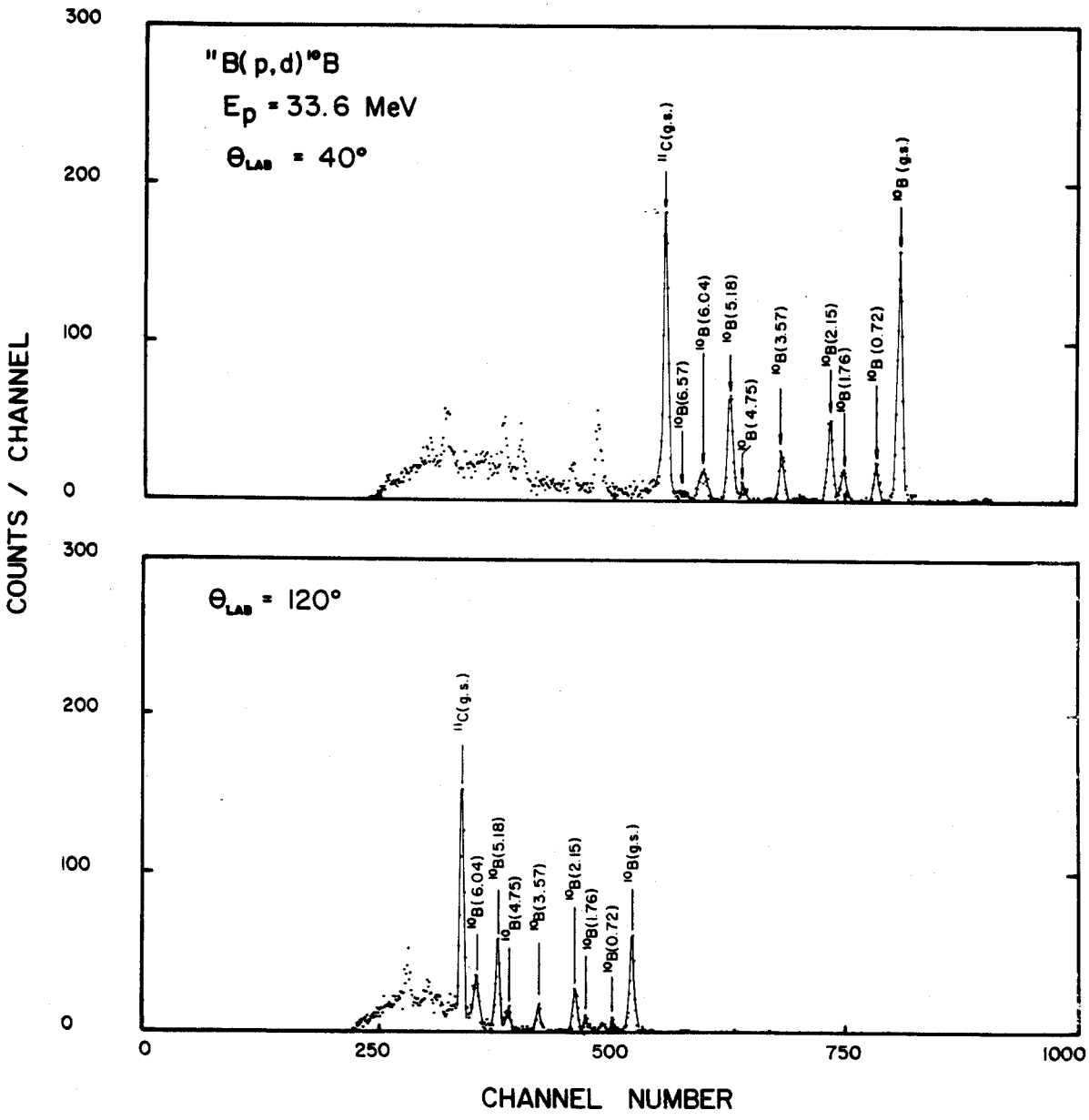

Figure 25.--$^{11}B(p,d)^{10}B$ deuteron spectra at 40° and 120°.

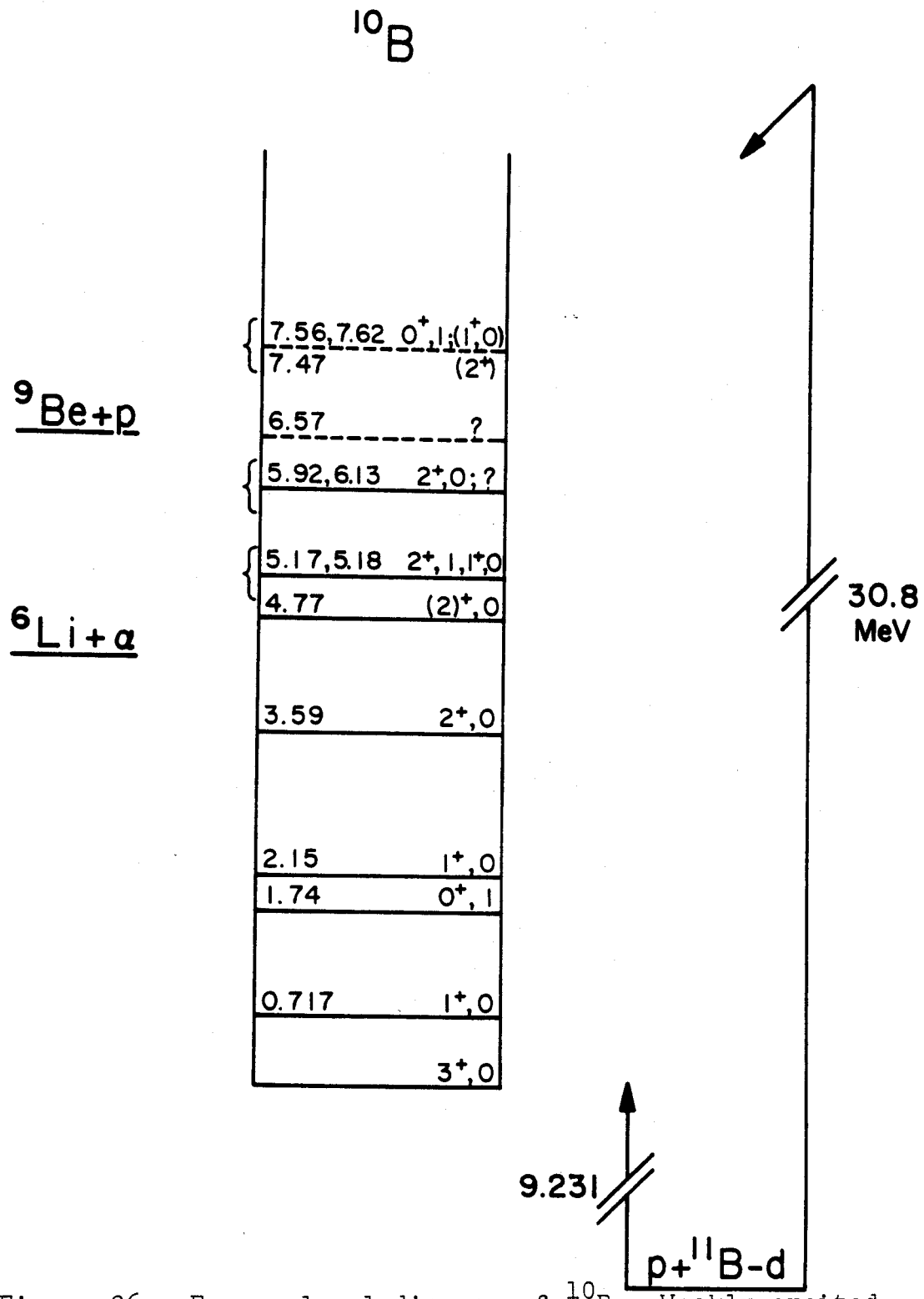

Figure 26.--Energy level diagram of ^{10}B. Weakly excited levels are drawn in with dashed lines; strongly excited levels are drawn in with solid lines. Brackets indicate groups of levels which could not be resolved experimentally.

correspond to known levels of ^{10}B [10] at 5.16 MeV ($J^\pi = 2+$) 5.18 MeV ($J^\pi = 1^+$) and 5.11 MeV ($J^\pi = 2^-$) excitation. The 5.11 MeV level should only be weakly excited, since it can only be excited in the direct reaction process by pickup of a 2s-1d shell neutron. The 5.16 and 5.18 MeV levels can both be excited by a direct reaction mechanism and deuteron groups from the two could not be separated with the 160 keV energy resolution obtained in this experiment.

The deuteron group corresponding to 6.04 MeV excitation energy in ^{10}B could correspond to previously observed levels at 5.92 MeV ($J^\pi = 2^+$), 6.04 MeV ($J^\pi = 4^+$), and 6.13 MeV ($J^\pi = ?$) excitation [10]. The level at 6.04 MeV cannot be excited by a direct reaction process due to angular momentum selection rules, hence principal contributions to this group are from the 5.92 MeV and 6.13 MeV levels.

No evidence was found for the excitation of negative parity states at 7.0 MeV ($J^\pi = 1^-$), 7.8 MeV ($J^\pi = 1^-$), and 8.1 MeV ($J^\pi = 2^-$) excitation [10] which might denote configuration admixtures from the 2s-1d shell in the ground state wave function of ^{11}B. However, as mentioned previously, deuterons corresponding to the 5.11 MeV state ($J^\pi = 2^-$) of ^{10}B could not be resolved from strongly excited positive parity levels, nor could two negative parity states in the 7.5 MeV region of excitation. One can therefore state that there is no direct evidence for sizable 2s-1d admixtures in the ground state wave function of ^{11}B.

The angular distributions for the ^{10}B levels at 0.0, 0.72, 1.76, 2.15, 3.57, and 4.75 MeV excitation have shapes characteristic of the direct pickup of a l_p neutron (see Figs. 27 and 28). The deuteron groups corresponding to ^{10}B excitation energies of 5.18 MeV and 6.04 MeV have similarly shaped angular distributions. This indicates that contributions to the 5.18 MeV group from the 5.11 MeV level ($J^\pi = 2^-$) are indeed small as previously conjectured, and that if the 6.04 MeV group contains contributions from the 6.13 MeV level (J^π unknown), the parity of this level is positive.

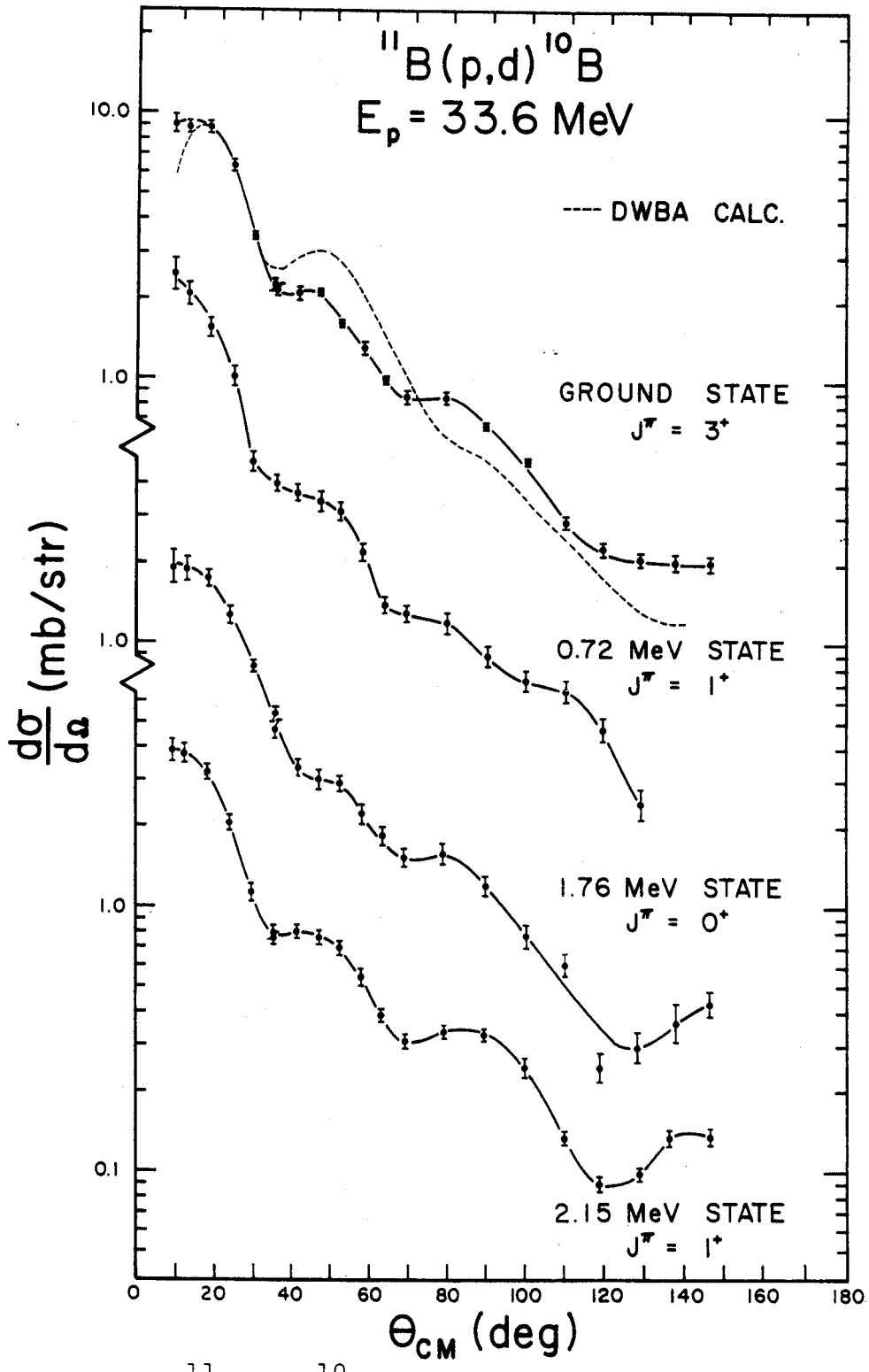

Figure 27.--$^{11}B(p,d)^{10}B$ angular distributions for the 0.0, 0.72, 1.76, and 2.15 MeV states of ^{10}B. The DWBA fit to the ground state differential cross section is shown with a dashed line.

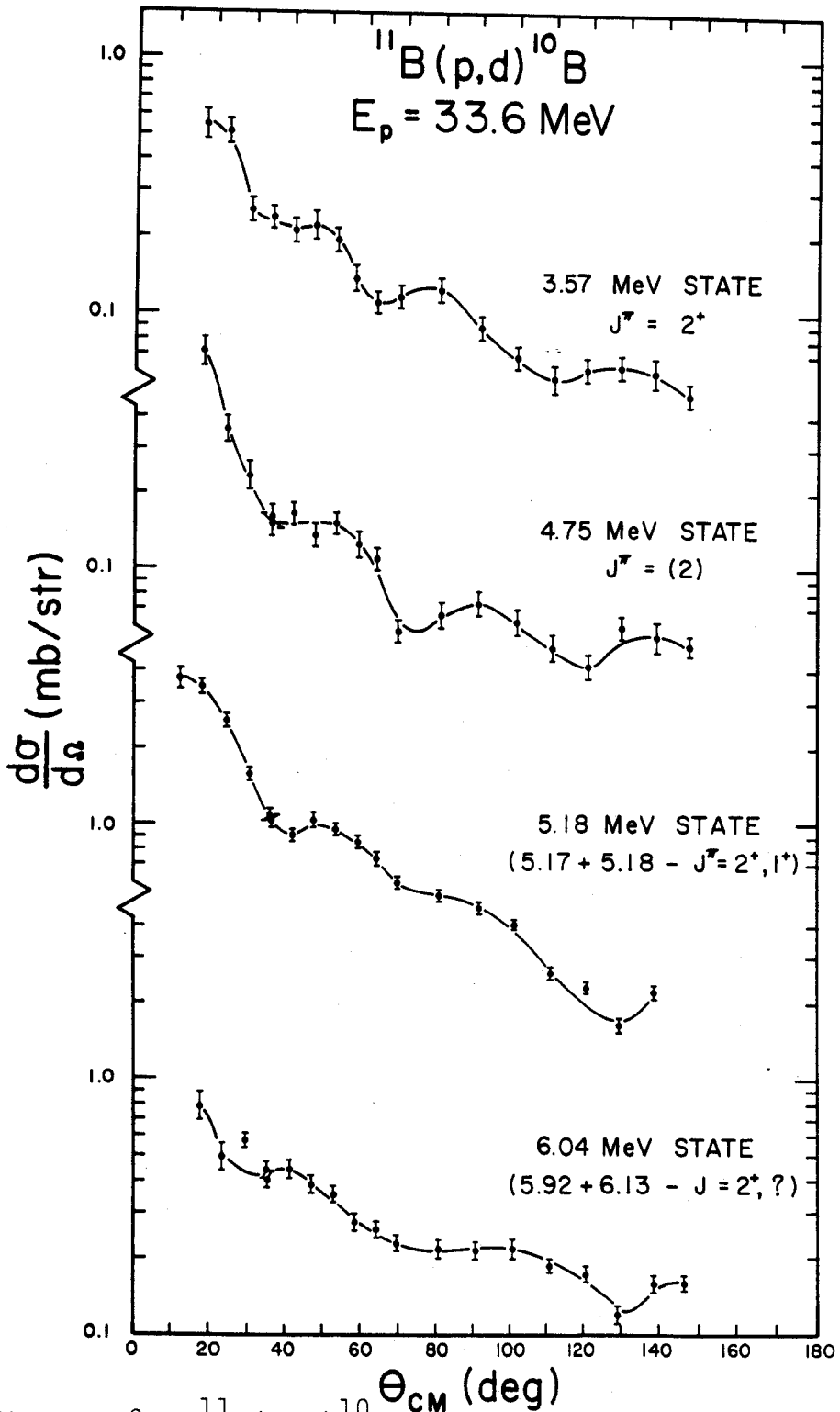

Figure 28.--$^{11}B(p,d)^{10}B$ angular distributions for the 3.57, 4.75, 5.17 + 5.18, and 5.92 + 6.13 states of ^{10}B.

CHAPTER 5

DWBA ANALYSIS

5.A. Elastic Scattering Measurements

Angular distributions for the elastic scattering of protons from targets of ^{6}Li, ^{7}Li, ^{9}Be, and ^{10}B were measured from 12° to 130° in the lab (see Figs. 29, 30, 31, 32). The experimental set up was similar to that described for the (p,d) reaction measurements, except that the counter telescope was replaced by a cylindrically shaped cesium iodide crystal, 0.5 inches long and 0.25 inches in diameter, mounted on a photomultiplier tube. A copper collimator with a thickness equivalent to the range of ∿50 MeV protons with a .125 inch diameter opening was placed in front of the crystal. The size of the crystal was kept as small as possible to minimize background contributions from neutrons and gamma rays. Pulses from the photomultiplier tube were amplified by a Landis preamp and then routed to an ORTEC amplifier for shaping and further amplification; the output was displayed on a 256 channel analyzer. The overall proton energy resolution obtained for these measurements was ∿500 keV.

In the case of $^{7}Li(p,p)$, the proton groups corresponding to the ground state and 0.48 MeV excited state of ^{7}Li

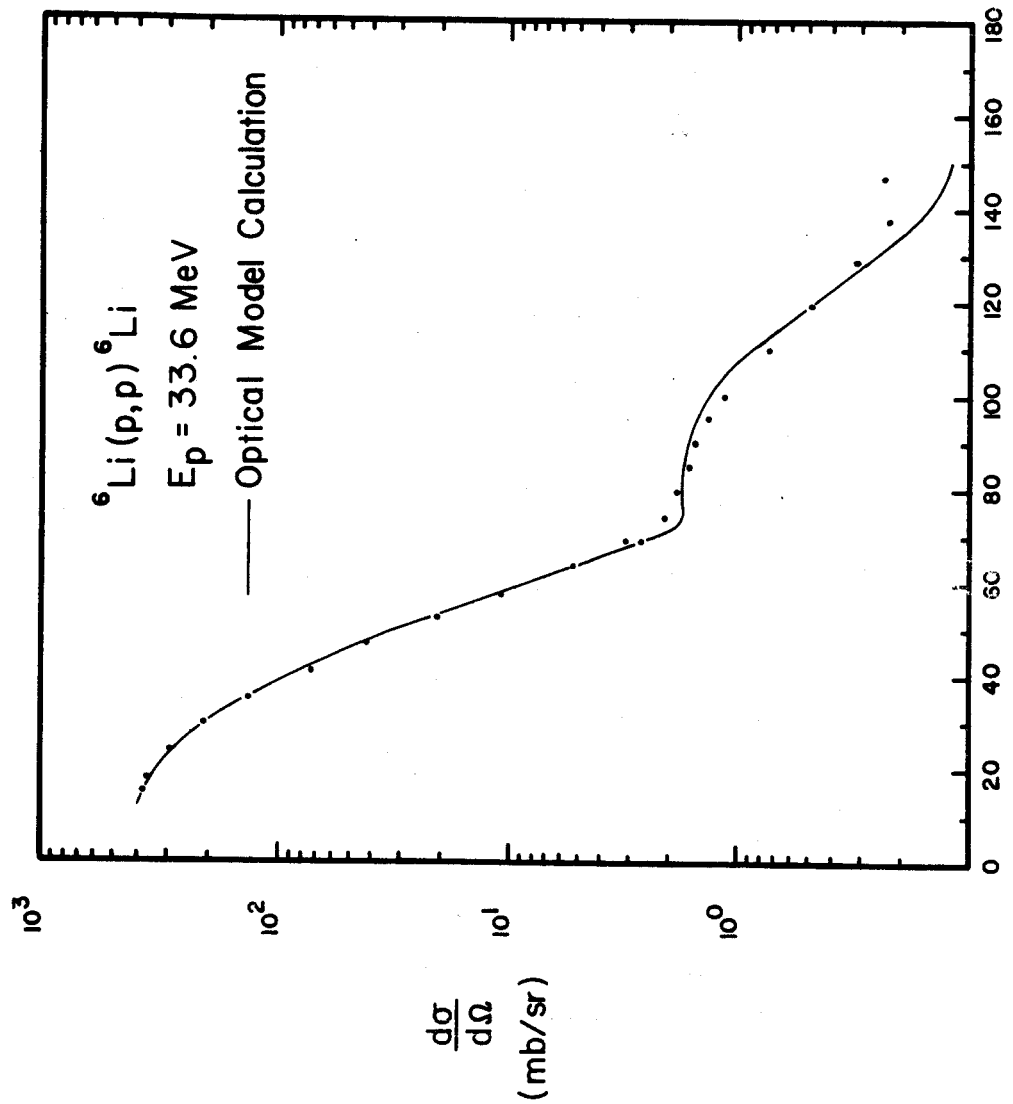

Figure 29.--^{6}Li(p,p)^{6}Li angular distribution. The optical model fit to the data is shown with a solid line.

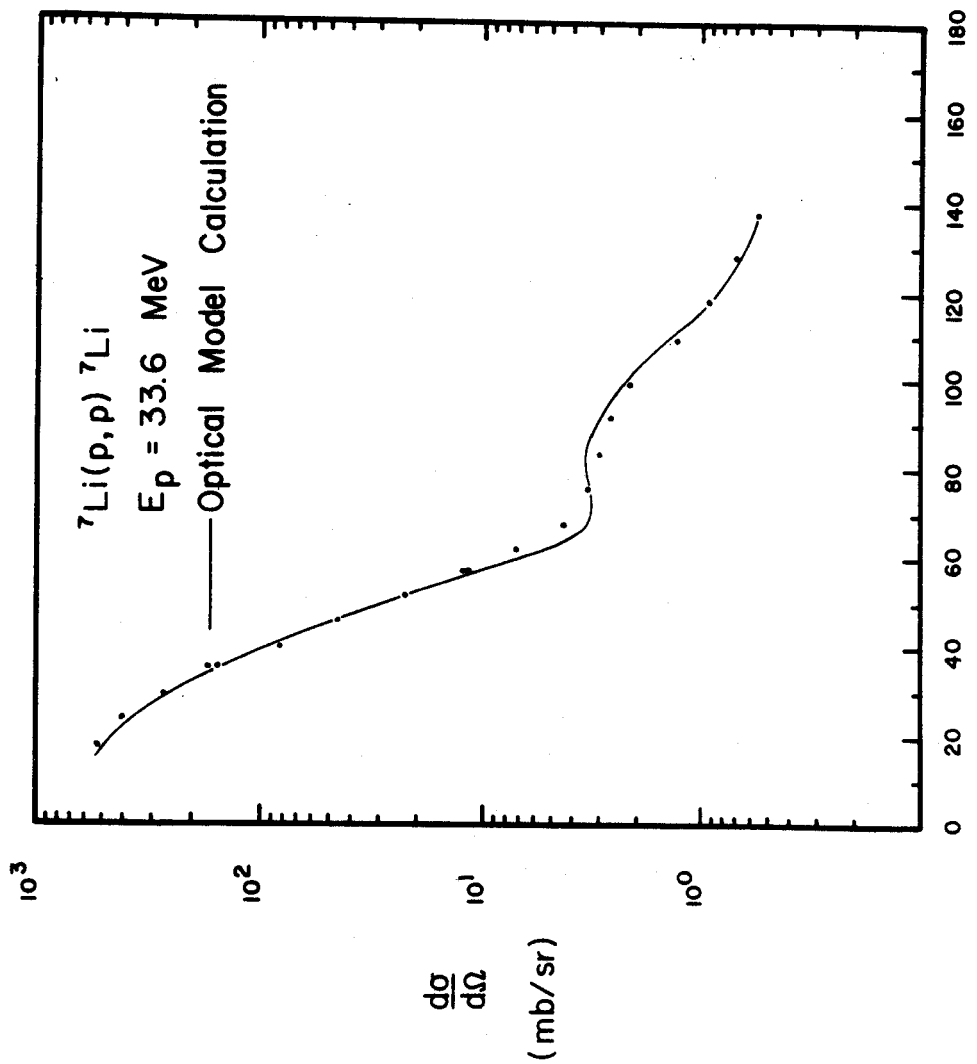

Figure 30.—^{7}Li(p,p)^{7}Li angular distribution. The optical model fit to the data is shown with a solid line.

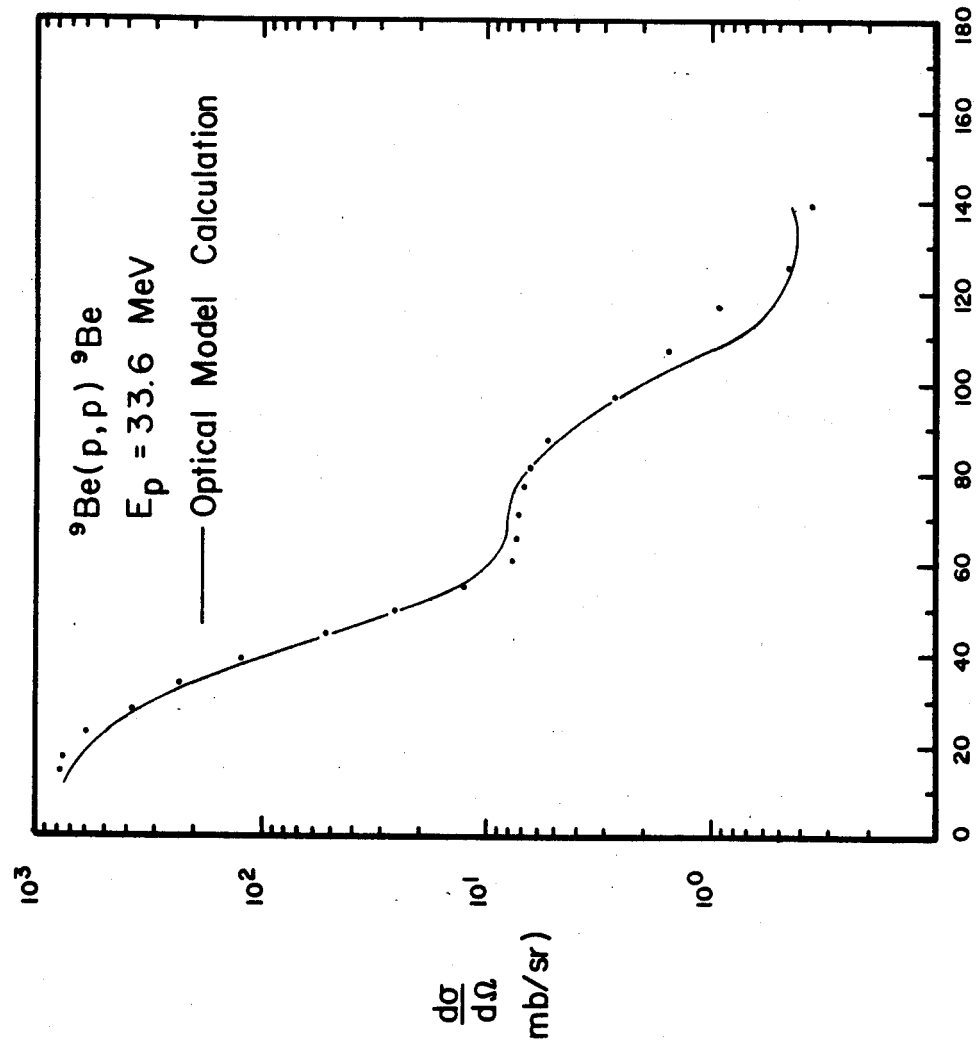

Figure 31.—^{9}Be(p,p)^{9}Be angular distribution. The optical model fit to the data is shown with a solid line.

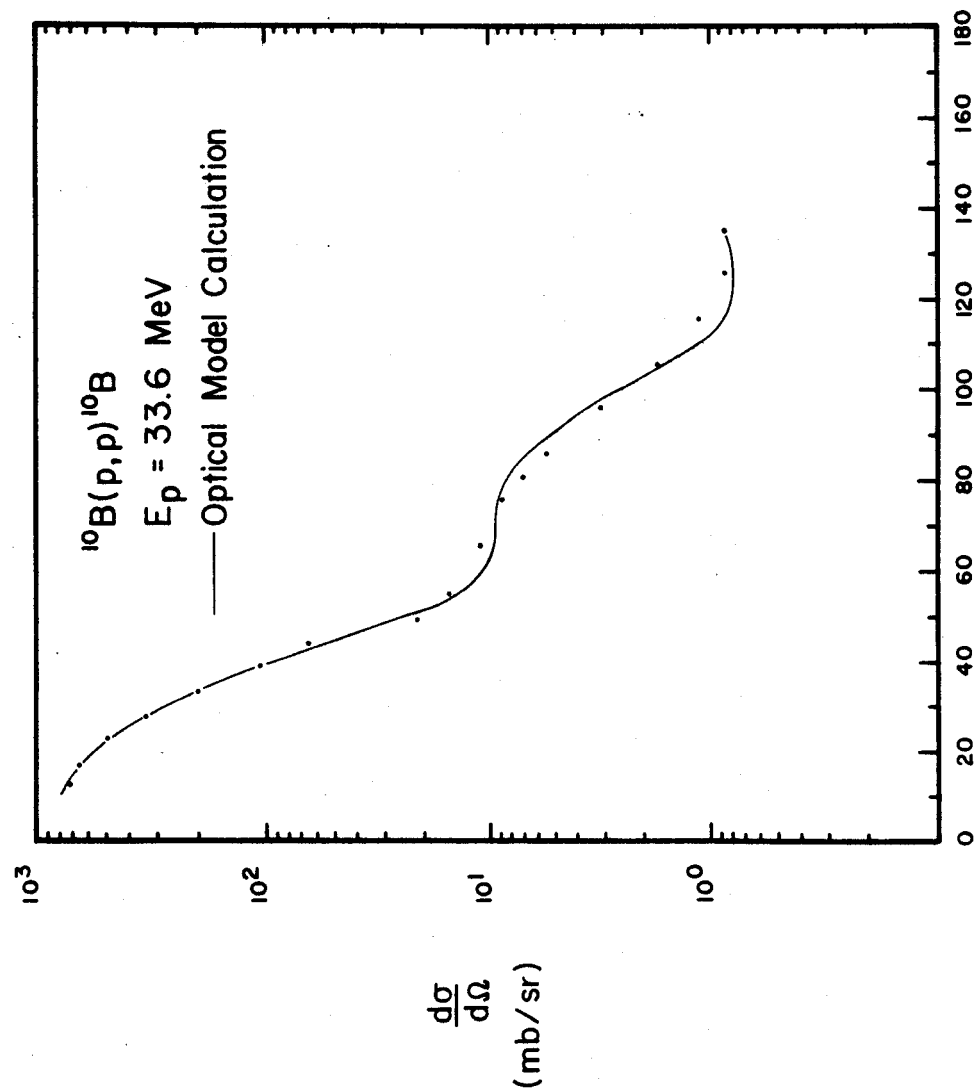

Figure 32.--$^{10}B(p,p)^{10}B$ angular distribution. The optical model fit to the data is shown with a solid line.

could not be resolved. Angular distributions had been measured for both states at an incident proton energy (E_p) of 25 MeV [60] and the same relative yields were assumed in computing the differential cross section for the ground state of ^{7}Li at an incident proton energy of 34 MeV. This amounted to an average correction of 2% at forward angles and between 15% and 25% at backward angles.

Similarly, proton groups from the ground state and 0.72 MeV excited state of ^{10}B could not be resolved. Data taken from the same reaction at incident proton energies of 19 MeV [61] and 185 MeV [62] show the cross section of the 0.72 MeV state to be approximately 1% to 2% as large as that of the ground state, so that this small correction to the ground state cross section was ignored. The contribution to the differential cross section from an ~8% ^{11}B impurity in the target was also not considered. This is not a serious omission, assuming that the ^{10}B and ^{11}B angular distributions do not differ appreciably in shape and magnitude. This is a rather good assumption in the case of the ^{6}Li-^{7}Li pair where the magnitudes differ by ~33% and the shapes are very similar. The accuracy of the absolute differential cross sections is 6% to 9%.

5.B. Optical Model Calculations

The Abacus computer code [29] calculates the angular distribution for particles scattered from an optical potential of the form

$$(1)\quad U = U_c - V f(r,R,a_R) - i 4a_I \frac{d}{dr} f(r,R,a_I) - \frac{1}{(M_\pi c)^2}\frac{V_{so}}{r}\frac{d}{dr} f(r,R,a_R)$$

Here $$f(r,R,a) = \frac{1}{e^x+1} \quad ; \quad x = \frac{r - RA^{1/3}}{a}$$

and U_c is the Coulomb potential from a uniformly charged sphere of radius $RA^{1/3}$ fermis. The code can be used to obtain agreement between the calculation and the experimental angular distribution; the method used employs a least squares criterion and allows any number of chosen parameters to be varied to arrive at a best fit to the data. The "best" fit is decided upon on the basis of a chi-squared calculation in the program itself and visual inspection of the overall fit to the experimental data. The optical model calculation representing the best fits for the elastic scattering of protons from ^{6}Li, ^{7}Li, ^{9}Be, and ^{10}B are shown in Figures 29, 30, 31, and 32. The parameters used to obtain these fits are given in Table 7.

The deuteron optical parameters were obtained in a similar manner by fitting data from the elastic scattering of deuterons from ^{9}Be at an incident deuteron energy (E_d) of 27.7 MeV [63] and from ^{7}Li at E_d = 28 MeV [64]. The best fit optical parameters obtained are given in Table 8; no spin orbit term was included in the optical potential and the imaginary diffuseness (a_I) was set equal to the real diffuseness (a_R). Deuteron optical parameters for the

boron calculations were obtained from the literature [65] and are given below.* In this case, a volume absorption term is used in the imaginary portion of the potential.

TABLE 7.--Proton optical model parameters.

Target	V(MeV)	W(MeV)	V_{So}(MeV)	R(f)	a_R(f)	a_I(f)
^{6}Li	44.56	6.92	7.38	1.124	.578	.685
^{7}Li	46.45	6.34	7.18	1.187	.478	.727
^{9}Be	48.92	6.44	6.30	1.139	.613	.616
^{10}B	53.99	6.22	6.31	1.097	.548	.644

TABLE 8.--Deuteron optical model parameters.

Target	V(MeV)	W(MeV)	R(f)	a_R(f)
^{7}Li[a]	79.45	11.23	1.094	.769
^{9}Be	74.03	11.67	1.239	.736

[a]Data renormalized by 0.85.

5.C. DWBA Calculations

Distorted wave Born approximation calculations (see Chapter 1) were carried out using the Masefield computer code on the CDC 3600 computer. The calculation has been

*Deuteron optical parameters for ^{10}B(d,d) E_α = 21.6 MeV V = 83.5 MeV, W = 14.94 MeV, R = 1.33 f, a = 0.65 f.

checked and found to agree exactly with identical calculations performed with the DWBA code, JULIE [66], when no spin orbit term was included in the proton optical potential; there was a slight difference between the shapes of the angular distributions from 0° to 5° and for angles $\geq$ 80° when a spin orbit term was included in the potential. There is no apparent explanation for this difference, however it does not affect the general features of the calculated angular distribution and most important, does not affect the extraction of the spectroscopic factors.

The DWBA analysis was carried out with parameters for the picked up neutron of a_n = 0.65 f and $R_n = 1.25\ A^{1/3}$ f. No spin orbit term was included in the neutron potential.

The DWBA calculations lead to an interesting result, in that it was impossible to get a reasonable fit to the (p,d) angular distribution data using the optical parameters in Tables 7 and 8. However, if the imaginary well of the deuteron optical potential (W_d) is increased by a factor of three in the case of ^{9}Be(p,d)^{8}Be and a factor of four in the cases of the lithium and boron (p,d) reactions, reasonable fits are obtained in all cases (Figs. 10, 13, 17, 22, 27). A 20% variation of any of the other parameters would not produce similar results. The same situation was encountered in applying a DWBA analysis to the data from ^{4}He(p,d)^{3}He with E_p = 31 MeV [67].

This anomalously large value of W_d may be a consequence of using the optical model potential to describe the interaction of the scattered deuteron with a relatively small number of nucleons which comprise the scattering nucleus. It may also be due to the fact that in the optical model, the deuteron is treated as a point particle, whereas the weak coupling within the deuteron itself is likely to be sensitive to deformations caused by interactions with the target nucleus. No similar effect was noted, however, when optical parameters obtained from elastic scattering were used in DWBA calculations of the (p,d) reaction with heavier nuclei [14]. Thus it appears that the first possibility may be the more relevant of the two.

The same effect was encountered by Siemsson [68] in attempting to fit data from (d,p) reactions with lp shell nuclei. The incident deuteron energy was ∿20MeV. Reasonable fits to the data were obtained by using a cutoff radius in the DWBA calculations [33]. It was found, however, that the amplitude of the first peak of the differential cross section varied as a function of the cutoff radius. Roughly, the amplitude of the first peak of the differential cross section had two maxima, the first maximum appeared at a cutoff radius of 0 fermis and the second at a cutoff radius of 3 to 5 fermis. The variation in the cross section peakwas approximately 3 to 1. Cutoff radii corresponding to the second maximum were used in the

subsequent DWBA calculations in which reasonable fits to the data were obtained.

Thus, it appears that a large increase in the strength of the imaginary deuteron well depth and the use of a cut-off radius both have a similar effect on the DWBA calculation. As opposed to using a rather arbitrary cutoff, increasing the deuteron well depth varied the amplitude of the first peak of the differential cross section by less than 15% in all cases except that of $^{10}B(p,d)\ ^{9}B$, where the change was of the order of 20%.

The concern about the behavior of the amplitude of the differential cross section's first peak arises because the spectroscopic factor is assumed to be directly proportional to the ratio of the maxima of the DWBA and experimental distributions' first peaks. If the parameters of the DWBA calculation are varied in order to produce theoretical results which bear a reasonable resemblance (in shape) to the experimental data, the effect of these variations on the amplitude of angular distribution's first peak must be considered in deciding just how meaningful the extracted spectroscopic factors are.

In summary, neither method of obtaining reasonable fits to the data explains the reason for the anomalous behavior of the DWBA in the case of light nuclei. The effect is large and reproducible, and it has been observed in the case of (d,p) and (p,d) reactions at several

different bombarding energies. It deserves further study in that it points out weaknesses in the DWBA calculations which are especially emphasized in the case of light nuclei.

CHAPTER 6

SPECTROSCOPIC FACTORS

6.A. Experimental Spectroscopic Factors

The experimental spectroscopic factor $S_{A\rightarrow B}$ for the transition A(p,d)B, which proceeds by a direct pickup of $l_{p3/2}$ and $l_{p1/2}$ neutrons, was calculated from the expression

$$S_{A\rightarrow B} = \frac{\sigma_{EXP}}{1.6\sigma^{M}_{DWBA}}$$

σ^{M} is the magnitude of the differential cross section at the angle for which it has its characteristic $\ell_n = 1$ maximum. The DWBA result, which uses the zero range approximation, is multiplied by a factor of 1.6 to make it approximately equivalent to a calculation using the effective range theory [69, 70].

This method of extracting the spectroscopic factor is based on the assumption that the experimental angular distribution and the DWBA have the same shape and differ in magnitude by a constant factor, i.e., the spectroscopic factor. Thus, the magnitudes of the integrated or total DWBA and experimental cross sections also differ by the same spectroscopic factor. In practice, the DWBA calculation does have a shape similar to that of the experimental

distribution, with the difference between the two shapes appreciable for angles $\geq 90°$. The disagreement between theory and experiment at backward angles results in part from physical effects not included in the DWBA formalism.

The difference between the integrated cross sections is essentially determined by the values of the angular distributions at forward angles because of the characteristic forward peaking of the direct reaction angular distributions, and is not significantly affected by their detailed behavior at backward angles. For example, in the case of $^{7}Li(p,d)^{6}Li$ the contribution to the integrated cross section from 90° to 180° is $\sim$4%. Assuming that the shapes of the DWBA and experimental distribution match quite well at forward angles, determining the spectroscopic factor from the relative peak heights of the characteristic $\ell = 1$ maxima is equivalent to determining the spectroscopic factor from the relative magnitude of the integrated cross sections. Spectroscopic factors can be extracted using this method in cases where the integrated cross section cannot be obtained directly because of experimental difficulties encountered in measuring the angular distribution at backward angles.

6.B. Theoretical Spectroscopic Factors

The theoretical spectroscopic factors were obtained for the transition A(p,d)B from the coefficients of fractional parentage, $\beta_{\ell j}$, calculated by Kurath using the intermediate

coupling model for 1_p shell nuclei [16]. The theoretical spectroscopic factor $S_{A\to B}$ is given by

$$S_{A\to B}(\ell_n=1\ j_n=3/2,1/2) = n(T'1/2\ M_T'\ 1/2\,|\,T\ M_T)^2 \sum_{\substack{\ell\\ j}} \beta_{\ell j}{}^2$$

$$j = 1/2,3/2$$
$$\ell = 1$$

n is the number of nucleons in the 1p shell of A and ($|$) is a Clebsch Gordon coefficient with T', M_T' and T,M_T the isotopic spin and its projection for the final state and initial state respectively. As calculated above, the spectroscopic factors relate to states with pure isospin. Other sets of spectroscopic factors for the reactions $^7Li(p,d)^6Li$ and $^{11}B(p,d)^{10}B$, $^{10}B(p,d)^9B$ were obtained from the shell model calculation of Barker [17] and the intermediate coupling calculations of Balashov [18], respectively.

Theoretical and experimental relative spectroscopic factors were obtained by normalizing the sum of the spectroscopic factors for each reaction to one. Considering the difficulty in extracting meaningful absolute spectroscopic factors from the DWBA comparison to the data, the relative spectroscopic factor was calculated to provide a better look at the relative amount of overlap between the target nucleus' ground state wave function and wave functions of the residual nucleus' different excited states plus a 1p shell neutron.

6.C. Comparison of Results

The agreement between theory and experiment for $^{7}Li(p,d)^{6}Li$ is good (see Fig. 33). The experimental spectroscopic factors of zero for the 4.57 and 6.0 MeV states could be due to the difficulty in extracting the small deuteron yields, corresponding to these broad states, from the background.

Figure 34a shows the large discrepancy between theory and experimental spectroscopic factors for the ^{8}Be $J^{\pi} = 2^{+}$ doublet at 16.6 and 16.9 MeV and also for the $J^{\pi} = 3^{+}$ doublet at 19.1 and 19.2 MeV. This disagreement could result from the fact that the experimental spectroscopic factors have been extracted using a DWBA calculation with deuteron potential parameters obtained from the elastic scattering of deuterons from the ground state of ^{9}Be, whereas the nucleus is actually left in a state 17 to 19 MeV in excitation above the ground state of ^{8}Be. The effect of this approximation on the extraction of the spectroscopic factor is not known, but it should be noted that the same large discrepancies are not present in the results for the $J^{\pi} = 1^{+}$ doublet at 18 MeV excitation. The last observation fits in with another possible explanation for the observed disagreement. The theoretical calculations assume the states to be pure in isotopic spin, whereas previous experiments have shown considerable isospin mixing to be present within the $J^{\pi} = 2^{+}$ and 3^{+} doublets. If two states of pure isospin are mixed to produce two new final states of

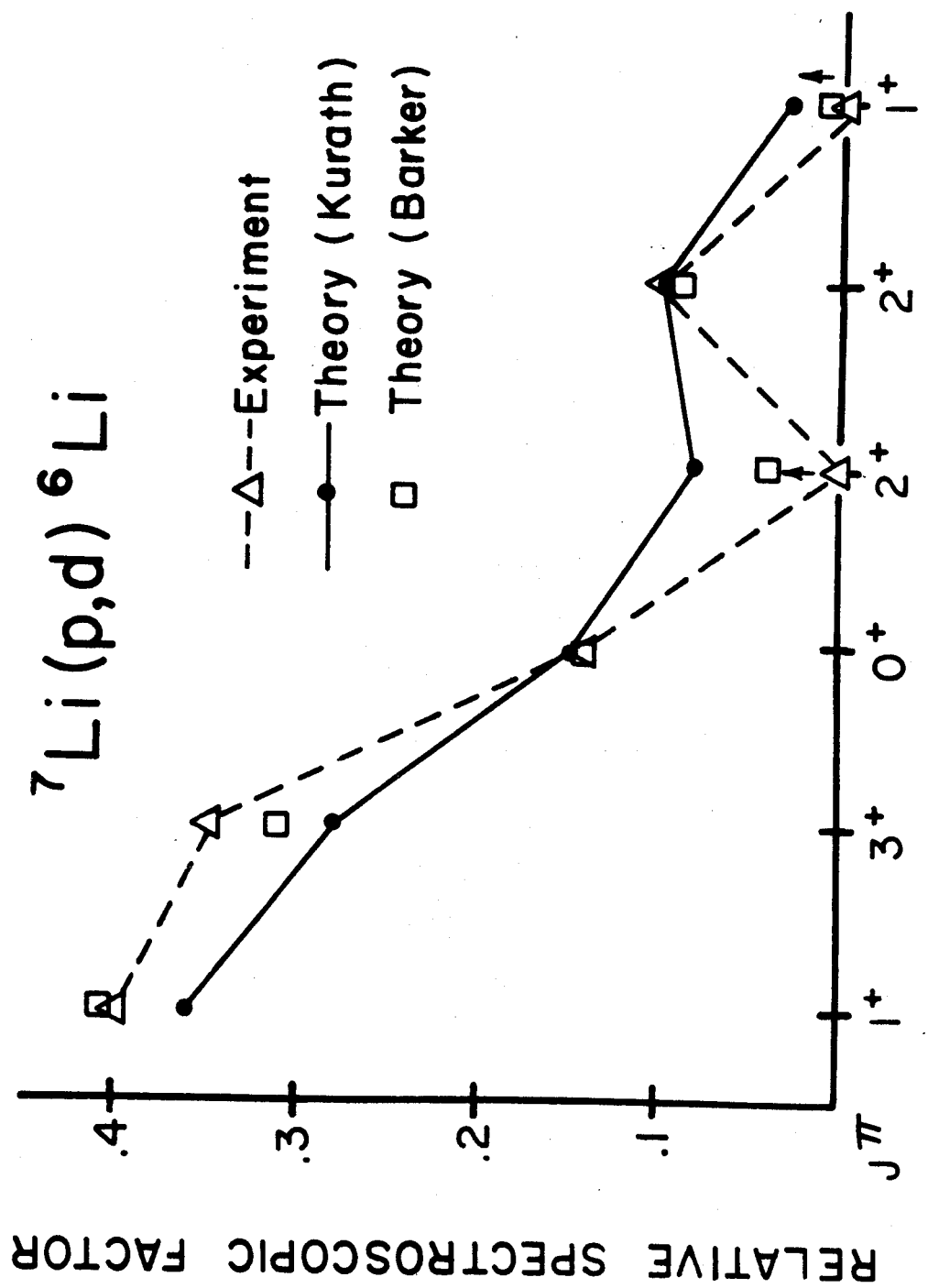

Figure 33.--Comparison of theoretical and experimental relative spectroscopic factors for ^{7}Li(p,d)^{6}Li. The arrows above the levels at 4.57 MeV and 6.0 MeV excitation energy are used to indicate that small deuteron yields from these levels may not have been observed because of the width of these states and a high background.

Fig. 34a

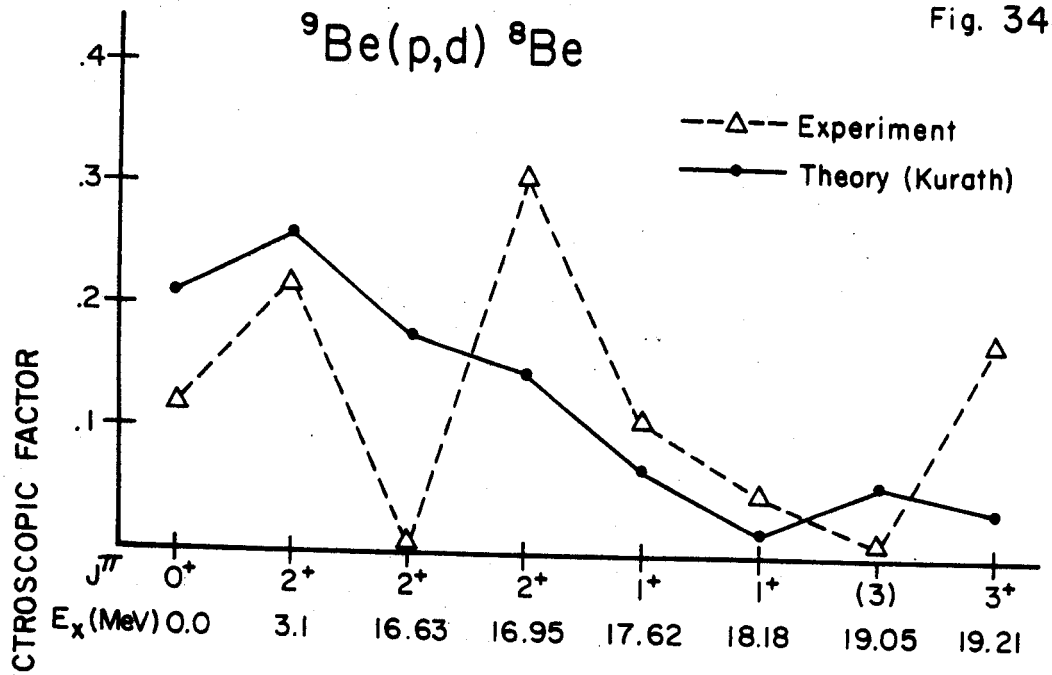

Fig. 34b

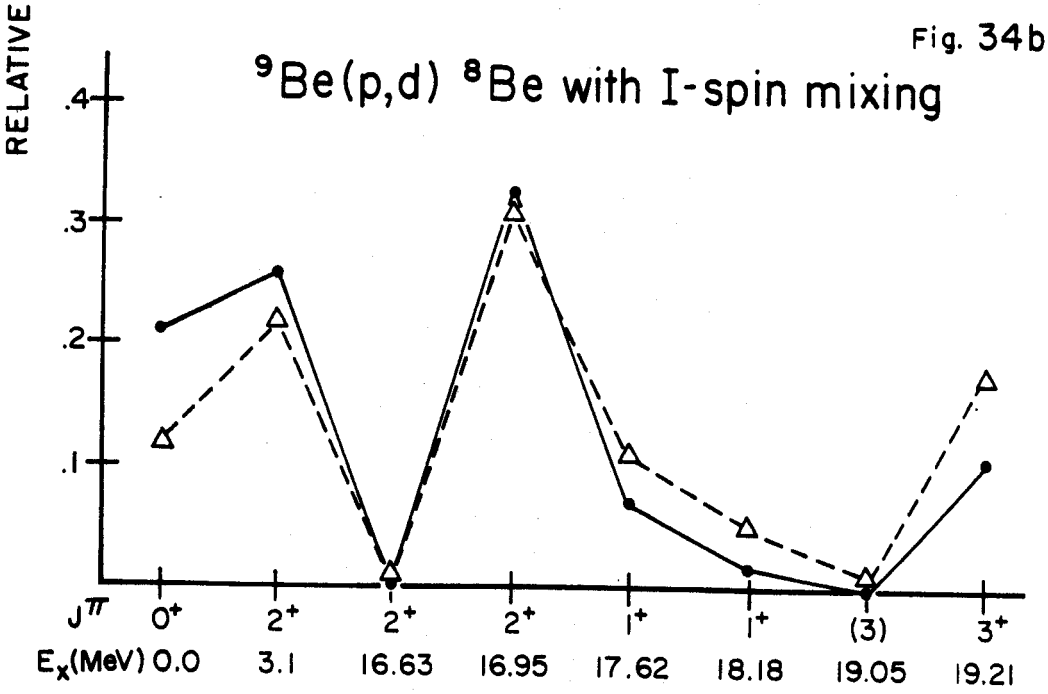

Figure 34.--Comparison of theoretical and experimental relative spectroscopic factors for ^{9}Be(p,d)^{8}Be. Good agreement is obtained except for the $J^\pi = 2^+$ and 3^+ doublets. If the sum of the theoretical spectroscopic factors within these doublets in 34a is fixed, but the ratio of strengths is adjusted to best fit the experimental data, the Figure 34b is obtained. This is equivalent to mixing states with definite isospin within the

indefinite isospin, the ratio of spectroscopic factors for the isospin mixed pair will be different, in general, from that originally found for the pair with pure isospin. However, the sum of the spectroscopic factors for each pair is the same for both cases. Assuming, therefore, that the experimental results only represent a mixing of the theoretical isospin pure states, there should be agreement between theoretical and experimental sums of spectroscopic factors for each doublet. The sum of the experimental spectroscopic factors for the $J^{\pi} = 2^{+}$ and 3^{+} doublets is .32 and .19, respectively, whereas the sum of the theoretical spectroscopic factors for the same $J^{\pi} = 2^{+}$ and 3^{+} doublets is .33 and .11, respectively. This same approach was also used in obtaining Figure 34b. Here the ratio of spectroscopic factors within the $J^{\pi} = 2^{+}$ and 3^{+} doublets has been adjusted to give better agreement with experiment, while the sum of spectroscopic factors within the doublets is the same as that in Figure 34a. Thus, good agreement with theory for the $^{9}Be(p,d)^{8}Be$ experiment can be obtained, assuming that the isospin mixing with the $J^{\pi} = 2^{+}$ and 3^{+} doublets is the cause of the major differences observed.

Relatively good agreement is obtained between the theoretical calculations of Kurath and experimentally obtained spectroscopic factors for the $^{11}B(p,d)^{10}B$ reaction (see Fig. 35). Somewhat poorer agreement is obtained with the calculations of Balaskov; in particular, there is a marked difference between the calculated and experimental

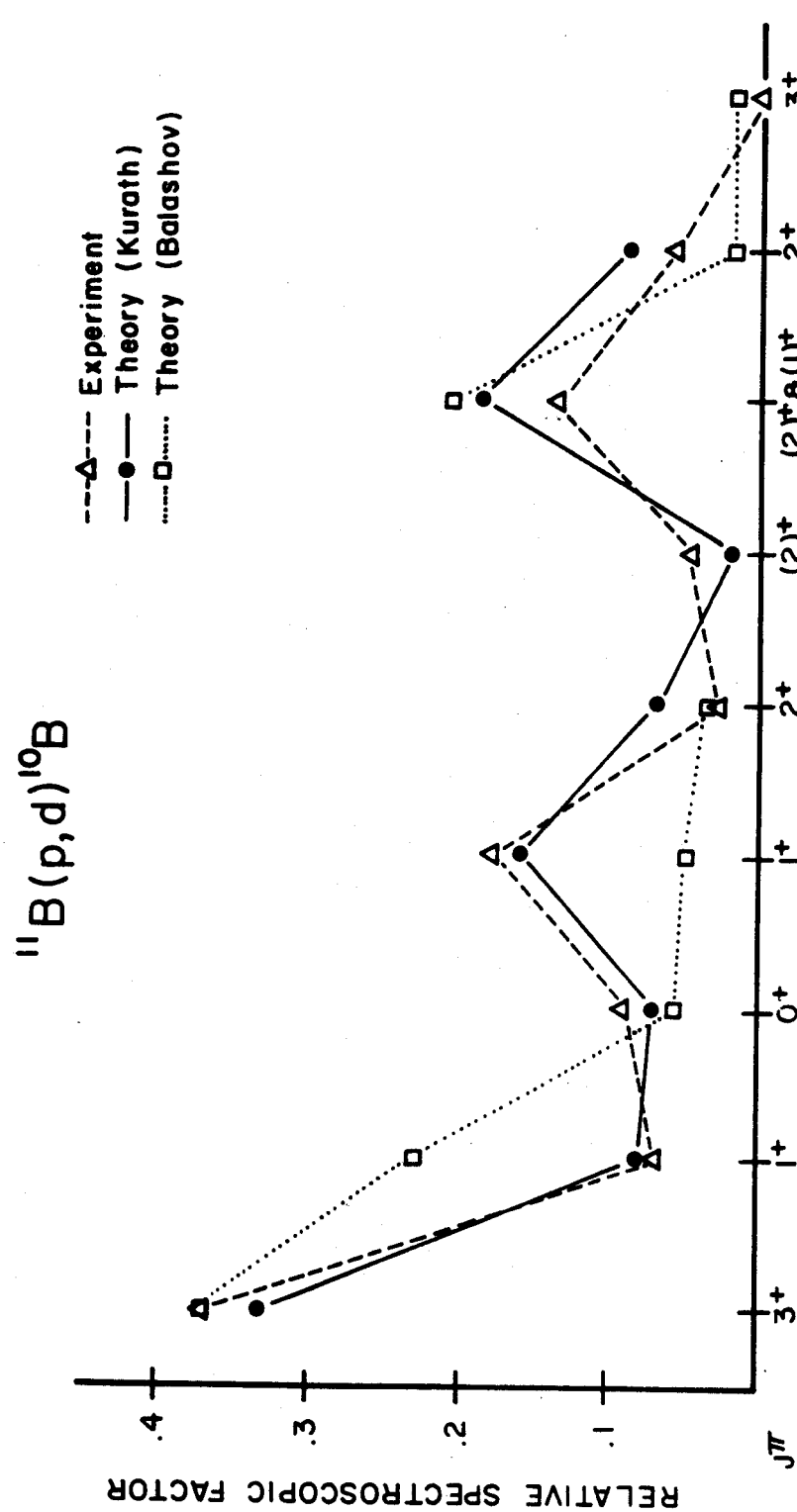

Figure 35.--Comparison of theoretical and experimental spectroscopic factors for $^{11}B(p,d)^{10}B$. No deuterons were observed corresponding to a $J^{\pi} = 3^+$ state at a theoretical ^{10}B excitation energy of 6.1 MeV [18], however the level is predicted to be weakly excited.

spectroscopic factors for the 0.72 MeV and 2.15 MeV levels of ^{10}B. Balaskov's calculations also do not include a spectroscopic factor for the $J^{\pi} = 2^{+}$ level at 4.75 MeV.

Both Balaskov and Kurath predict a weakly excited level ($J^{\pi} = 3^{+}$) around 5-6 MeV excitation in ^{10}B. There are three known levels in the region 6.5 - 7.0 MeV excitation in ^{10}B with unknown spins and parities [10]. None were observed to be excited by the (p,d) reaction, however, the deuteron yield may have been very small and lost in the background.

The spectroscopic factor for the deuteron group observed at a ^{10}B excitation energy of 6.04 MeV was calculated assuming only a $J^{\pi} = 2^{+}$ state contributed to the deuteron yield, when, as mentioned previously, the energy resolution could not have separated contributions from previously observed levels of ^{10}B at 5.92 MeV ($J^{\pi} = 2^{+}$) and at 6.13 MeV ($J^{\pi} = ?$) [10]. A comparison of the experimental result with the calculation of Kurath indicates that the ^{10}B 5.92 MeV level is the main contributor to the observed deuteron group.

Spectroscopic factors have now been extracted for the $^{11}B(p,d)^{10}B$ reaction at incident proton energies of 18.9 MeV [7], 155 MeV [57], and 33.6 MeV; they have also been extracted for the $^{11}B(d,t)^{10}B$ reaction at an incident deuteron energy of 21.6 MeV [65]. The results are shown in Figure 36, where the spectroscopic factors for the ground state transition have been normalized to one. The

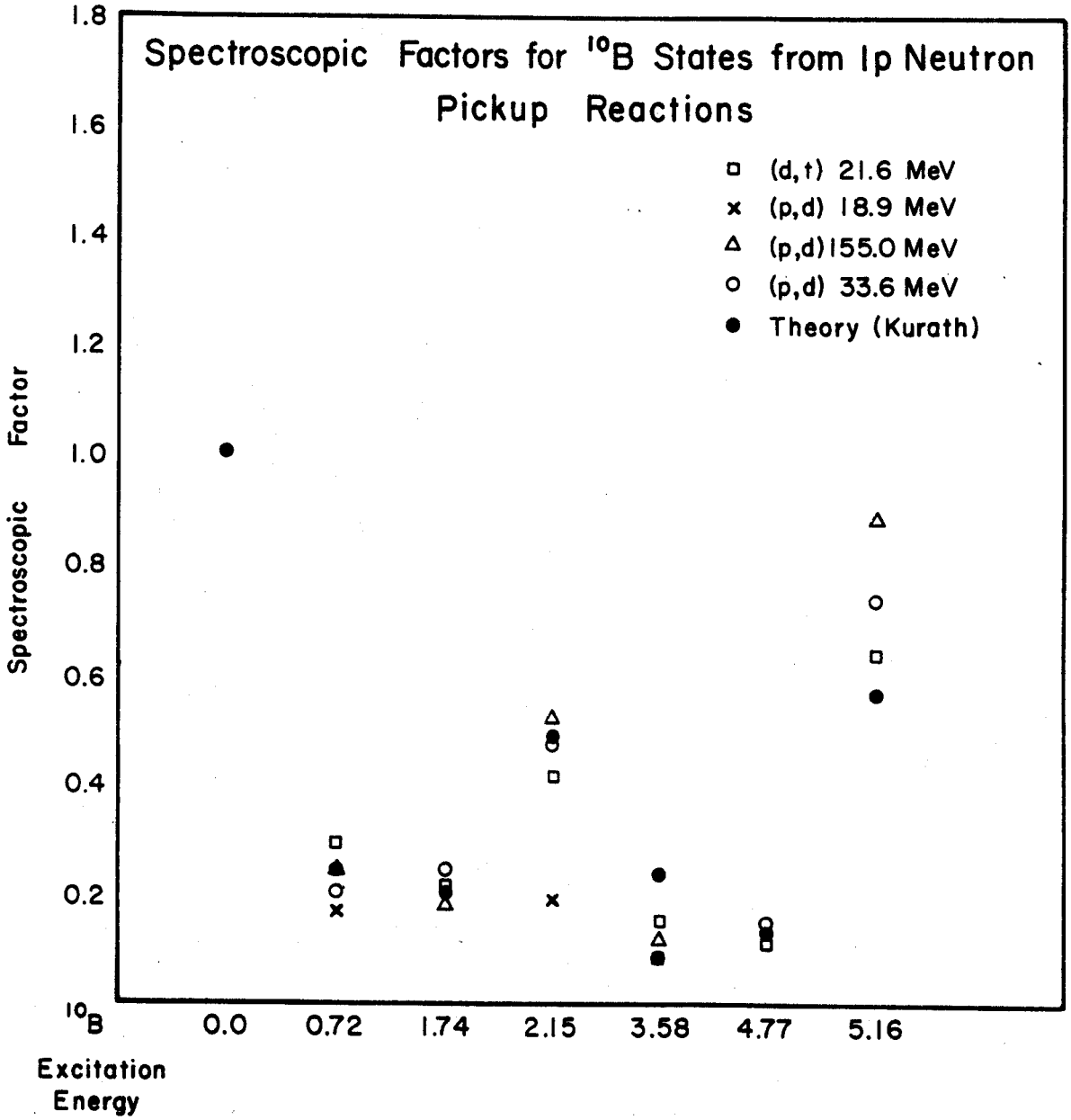

Figure 36.--A comparison of experimentally obtained spectroscopic factors for ^{10}B states.

experimental spectroscopic factors for the deuteron group corresponding to a ^{10}B excitation energy of 5.16 MeV have been extracted assuming that only the 5.16 MeV level of ^{10}B ($J^{\pi} = 2^{+}$) contributes to the yield. In all cases, however, the energy resolution was not good enough to separate out contributions to the observed deuteron yield from the 5.18 MeV level of ^{10}B ($J^{\pi} = 1^{+}$). Contributions to the observed deuteron group from both levels were assumed in the calculation shown in Figure 35. The experimental spectroscopic factor for the 5.16 MeV level of ^{10}B extracted from the E_p = 155 MeV work also contains contributions from the 4.77 MeV level of ^{10}B ($J^{\pi} = 2^{+}$); the two levels could not be resolved with this high incident proton energy.

The spectroscopic factor for the 2.15 MeV level of ^{10}B obtained from the work at E_p = 18.9 MeV appears likely to be in error, as its value is significantly different from a closely grouped series of results from (p,d) experiments performed over a wide range of energies, Kurath's theoretical calculations, and a (d,t) experiment (see Fig. 30). It was on the basis of the work done at E_p = 18.9 MeV that a previous investigation proposed an isotopic spin dependence in the (p,d) and (d,t) reactions which would account for significant differences in the observed spectroscopic factors for the ^{10}B 2.15 MeV level [65]; the present work does not support these contentions.

With the above data point ignored, a mean spectroscopic factor was calculated from the experimental data for each ^{10}B level; the results are shown in Table 9.

TABLE 9.--Average differences of spectroscopic factors from mean values of the experimental data.

Spectroscopic Factors from:	Average Difference from Mean Values
(p,d) reactions	15%
(d,t) reactions	18%
theoretical calculation (Kurath)	20%

From these results, the following general conclusions appear to be valid:

1. Spectroscopic factors obtained over a wide range of incident energies agree to within 15% - 20%.
2. Spectroscopic factors obtained from the (d,t) reaction are not significantly different from those obtained with (p,d) reactions.
3. Kurath's calculations agree with the experimental spectroscopic factors to within $\sim$ 20%.
4. A reasonable absolute error for the spectroscopic factors obtained in this work falls somewhere in the region of 15% - 20%.

Experimental and theoretical spectroscopic factors for the reaction $^{10}B(p,d)^{9}B$ are shown in Figure 37. The ^{9}B levels at 4.4 MeV and 5.7 MeV have been predicted theoretically by both Kurath and Balaskov, but have not been observed experimentally. The predicted yeilds are small, however, and the peaks may have been lost in the high background.

The ^{9}B levels at 0.0, 2.35, 7.1, and 11.75 MeV all have been determined to have negative parity (see Chapter 4), while the ^{9}B level at 14.01 MeV has been tentatively identified as having negative parity. Assuming the experimental spectroscopic factors agree with theoretical calculations to within ∿20%, the spins for the observed levels were assigned by comparing the theoretical and experimental results (see Fig. 37).

Additional evidence to support these assignments was obtained from triton energy spectra for the reaction $^{11}B(p,t)^{9}B$. These spectra were taken with the same ^{11}B targets used in the $^{11}B(p,d)^{10}B$ reaction work and the particle identification system adjusted to detect tritons (see Fig. 38). The shapes of the angular distributions shown in Figure 39 can be explained with the following simple model for the (p,t) reaction. When the incident proton picks up two neutrons as a pair from ^{10}B, they must be in the singlet state with a total spin, S = 0 and the orbital angular momentum of the pair must be even (L = 0, 2, 4 . . .) from symmetry considerations. Using

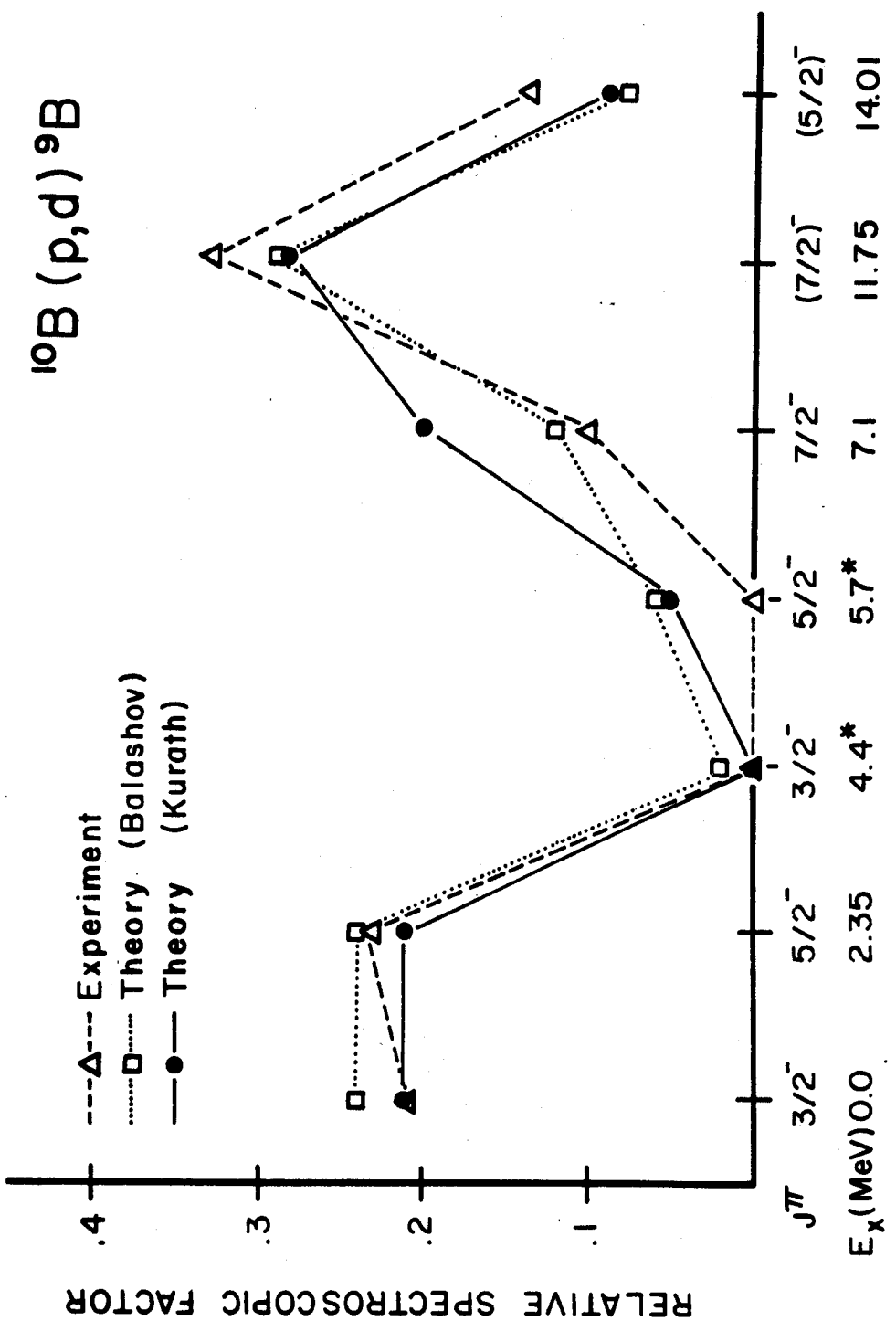

Figure 37.--Comparison of theoretical and experimental spectroscopic factors for $^{10}B(p,d)^{9}B$. No deuterons were observed corresponding to theoretically predicted ^{9}B levels at 4.4 and 5.7 MeV [18]; these levels are predicted to have small yields which may have been lost in the background. Angular momentum assignments for the observed states have been made on the basis of the observed agreement between Kurath's theoretical spectroscopic factors and the data.

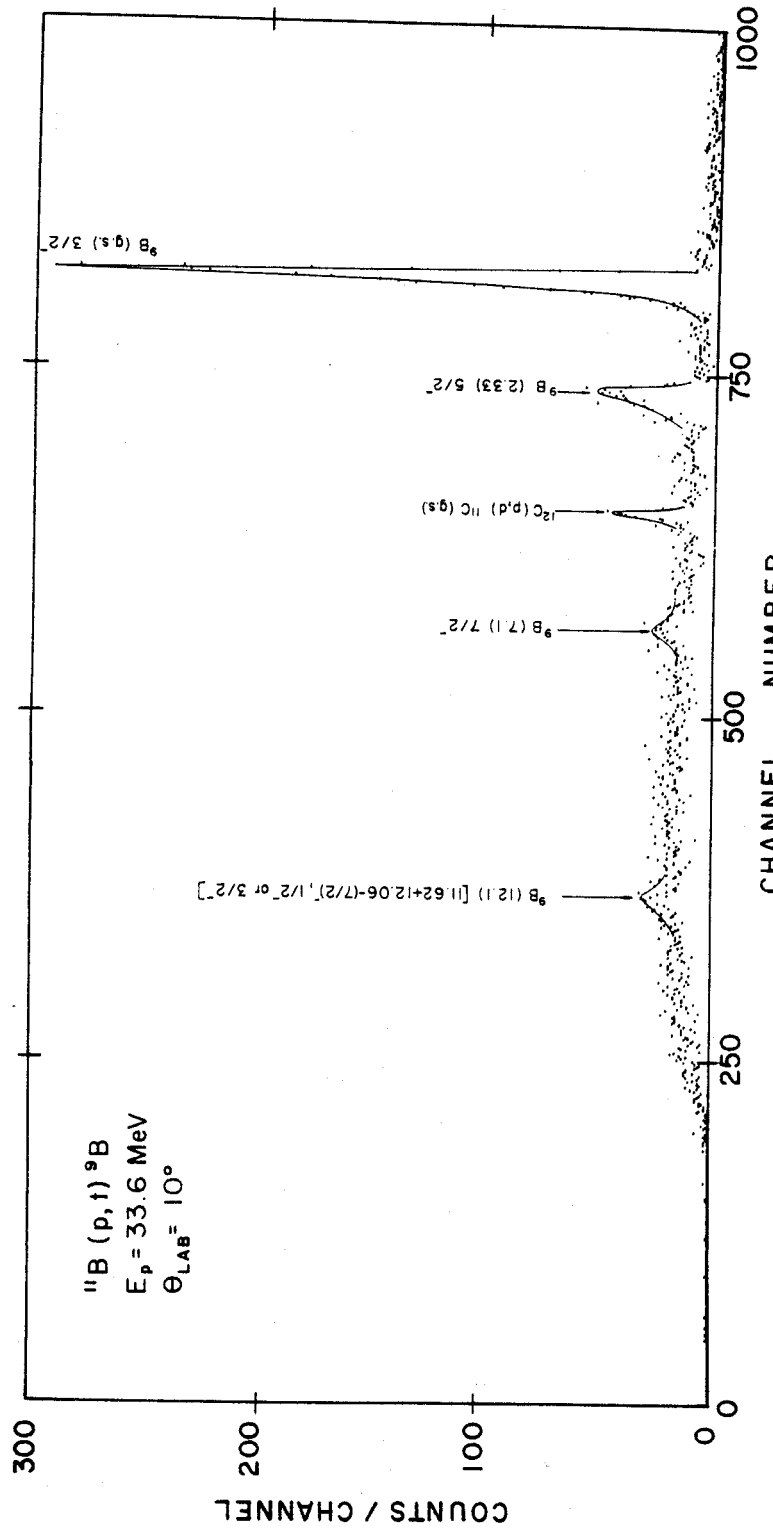

Figure 38.--^{11}B(p,t)^{9}B spectrum at 10 degrees. In setting the mass gate to insure counting all the tritons, some deuterons from the reaction ^{12}C(p,d) ^{11}C (g.s.) were permitted to leak through.

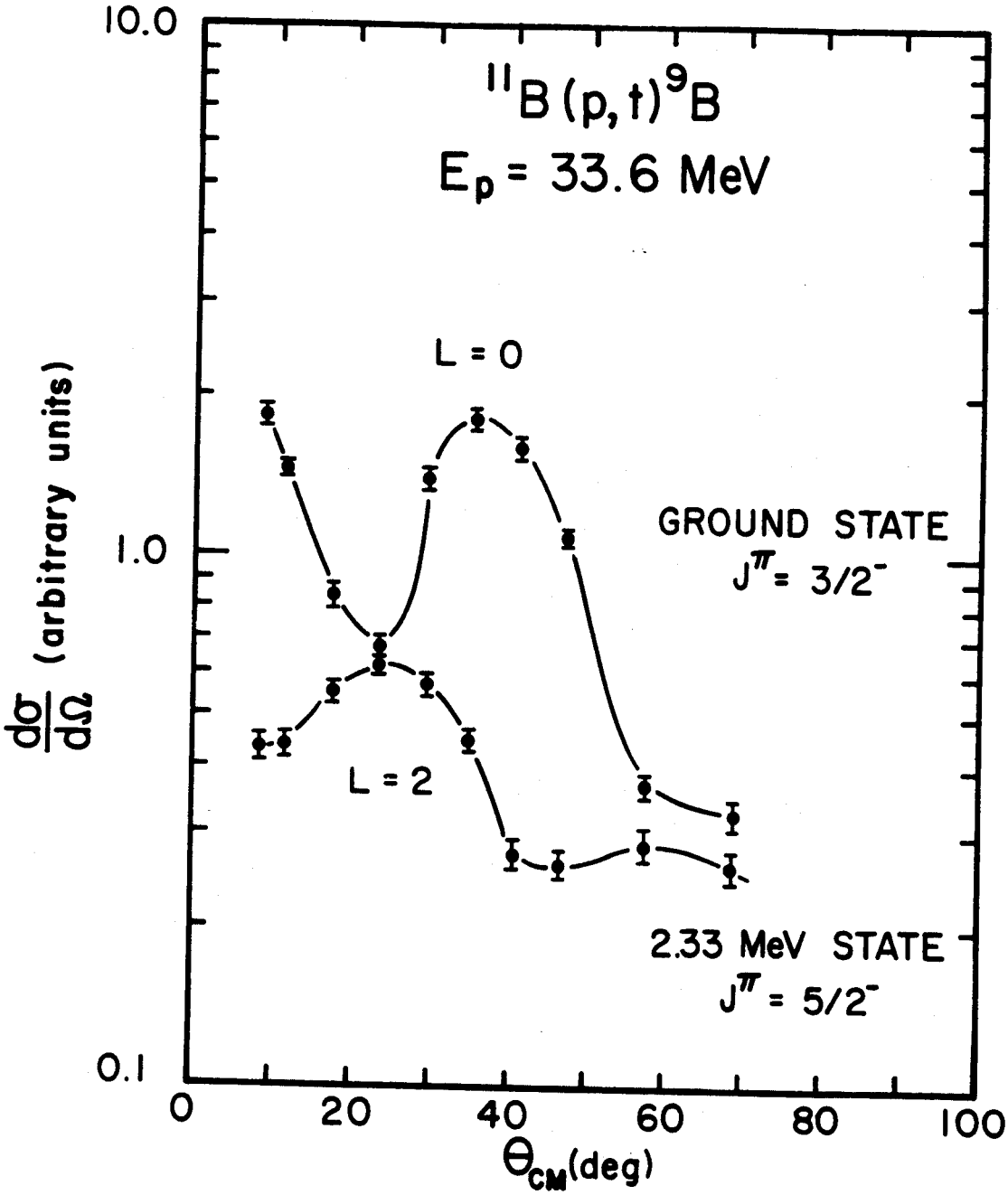

Figure 39.--$^{11}B(p,t)^{9}B$ angular distributions for the ground state and 2.33 MeV excited state of ^{9}B.

this simple picture, the ground state angular distribution for $^{11}B(p,t)^{9}B$ has a characteristic shape for the pickup of a dineutron with orbital angular momentum L = 0. This means the ground state of ^{9}B can only have the assignment $J^{\pi} = 3/2^{-}$, in agreement with the $^{10}B(p,d)^{9}B$ work. The angular distribution for the 2.33 MeV state has a characteristic shape for the pickup of a dineutron with L = 2 allowing for spin and parity assignments of $J^{\pi} = 7/2^{-}$, $5/2^{-}$, $3/2^{-}$, and $1/2^{-}$. These values do not contradict the previous $J^{\pi} = 5/2^{-}$ assignment for this state. It should also be noted that the assignments for the levels at 0.0, 2.35, and 7.1 MeV coincide with the spin assignments for isobaric analogue levels of ^{9}Be at 0.0, 2.43, and 6.66 MeV excitation [10]. There is therefore a significant amount of supplementary evidence to support the spin and parity assignments which were made on the basis of agreement between experimental and theoretical spectroscopic factors.

CHAPTER 7

CONCLUSIONS

The experimental results of this thesis show that Kurath's intermediate coupling model of 1p shell nuclei correctly describes the actual physical situation. The only case where the theoretical calculations of Kurath and the experimental data were not in reasonable agreement was that of the $J^{\pi} = 2^{+}$ and 3^{+} doublets of ^{8}Be, however, the observed differences were explained by the inclusion of isotopic spin mixing in the wave functions for these doublet states. In fact, considering the otherwise good agreement obtained between theory and experiment, the discrepancies noted in the $^{9}Be(p,d)^{8}Be$ reaction illustrate in a very concise manner that the ^{8}Be 2^{+} and 3^{+} states contain admixtures of $T = 0$ and $T = 1$.

On the basis of the intermediate coupling model's ability to predict spectroscopic factors to within $\sim\pm 20\%$, spin assignments were made for the observed negative parity levels of ^{9}B by comparing the experimental data with the model predictions. The same general agreement between theory and experiment was observed for these states of previously undefined spin as was observed for states of known spin in other 1p shell nuclei.

Thus, this systematic study of the effectiveness of the intermediate coupling model in the 1p shell has provided a basis for extending our knowledge of the 1p shell nuclei by helping to establish a reliable framework into which new experimental facts can be fitted. It should be emphasized that the present work only tests one aspect of the model, i.e. its ability to predict spectroscopic factors. Other checks have been made to test the model's ability to predict energy levels [20] and electromagnetic transition widths [19]. These studies have revealed a failure of the model to reproduce collective effects, a weakness which is not reflected in the extracted spectroscopic factors.

The direct comparison of the results of this work with results from neutron pickup reactions performed at different energies and with different incident particles shows that the spectroscopic factors can be measured to within an uncertainty of approximately ±20%; an estimate generally held among workers in the field, but one for which there was little firsthand evidence. More important, the spectroscopic factors do not appear to depend significantly on the incident particle or its energy; this gives some assurance that the experimental spectroscopic factors obtained here do yield a reasonable measure of the overlap of the target and residual nuclear wave functions.

No evidence was found for any 2s-1d shell admixtures in the ground state wave functions of ^{6}Li, ^{7}Li and ^{9}Be; no significant admixtures from this shell were found in the

ground state wave functions of ^{10}B and ^{11}B. The strongly excited 16.6 MeV state of ^{5}Li is the only case where neutron pickup from the 1s shell was observed with any appreciable yield. The 11.4 MeV state of ^{8}Be ($J^{\pi} = 4^{+}$) appears to be excited by a compound nucleus mechanism and not because of any 1f admixture in the ^{9}Be ground state wave function [13]. From this study, therefore, the ground states of ^{6}Li, ^{7}Li, ^{9}Be, ^{10}B and ^{11}B appear to consist of tightly bound 1s cores, the remaining nucleons residing in the 1p shell with no sizable admixtures from other shells.

APPENDIX I

LITHIUM DRIFTED SILICON DETECTORS

The method used to fabricate lithium drifted silicon detectors was similar to that described by Goulding [71]. Wafers from 2 to 4 mm thick were cut from p-type silicon (typically with a resistivity of ∿100 ohm-cm). The crystal faces were lapped with #95 Al_2O_3 grit and #1000 silicon carbide grain to smooth the surfaces and remove saw marks. One surface was then coated with a lithium-mineral oil suspension and the wafer heated in an oven for 8-12 minutes at ∿350° C in an argon atmosphere. In this process, the lithium donor ions diffuse into the surface of the p-type silicon forming a p-n junction.

After cooling, the wafer's sides were etched in an $HF-HNO_3$ solution to rid them of impurities and the junction tested for diode characteristics. The etching was repeated until the leakage current was of the order of microamps with no junction breakdown evident for a reverse bias of several hundred volts. At this point in the fabrication process, typical surface resistances were 200-300 Ω for the lithium n-side of the wafer and ∿100 KΩ for the p-side of the wafer.

If a reverse bias is now placed across the junction, the lithium donor atoms diffuse or "drift" into the p-type silicon. At equilibrium, they compensate the effect of the acceptor distribution, causing the region to react like an "intrinsic" or pure material, so that an electric field applied across the region will cause very little current to flow (on the order of .01 - .1 μ amps). The "drifting" apparatus consisted of a hot plate kept at a temperature of 80° - 140° C to which the wafer was affixed. A reverse bias on the order of 500 volts was placed across the junction resulting in a drift power (energy dissipated in the crystal) of 0.5 to 2.0 watts depending on the particular crystal and the amount of time spent in the drift. The width of the intrinsic region (W) is roughly given by [4],

(1) $W = \sqrt{2\mu_L Vt}$ (cm)

V = drift voltage

μ_L = mobility of Li ions (cm^2/volt sec.)

t = time (sec.)

The mobility of the lithium ions (μ_L) depends on the detailed characteristics of the silicon material used (impurity content, defect concentration, etc.) and varies directly with the drift temperature. Typical lengths of drift time for depletion depths of ∿3mm were 2 1/2 - 3 weeks. If at any time during the drift process the leakage current grew so large that only a small drift voltage (V)

could be used in order to stay within a crystal power dissipation of 2 watts, the wafer was removed from the apparatus and its sides etched in the $HF-HNO_3$ solution to clean off any accumulated surface impurities. It was then replaced in the apparatus and the drift process resumed.

The procedure for checking the depth of the depletion region consisted of placing the wafer in a $CuSO_4$ solution, to which a few drops of HF had been added, so that the n-face of the crystal remained dry. When placed in sunlight or strong artificial light, copper will plate out only on the intrinsic region and hence the depth may be readily determined.

When the desired depletion depth was obtained, the crystal was cut into a shape similar to that shown in Figure 40. The surfaces were lapped and then cleaned by etching. Gold was plated on the upper and lower surfaces for electrical contacts and the finished detector placed in a mount similar to that shown in Figure 40. The design of the detector minimizes the sensitive region of the detector and hence minimizes the background due to neutrons and gamma rays. The detector encapsulation protects the surfaces of the crystal from accumulation of pump oil and other impurities and makes the detector easy to handle.

Detectors could be made in this way with depletion depths of about 3 mm. and produced deuteron energy spectra with an overall energy resolution of 100-150 keV. They

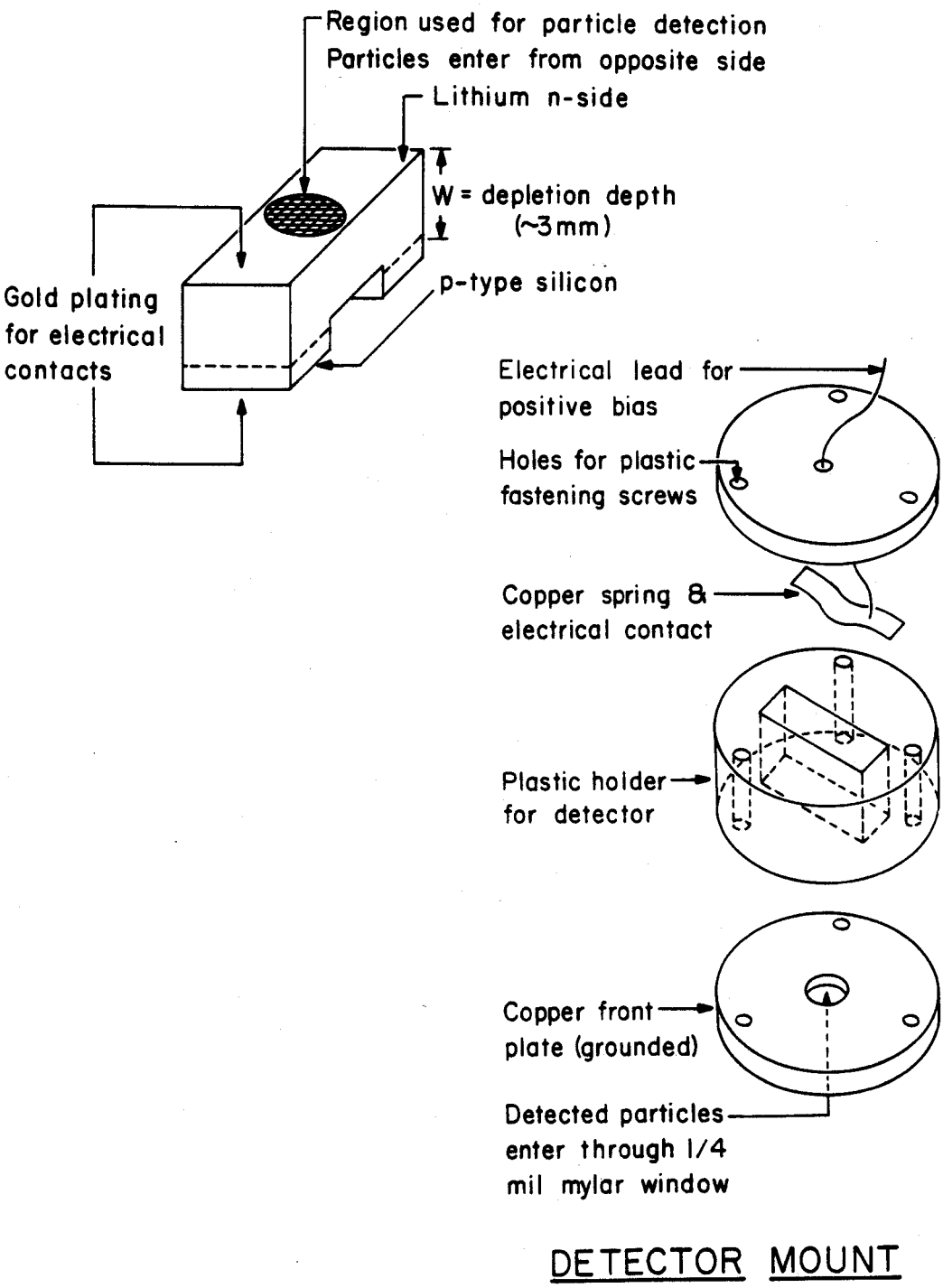

Figure 40.--Lithium drifted detector and mount.

were, however, difficult to produce and their lifetime short (one week or less). The reason for this short useful life was probably due to imperfect sealing of the encapsulation and not to radiation damage. Commercially purchased detectors with similar initial characteristics, but with more sophisticated packaging, had lifetimes of 1 1/2 to 2 months with approximately 100 hrs/week of actual use with proton beam currents of 1-100 nanoamps.

BIBLIOGRAPHY

1. L. Kull, Bull. Am. Phys. Soc. 12, 17 (1967).
2. L. Kull and E. Kashy, Bull. Am. Phys. Soc. 12, 484 (1967).
3. K. G. Standing, Phys. Rev. 101, 152 (1956).
4. J. G. Likely, Phys. Rev. 98, 1538 (1955).
5. J. B. Reynolds and K. G. Standing, Phys. Rev. 101, 158 (1956).
6. E. F. Bennett and D. R. Maxson, Phys. Rev. 116, 131 (1959).
7. J. Legg, Phys. Rev. 129, 272 (1962).
8. T. H. Short and N. M. Hintz, Bull. Am. Phys. Soc. 9, 391 (1964).
9. University of Minnesota Linac Lab Prog. Report, 61 (1964).
10. T. Lauritsen and F. Ajzenburg-Selove, Nucl. Phys. 78, 1 (1966).
11. W. Selove, Phys. Rev. 101, 231 (1956).
12. D. Bachelier, et al., J. Phys. (Paris) Colloq. 1, 70 (1966).
13. D. Bachelier, et al., International Conference on Nuclear Physics, Gatlinburg, 1966 (unpublished).
14. E. Kashy and T. W. Conlon, Phys. Rev. 135, B389 (1964).
15. R. Sherr, et al., Phys. Rev. 139, B1272 (1965).
16. D. Kurath (private communication).
17. F. C. Barker, Nucl. Phys. 83, 418 (1966).
18. V. V. Balashov, A. N. Boyarkina, and I. Rotter, Nucl. Phys. 59, 417 (1964).

19. D. Kurath, Phys. Rev. 106, 975 (1957).

20. D. Kurath, Phys. Rev. 101, 216 (1956).

21. H. Feshbach, Direct Interactions and Nuclear Reaction Mechanisms (Gordon and Breach, London, 1962), p. 215.

22. Ibid., Chapter 3.

23. A. Messiah, Quantum Mechanics (Gordon and Breach, New York, 1962), Chapter 21.

24. W. Tobocman, Theory of Direct Interactions (Oxford, London, 1961), Chapter 3.

25. R. M. Drisko and G. R. Satchler, Proceedings of the Rutherford Jubilee Conference (1961), (Academic Press, Inc., New York, 1961), p. 555.

26. J. K. Dickens, R. M. Drisko, F. G. Perey and G. R. Satchler, Phys. Letters 15, 337 (1965).

27. N. Austin, R. M. Drisko, E. C. Halbert, and G. R. Satchler, Phys. Rev. 133, B3 (1964).

28. M. E. Rose, Elementary Theory of Angular Momentum (Wiley, New York, 1957).

29. E. H. Auerbach, Brookhaven National Laboratory Report No BNL6562, Abacus-2, 1962 (unpublished).

30. C. Kittel, Elementary Statistical Physics (John Wiley and Sons, Inc., New York, 1958), p. 173.

31. P. E. Hodgson, Optical Model of Elastic Scattering (Clarendon Press, London, 1963), Chapter 3.

32. S. K. Penny and G. R. Satchler, Nucl. Phys. 53, 145 (1964).

33. L. L. Lee, J. P. Schiffer, B. Zeidman, G. R. Satchler, R. M. Drisko and R. H. Bassel, Phys. Rev. 136, B971 (1964).

34. M. Mayer, Phys. Rev. 78, 16 (1950).

35. D. R. Inglis, Rev. of Mod. Phys. 25, 390 (1953).

36. D. H. Wilkinson, Proceedings of the Robert A. Welch Foundation Conferences on Chemical Research - The Structure of the Nucleus, (1957).

37. L. Rosenfeld, Nuclear Forces (North Holland, Amsterdam, 1948), p. 234.

38. E. Feenberg and E. Wigner, Phys. Rev. 51, 95 (1937).

39. S. Cohen and D. Kurath, Nuclear Physics 73, 1 (1965).

40. H. G. Blosser and A. I. Galonsky, International Conference on Isochronous Cyclotrons, Gatlinburg, 1966 (unpublished).

41. M. E. Rickey and R. Smythe, Nucl. Inst. Meth. 18, 19, 66 (1962).

42. ORTEC Instruction Manual, Silicon Surface Barrier Detectors, Oak Ridge Technical Measurement Corporation.

43. F. S. Goulding, D. A. Landis, J. Cerny and R. H. Pehl, Nucl. Instr. Meth. 31, 1 (1964).

44. B. M. Bardin and M. E. Rickey, Rev. Sci. Instr. 35, 902 (1964).

45. R. D. Evans, The Atomic Nucleus (McGraw-Hill Book Co., New York, 1955).

46. K. Wildermuth and Th. Kanellopoulos, Nucl. Phys. 1, 150 (1958).

47. I. L. Rozental, JETP USSR 28, 118 (1955).

48. T. A. Tombrello, A. D. Bacher and R. J. Spiger, Bull. Am. Phys. Soc. 10, 423 (1965).

49. S. T. Butler, Phys. Rev. 106, 272 (1957).

50. K. Wildermuth, Nucl. Phys. 31, 478.

51. J. B. Marion, Phys. Letters 14, 315 (1965).

52. C. P. Browne and J. R. Erskine, Phys. Rev. 143, 683 (1966).

53. P. Paul, Zeitschrift für Naturforschung 21, 914 (1966).

54. P. Paul, D. Kohler and K. A. Snover, Bull. Am. Phys. Soc. 11, 26 (1966).

55. G. T. Garvey, J. Cerny, and H. Pugh, Bull. Am. Phys. Soc. 11, 26 (1966).

56. J. B. Marion and C. A. Ludemann, Bull. Am. Phys. Soc. 11, 26 (1966).

57. D. Bachelier, et al., J. Phys. (Paris) Colloq. 1, 51 (1966).

58. E. F. Farrow and H. J. Hay, Phys. Letters 11, 50 (1964).

59. I. Slaus (private communication).

60. G. Crawley and S. Austin, Inter. Conf. on Nuclear Physics, Gatlinburg, 1966 (unpublished).

61. G. Schrank, E. K. Warburton, and W. W. Dachnick, Phys. Rev. 127, 2159 (1962).

62. D. Hasselgren, P. U. Renberg, O. Sundberg, and G. Tibell, Nuc. Phys. 69, 81 (1965).

63. R. J. Slobodrian, Phys. Rev. 125, 1003 (1962).

64. R. J. Slobodrian, Nucl. Phys. 32, 684 (1962).

65. D. Dehnhard, G. C. Morrison, and Z. Vager, Inter. Conf. on Nuclear Physics,Gatlinburg (1966), (unpublished).

66. R. H. Bassel, R. M. Drisko, and G. R. Satchler, "Distorted-Wave Theory of Direct Nuclear Reactions," ORNL-3240 (1962).

67. S. M. Bunch, H. H. Forster and C. C. Kim, Nucl. Phys. 53, 241 (1964).

68. R. H. Siemssen, Bull. Am. Phys. Soc. 12, 479 (1967).

69. R. Satchler (private communication).

70. N. Austern, "Fast Neutron Physics" (Interscience, New York, 1961), Vol. II, ed. by J. B. Marion and J. L. Fowler.

71. F. S. Goulding, UCRL-16231 (1965), Appendix I.